Non-Destructive Bridge Deck Condition Assessment with a Probability-Based Deterioration Threshold

Tao Zou

Dissertation submitted to the Faculty of the

Virginia Polytechnic Institute and State University

in partial fulfillment of the requirements for the degree of

Doctor of Philosophy

In

Civil Engineering

Cristopher D. Moen, Chair

Thomas E. Cousins

Carin L. Roberts-Wollmann

William J. Wright

February 21st, 2013

Blacksburg, Virginia

Keywords: Bridge Deck, Deterioration, Non-Destructive Evaluation, Deterioration Threshold, Finite Element Method, LTBP Program

Non-Destructive Bridge Deck Condition Assessment with a Probability-Based Deterioration Threshold

Tao Zou

Abstract

Deterioration of bridge decks is an ongoing problem faced by transportation agencies across the country. In past decades, Non-Destructive Evaluation (NDE) techniques, capable of detecting various deteriorations types, e.g., cracking, delamination and reinforcing steel corrosion, have emerged. These techniques generate large amounts of data representing different underlying physics, (decibels for ground penetrating radar and volts for half-cell potential), making data interpretation and comparison difficult for bridge owners and practitioners. The deterioration threshold, or the transition between healthy and deteriorated areas, is essential in understanding NDE data. However, this threshold is determined empirically in former research and engineering practice. In the present research, a probability-based method is proposed to identify deterioration thresholds for specified confidence levels. NDE data measuring different underlying physics are transformed into a binary format by threshold values to compare and combine multiple NDE techniques for bridge deck assessment. The finite element method is also implemented to correlate bridge deck surface stresses with deteriorations measured by NDE techniques, and to study the causes on concrete bridge deck degradation. The general methodology developed in this study will be demonstrated on three bridges, i.e., Virginia and New York Pilot Bridges, which were studied under Federal Highway Administration (FHWA)'s Long-Term Bridge Performance (LTBP) Program.

Acknowledgement

I would firstly express my great appreciation and sincere gratitude to my mentor and advisor, Dr. Cristopher D. Moen. Without Dr. Moen's instruction and help, I will never have the chance to finish this dissertation. His kind and thoughtful guidance throughout my PhD study have been inspiring, and it has been a great honor and a pleasure for me to be his student.

I would also like to thank the members of the dissertation defense committee, Dr. Thomas Cousins, Dr. Carin Roberts-Wollmann, and Dr. William Wright. Dr. Cousins helped me coordinate with other researchers and institutes working on the LTBP Program, and gave me access to the LTBP's database. Dr. Roberts-Wollmann offered me insight ideas on understanding concrete shrinkage properties. Dr. Wright's class on steel bridge design helped me organize the knowledge on the bridge I worked on.

My PhD work has also greatly benefited from other Virginia Tech researchers, as well as researchers from Rutgers University and VDOT. Amey developed the initial finite element model, which helped me get into the program quickly. Farmir gave me ideas on modeling reduced elastic modulus of concrete due to shrinkage, according to his laboratory tests. And support and help from members of Dr. Moen's research group are also greatly appreciated.

Finally, and most importantly, I would like to thank my parents and my wife, without their help,both physical and mental, I could never possibly accomplish my work.

Table of Contents

List of Figures

List of Tables

Chapter 1 : Introduction

Among over 600,000 bridges in United States, one in four is categorized as structurally deficient and needs repair according to National Bridge Inventory (2003). Bridge decks, which carry traffic loads directly, are most vulnerable to degradation and usually with less service life than design expectations. Therefore, it is necessary to evaluate and predict the degradation of bridge structures, especially deteriorations of concrete bridge decks.

Non-destructive evaluation (NDE) techniques have been developed to evaluate bridge deck deteriorations without damaging structures. NDE evaluations are typically based on numerous techniques, commonly acoustic, ultrasonic, electromagnetic and electrochemical (Scott et al. 2001). These techniques generate data representing different underlying physics, e.g., signal attenuation (decibels) for ground penetrating radar (GPR) and electrical potential (volts) for half-cell potential (Belli et al. 2008; Roberts 1995; Elsener 2001). Interpretation and comparison of such data with numerous physics are difficult for researchers and practitioners. The deterioration threshold, or the probable transition between healthy and deteriorated areas, is essential in understanding measured NDE data (Gucunski et al. 2005). However, former research and industry practitioners typically determine this threshold empirically (Romero 2010) or by varying a data normalization parameter from one NDE technique to obtain the best graphical correlation with another NDE mapping (Rhazi et al. 2007). Therefore, there are demands to develop a general quantitative procedure identifying deterioration thresholds, and provide reliable comparison and combination of different NDE data in assessing bridge deck conditions. The study of causes and influential factors on bridge deck degradation can help control deteriorations. As a convenient tool, finite element methods are capable to analyze bridge deck

behaviors under the influences of live loading and concrete shrinkage, providing a way to study correlations between external effects induced stresses and concrete deteriorations (Lee 2010; Schindler et al. 2010).

The present research develops a general probability based method to identify deterioration thresholds of NDE data and apply determined threshold values to map continuous and quantitative NDE data into a binary format. NDE data is then combined to assess bridge deck conditions. The finite element analysis is also used to study the correlation between bridge deck surface stresses and the NDE data under influences of live loads and concrete shrinkage. This addresses most influential factors on bridge deck deteriorations.

1.1 Long-Term Bridge Performance Program and Pilot Bridges

The Long-Term Bridge Performance (LTBP) Program was initiated by Federal Highway Administration (FHWA) to improve the performance of U.S. highway systems, in terms of safety, reliability, effectiveness and sustainability (Hamid Ghasemi et al. 2009). One of the goals of the LTBP Program is to determine causes and processes of bridge deck deteriorations, and propose models predicting potential future deteriorations on bridge decks. During the pilot phase, seven bridges distributed throughout the United States were subjected to an initial round of bridge performance testing. This research is presented on two of the pilot bridges, i.e., Virginia and New York Pilot Bridges, east of the Mississippi River, on which researchers from Virginia Tech and other institutes performed the tests.

1.1.1 Virginia Pilot Bridge and Non-Destructive Evaluation

Virginia Route 15 Bridge over Interstate 66 is the first pilot bridge that was studied in LTBP Program. It is a common steel stringer bridge built in 1979 with a total length of 83.5 m (274 ft.)

and two 41.8m (137 ft.) spans cross over two lanes of east and westbound Interstate travelling southbound (Collins 2010), as shown in Figure 1-1.

Figure 1-1 Virginia Route 15 Bridge over Interstate 66 (Photograph by Collins)

The bridge deck is supported by six continuous steel girders with varying cross section and 2.3m (7ft-6in) center to center spacing, and cross frames to ensure the lateral stability as shown in Figure 1-2.

Figure 1-2Virginia bridge girders and cross frames (Photograph by Collins)

The bridge deck thickness is around 200 mm (8.5 in.) with an approximate skew of 17.45°. Steel girders are supported on abutments with rocker bearing and on piers with pin bearings. The concrete deck of this bridge is in fairly poor condition with visible deteriorations on the surface as shown in Figure 1-3.

Figure 1-3Deterioration on Virginia Route 15 Bridge (Photograph by Gucunski et al.)

Field testing and validations were conducted by means of destructive and nondestructive evaluation, by both LTBP Program in September 2009 and SHRP 2 in 2010 (Gucunski et al. 2013). In the present research, analysis will be based on data obtained by LTBP Program in 2009. The primary objectives of these testings were to study effectiveness of NDE techniques in detecting different bridge deck deterioration types. The chain drag, GPR and half-cell potential mappings are shown in Figures 1-4, 1-5 and 1-6.

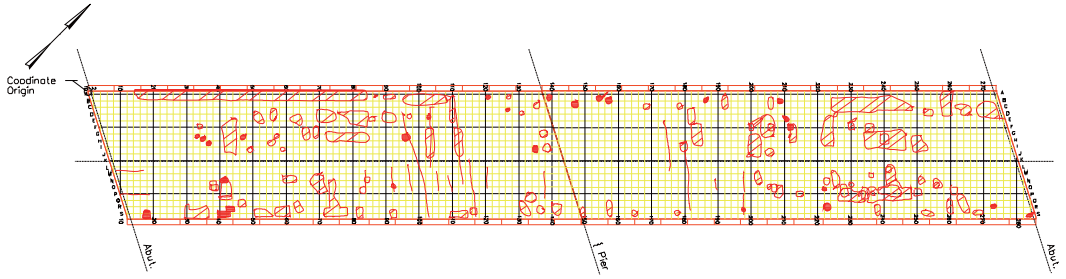

Figure 1-4 Chain drag condition map for Virginia Pilot Bridge (Andrew Foden 2009)

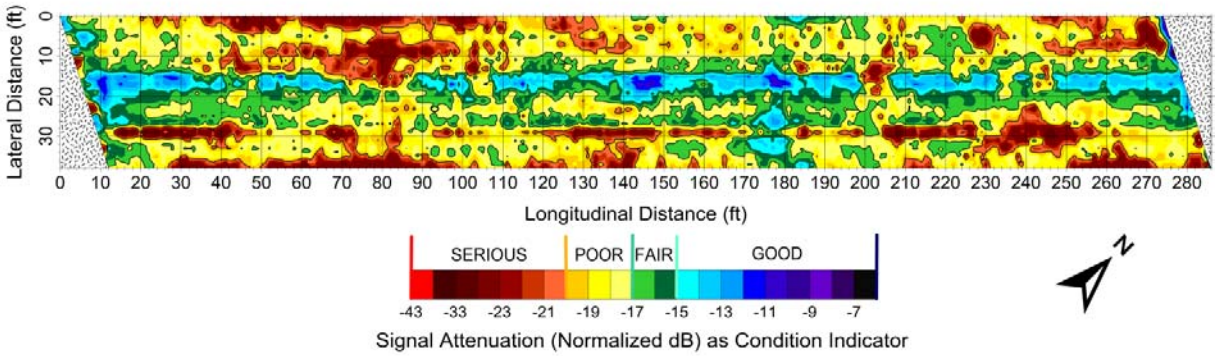

Figure 1-5 GPR Condition Map for Virginia Pilot Bridge (Rutgers University 2009)

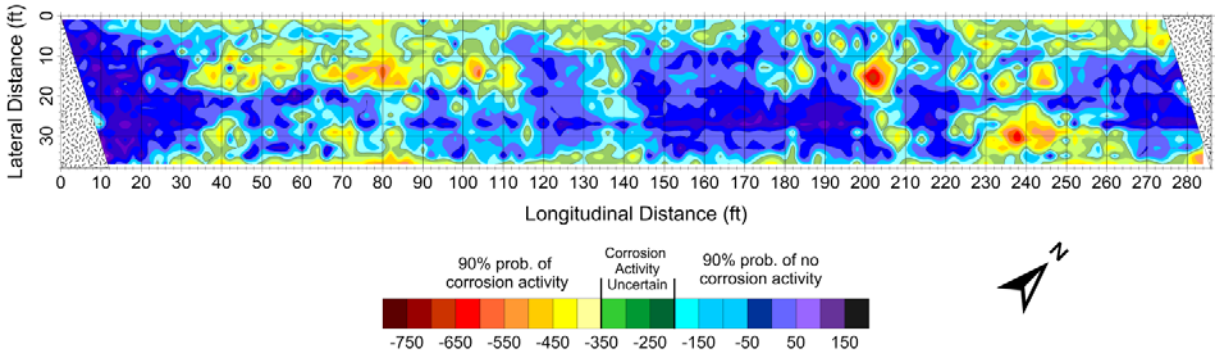

Figure 1-6 Half-Cell Potential Map of Virginia Pilot Bridge (Rutgers University 2009)

1.1.2 New York Pilot Bridge and Non-Destructive Evaluation

The New York Pilot Bridge, shown in Figure 1-7, is located in the western part of the state in the town of Almond, approximately 120 miles west of Binghamton, NY. The weather exposure and environmental conditions in western New York represent a cold-humid climate. The bridge carries two lanes of traffic on NY Route 21 over the Karr Valley Creek. The New York Pilot Bridge is a two-span, adjacent, precast, prestressed concrete box beam superstructure that was constructed in 1990.

Figure 1-7 New York Pilot Bridge Karr Valley Creek (Rutgers University 2009)

The superstructure of the New York Pilot Bridge consists of adjacent box beams (Figure 1-8) with a 150 mm (6 in.) cast-in-place concrete topping. The superstructure is continuous over the center pier with longitudinal epoxy-coated mild steel reinforcement (ECR) in the negative moment region of the superstructure over the center pier. The GPR and half-cell potential mappings of New York Pilot Bridge deck conditions are shown in Figures 1-9 and 1-10.

Figure 1-8 Adjacent box beams of New York Pilot Bridge (Rutgers University 2009)

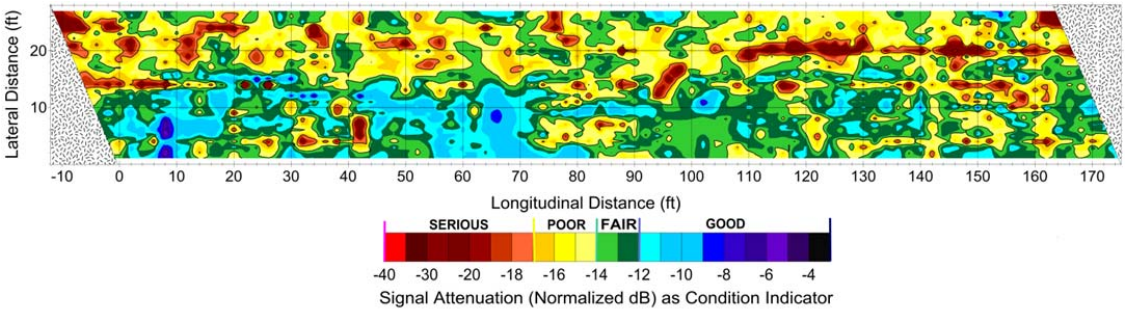

Figure 1-9 GPR condition maps before and after asphalt overlay for New York Pilot Bridge (Rutgers University 2009)

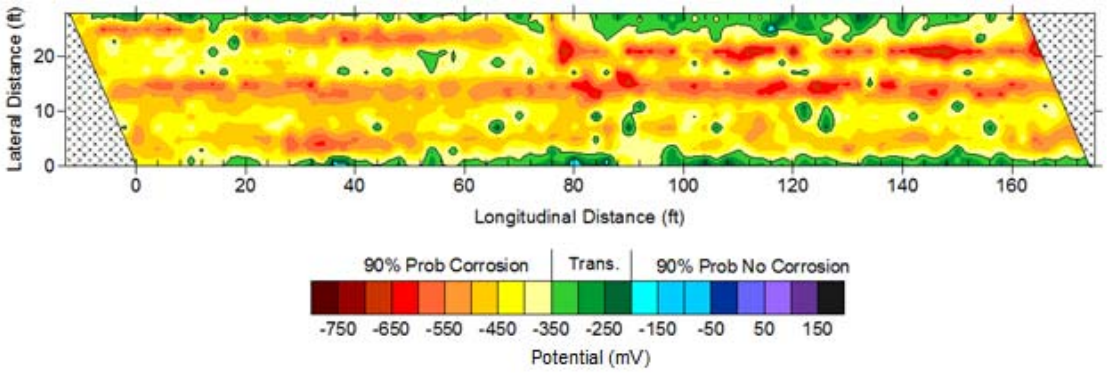

Figure 1-10 Contour map of half-cell potential results for New York Pilot Bridge (Rutgers University 2009)

1.2 Deterioration Thresholds

Healthy and deteriorated areas of a bridge deck identified with NDE are typically demarcated with a deterioration threshold, defined as the probable transition within the range of NDE data (e.g., 2.41 kohm-cm to 98.91 kohm-cm for resistivity or -36.32 dB to -8.92 dB for GPR) from healthy to deteriorated areas on a bridge deck (Gucunski et al. 2005). Historically, this deterioration threshold has been defined subjectively by the operator conducting the NDE measurements considering the age of bridge deck, visual deck condition, and the intensity of NDE signal change (Gucunski et al. 2005). Another approach is to vary a data normalization parameter from one NDE technique to obtain the best graphical correlation with another NDE

mapping (Rhazi et al. 2007). Specific deterioration threshold values based on NDE type have been proposed, for example, between 5.08 kohm-cm and 9.91 kohm-cm for resistivity (Manning 1985), however these thresholds are typically established from project-specific data and are not appropriate for general application (Guthrie and Tuttle 2006).

1.3 Scope and Objectives

This research develops a general probability based approach to identify deterioration thresholds of quantitative NDE data and assess bridge deck conditions. To compare NDE data measuring different underlying physics, deterioration thresholds are used to transform quantitative data into a binary format. The bridge deck condition is then assessed by overlapping these NDE data. The finite element method is also implemented to evaluate causes of deterioration on bridge decks. Surface stresses on bridge deck induced by live loads and concrete shrinkage are correlated to NDE data. The theory and application are introduced on two pilot bridges with numerous degrees of deck deteriorations within FHWA's LTBP Program.

The primary objectives of this research are composed of three parts:

- Develop a probability-based method to identify deterioration thresholds for quantitative NDE data.
- Use deterioration thresholds to transform quantitative NDE data into a binary format. Assess bridge deck conditions by combining NDE data measuring different underlying physics.
- Develop a finite element model to study stress distributions on the bridge deck. Correlate stresses with NDE deteriorations.

1.4 Dissertation Organization

This dissertation is organized in the manuscript format, where the traditional chapters in a dissertation are replaced by manuscripts that have been or will be submitted to peer-reviewed journals or conferences. For this dissertation, two journal papers and one conference paper are presented.

A literature review is presented in Chapter 2 to provide additional background on numerous topics, including: (1) bridge deck deterioration causes and types, (2) NDE techniques in the concrete deterioration detection, (3) empirical deterioration threshold definitions, (4) finite element modeling on composite bridges, (5) finite element modeling on bridge deck deteriorations and (6) finite element modeling on bridge deck cracking.

Chapter 3 is a manuscript entitled "A Probability-Based Threshold Definition for Non-Destructive Bridge Deck Deterioration Evaluation", which will be submitted to the Journal of Structural Engineering. This manuscript focuses on the procedure in developing the probability-based method to identify deterioration thresholds; this methodology is introduced for general sets of NDE data and the application is demonstrated on two pilot bridges. Chapter 4 presents the conference paper entitled "Non-Destructive Bridge Deck Condition Assessment with Deterioration Thresholds", which is published in the proceedings of the 93rd Transportation Research Board Annual Meeting. This manuscript presents the application of the probability-based deterioration thresholds. GPR and half-cell potential data are normalized by identified deterioration thresholds, and combined with chain drag in the bridge deck condition assessment. Chapter 5 is a manuscript entitled "Correlation between Live Load and Shrinkage Stresses and Bridge Deck Deterioration with Non-Destructive Evaluation", which will be submitted to the Journal of Bridge Engineering. This manuscript demonstrates a finite element model in

analyzing structural behaviors under influences of live loading and concrete shrinkage, and studies the correlation between live load and shrinkage stresses and bridge deck deteriorations.

Chapter 6 summarizes results, gives conclusion and recommends future research. The reference for all the chapters is then provided at the end of the dissertation. Appendix A presents the theoretical procedure in deriving the GPR signal attenuation distribution for healthy concrete. Appendix B summarizes the vertical deflection and longitudinal strain comparisons between finite element results and field testing data.

Chapter 2 : Literature Review

2.1 Concrete Bridge Deck Deteriorations

Bridge deck deterioration is the main reason for categorizing a bridge as structurally deficient (Tsiatas and Robinson 2002). Among all types of concrete bridge deck deterioration (scaling, spalling, cracking, abrasion damage, alkali aggregate reaction, delamination, sulfate attack, saltwater and freeze/thaw), cracking, delamination and spalling are most harmful and greatly reduce the service life of bridge structures. And normally these deteriorations happen due to the corrosion of steel reinforcement (Russel 2004; Heckroodt 2002).

Breysse (2010) summarized the causes and mechanisms of the most common processes of reinforced concrete structure deteriorations, mainly by means of physical, mechanical damage process and chemicophysical damage process. Overloading, restraining effects, freeze and thaw and fire are classified as physical and mechanical damage process. Restraining effects are mainly due to concrete shrinkage and thermal gradients. Drying of concrete causes a differential shrinkage for the concrete member and leads to tensile stresses, which cause crack formation mainly perpendicular to the surface. Another mechanism that can induce cracks is thermal cracking at early age. Due to low thermal conductivity of concrete, internal parts tend to expand as a result of thermal dilation, which creates tensile strains and is an additional cause of cracking. Carbonation, chloride penetration and corrosion in reinforced concrete are classified as chemicophysical damage process. Carbonation starts on the concrete surface, and once carbonation process reaches the reinforcement, the passive layer covering the rebar deteriorates and corrosion initiates. Chloride ions enter the concrete by diffusing through the pores or through surface cracks, which can be mechanically induced or shrinkage cracks. When chloride ions

reach a rebar, they can induce corrosion, and further cause the delamination or spalling of concrete.

Cracks are the visual indicator for deteriorations of bridge decks, and cracks are categorized into three types by Tsiatas and Robinson (2002) as: inadequate structural performance cracks, inadequate material performance cracks, and acceptable cracks. Details related to the formation of these cracks are depicted in Table 2-1. Cracking of structural concrete causes multiple problems, which are mainly the decrease in structural integrity of the bridge component, and creating a flow path for penetration of chlorides. Tsiatas and Robinson (2002) indicated that cracks having widths as small as 0.004 to 0.008 in allow penetration of water and chloride solutions.

Table 2-1 Crack categorization and mechanisms of formation (Tsiatas and Robinson 2002)

Category of Crack	Inducing Mechanism
Inadequate structural performance	Excessive foundation settlement, excessive loading or construction overloads, excessive stresses due to thermal gradients, inadequate design or detailing, poor construction practices.
Inadequate material performance	Plastic shrinkage, drying shrinkage, reinforcement corrosion, free/thaw cycles, wet/dry cycles, chemical reaction
Acceptable	Cracks that must develop to properly distribute tensile stresses according to current design criteria.

Transverse cracking is the predominant form of bridge deck cracking (Ramey and Wright 1997), and generally occurs over reinforcing bars in transverse direction in the negative moment region in continuous spans (in the top region of the deck). Overall, cracking is more present in continuous spans (than simple spans), longer spans (than shorter spans), and older decks (than newer decks). Alampalli et al. (2002) reported a direct correlation between severity of cracking

and severity of vibrations. Numerous strategies have been discussed to reduce the transverse cracking, such as by using bars with size smaller than No. 5, experimenting with reinforcing bar arrangements, avoiding splicing transverse steel when possible, increasing deck thickness, standardizing deck thickness, increasing concrete cover to at least 2.5 in, when deicing salts are used, limiting water-to-cement (w/c) ratio to 0.4 to 0.45 and maintaining control on materials (Ramey et al., 1997).

Corrosion is an electrochemical process and ordinarily begins at the surface of the steel. (Callister, 1997), and is the most frequent and serious form of degradation of steel reinforced concrete (Taly, 1998). The corrosion of steel causes deterioration of concrete. The product of steel corrosion, rust, has a volume several times greater than the metallic iron from which it was formed, which causes pressure build-up and cracking in the concrete (Mays, 1992). Young et al. (1998) reported that 0.00004 to 0.0002 in. of corrosion is sufficient to cause concrete cracking. The resulting cracks often appear in an orientation parallel to the reinforcing steel.

Reinforced concrete bridge deck experiences an accelerated process in deterioration after concrete cracking. Tuutii (1982) discussed the process of reinforced concrete deterioration. The mechanism of corrosion is classified as two stages: the initiation period, in which chlorides penetrate concrete cover in sufficient quantities and depassivate reinforcing steel, and the propagation period, in which the structure deteriorates due to loss of reinforcing steel cross-section area. Cracks occur after the depassivation of reinforcing steel, which accelerates the deterioration propagation, and ultimately causes spalling, delamination and failure of concrete structures. Figure 2-1 summarizes the general deterioration process (Zhou 2005).

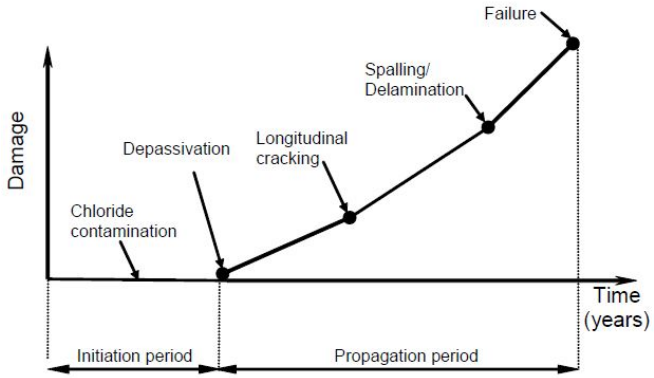

Figure 2-1 Corrosion Induced Damage of Reinforced Concrete Structures (Zhou 2005)

2.2 Non-Destructive Evaluation Methods

Condition surveys of concrete bridge decks provide critical information on the types and extent of deteriorations present on the deck, and can aid in the development of bridge deck preservation strategies, as well as in predicting the service life of a bridge deck (Hema et al. 2004). Non-destructive evaluations (NDE) are implemented to detect numerous types of deteriorations based on their physical properties, including acoustic (Gucunski et al. 2010), electromagnetic (Van Der Wielen et al. 2010), electrochemical (Shah and Ribakov 2008) and visual inspections. In this section, the past research is summarized on NDE techniques that will be discussed in this study, which are visual inspection, chain drag, ground penetrating radar (GPR) and half-cell potential.

2.2.1 Visual Inspection

Visual inspection is the first step in assessing the bridge deck conditions (Manning 1985; Shin et al. 2003), in which the type and extent of deterioration are documented. Due to the easy access, the visual inspection on bridge deck could be conveniently accomplished. For bridge decks with overlaid asphalt wearing surfaces, the removal of the wearing surfaces are usually required to avoid inaccuracy on bridge deck deterioration. When conducting visual inspections, inspectors may identify concrete stains and cracks, which are the primary indication of deck deteriorations.

Cracks are documented by the size, location and orientation, as well as the depth whenever possible (Manning 1985). Spallings could be easily detected by visual inspection, since deteriorated concrete and reinforcing bars are exposed; however, concrete delamination are not easily detected through visual inspection unless they are relatively shallow and accompanied by a discoloration of the bridge deck (Manning 1985). In addition, visual inspection is a subjective method, and the inspection accuracy is related to inspectors' experience (Shubinsky 2003).

2.2.2 Chain Drag

Chain drag is an acoustic method, detecting near surface concrete delamination, that is based on the change of sounds while a set of chain links are dragged on the bridge deck surface ((Scheff and Chen 2000; Yehia et al. 2007). Concrete without delamination will responde with a clear ringing sound, while the acoustic response is a dull, hollow sound for delaminated concrete (Stratfull 1973; Henderson et al. 1999). Chain drag is the most widely used detection technique after visual inspection since it is a fast and convenient way to locate delamination and severe stages of bridge deck deteriorations; however, like the visual inspection, the inspectors' operation and experience also play important roles on the results. The accuracy of chain drag mapping is commonly influenced by technician fatigue, since the constant noise tends to reduce the technician's sensitivity to changes in the acoustic response (Manning 1985).

Although chain drag provides valuable information about the presence and location of delaminations, it can do so after delaminations have progressed to the point where major rehabilitation is required (Gucunski et al. 2000). In addition, the accuracy of chain drag surveys on asphalt-covered decks is unsatisfactory (Manning 1985). However, the convenient application and low cost make it a preliminary method for detecting deteriorations before investigations by other techniques.

2.2.3 Ground Penetrating Radar (GPR)

Ground penetrating radar (GPR) is a high resolution electromagnetic technique that is used to located reinforcing steel corrosion, contaminated concrete, inadequate concrete cover, delamination and separating cracks (Yehia et al. 2007; Belli and Wadia-Fascetti 2002). GPR uses high frequency electromagnetic (EM) waves from an antenna in the frequency band of 1.0 to 2.5 GHz and transmits waves into bridge decks to map subsurface characteristics (Saarenketo and Soderqvist 1994). The radar waves are emitted into the bridge deck from a surface antenna that may be pulled along the ground or mounted to a vehicle (Shin and Grivas 2003; Conyers 2003; Maser et al. 2001).When the waves are reflected by an object with different electrical properties, e.g., boundaries between air and concrete, the receiving antenna records the variations in the reflected return signal (IAEA-TCS-17 2002). Typically, a small portion of the radar wave is reflected back to the surface antenna, while the remainder of the wave continues throught the bridge deck. The travel times and amplitudes of reflected radar waves are recorded as indications of bridge deck deteriorations (Shrin and Grivas 2003; Conyers 2003; Maser et al. 2001). Figure 2-2 shows a typical GPR system (Sharma 1997).

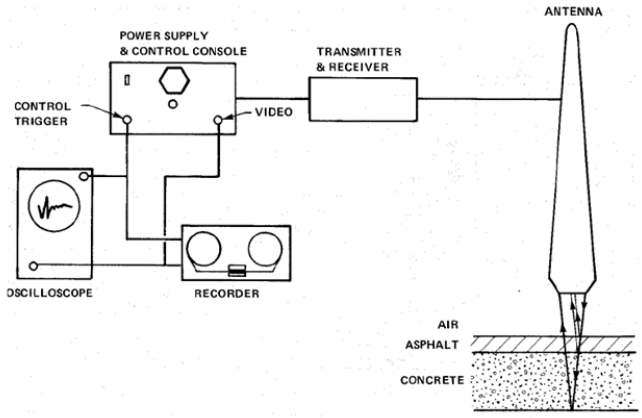

Figure 2-2 A typical GPR system

The depth to which a GPR unit can be used effectively and accurately depends on the electrical conductivity of the surface and subsurface materials (Sharma 1997). GPR waves can reach depths of 100 ft in low-conductivity materials, while for materials with high-conductivity, the depth of penetration could be reduced to less than 3 ft (GeoModel 2003). Since concrete is primarily composed of sand and gravel, which both have low electrical conductivity values, a concrete bridge deck can be an ideal environment for GPR survays (Sharma 1997). Delaminated concrete causes attenuation of the radar signal as the signal travels through the bridge deck and is reflected back from the damaged areas (Maser et al. 2001). Bridge decks overlaid with asphalt do not necessarily pose a problem for GPR mapping since asphalt consists principally of aggregate. GPR units are also capable of identifying concrete with high chloride and moisture contents since these factors produce high variable reflections of the radar wave at the overlay-deck interface (Maser et al. 2001).

The type of antenna used also affects the quality of GPR surveys, since the resolution of a GPR unit is directly proportional to the operating frequency (GeoModel 2003). Antennas with low frequencies, 25 to 200 MHz, can reach depths of 100 ft but with low resolution (GeoModel 2003). These types of antennas are generally used to locate large objects in the ground, such as sinkholes. Antennas with high frequencies, 300 MHz to 1 GHz, have a higher resolution but are limited to depths of about 30 ft in ideal conditions (GeoModel 2003). In a bridge deck survey, higher frequencies are necessary to achieve the increased resolution required to identify smaller objects such as reinforcing steel. A study conducted on a bridge deck in Finland demonstrated that the use of a GPR antenna with a frequency of 1.0 GHz resulted in good radar images without any data corrections (Saarenketo and Soderqvist 1994).

GPR offers many appealing advantages for assessing the condition of bridge decks (Sharma 1997). First, a GPR survey can reasonably provide an evaluation of the entire bridge deck with accuracy to within 3 to 15 percent of conventional core samples (FHWA 2000). Second, GPR decreases the safety risk to bridge inspectors by minimizing their exposure to traffic (FHWA 2000). In particular, the use of vehicle-mounted GPR units eliminates the need for lane closures and core patching and thus reduces traffic congestion as well. GPR units pulled or dragged by hand may necessitate a lane closure for relatively short periods of time, but the time that road crews are exposed to dangerous traffic conditions is still less than with other condition assessment methods. Vehicle-mounted units can travel at highway speeds and survey up to 200 miles per day. Manually dragged units require more time to survey a bridge deck than vehicle-mounted units but require significantly less time than taking cores preparation or any finishing reparation; therefore, labor and material costs to prepare and repair the deck are not required.

2.2.4 Half-cell Potential

The severity of steel corrosion in concrete can be determined by measuring the electrical half-cell potential of uncoated reinforcing steel (Stratfull et al. 1975; Finch et al. 2003). The procedure for measuring half-cell potentials is fairly simple. A half-cell, normally a copper-copper sulfate ($Cu\text{-}CuSO_4$) reference electrode (CSE), is placed on the surface of the concrete where the steel reinforcement is located (ASTM C876-99 1999). The reference electrode is then connected to the positive end of a high-input impedance voltmeter that is connected to a data-logging device. The negative end of the voltmeter is connected to the reinforcing steel being investigated. To enable the latter connection, a hole should be drilled into the concrete to expose the steel, and a screw should be tapped into the reinforcing steel so that a good electrical connection is made (Elsener 2001; Stratfull 1973; Kyung et al. 2004). In addition, a moist sponge

should be placed between the half-cell and the concrete to improve the electrical coupling between the deck and the instrument during the survey (Stratfull 1973).

Once the electrode and the reinforcing steel are adequately connected to the voltmeter, the corrosion potential of the steel reinforcement near the point of contact can be measured. A diagram of the testing equipment is shown in Figure 2-2 (Finch et al. 2003). After a large number of corrosion potential readings have been made, a contour map can be generated to delineate areas of corrosion. Measurements should be taken in a grid pattern to facilitate the drawing of equipotential lines on a two-dimensional contour map, as shown in Figure 2-3 (Stratfull 1973).

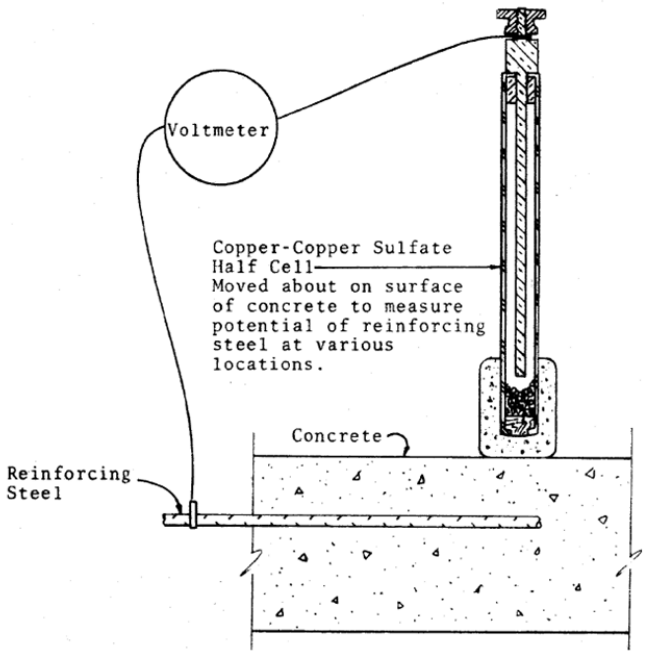

Figure 2-3 Half-cell potentiometer (Finch et al. 2003)

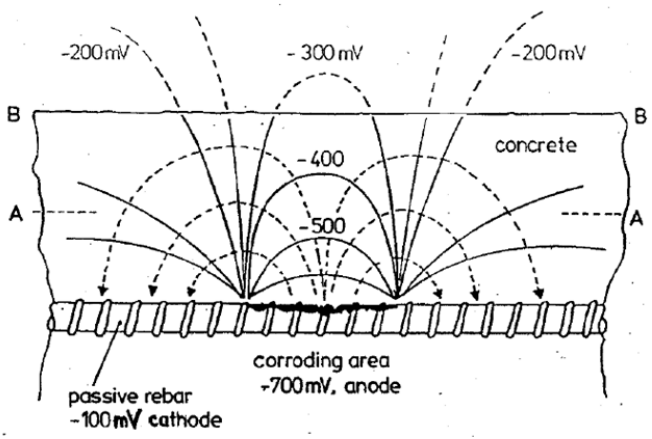

Figure 2-4 Two-dimensional contour map from half-cell potential testing

Surface potential measurements are affected by several factors, including concrete cover thickness, concrete resistivity, and polarization. As concrete cover thickness increases, the difference between the potential values of passive steel and actively corroding steel decreases. In fact, for a thick cover, the potential values become nearly identical. Therefore, locating small corroding areas becomes extremely difficult with increasing cover depth (Stratfull 1973).

As previously discussed, the resistivity of concrete is affected by concrete humidity and ion concentrations in the pore solution. Using empirical equations, researchers have shown that reduced electrical resistance of the concrete increases the current flow in the reference electrode used in half-cell potential surveys (Stratfull 1973). When surface potential measurements are performed on highly resistive concrete, however, corrosion areas can be masked. Macrocell currents are inclined to avoid the highly resistive layer, which affects potential readings in a way similar to cover depth.

ASTM C 876, Standard Test Method for Half-Cell Potentials of Uncoated Reinforcing Steel in Concrete, specifies that potential measurements more negative than −0.35 V measured with a CSE indicate a probability greater than 90 percent that corrosion is occurring. Potential

measurements more positive than −0.20 V indicate a probability greater than 90 percent that corrosion is not occurring in that area. Potential measurements between −0.20 and −0.35 V indicate that corrosion in that area is uncertain. However, studies have been conducted that conflict with these threshold values designated in ASTM C876 (ASTM C876 1999; Stratfull 1973). The studies indicate that different conditions, such as concrete moisture content, chloride content, temperature, carbonation, and cover thickness, alter the potential values that suggest active corrosion of the reinforcing steel (ASTM C876 1999; Elsener 2001; Stratfull 1973). In other words, corrosion may occur on one bridge deck at values more positive than −0.20 V, while for another it may occur at values far more negative than −0.35 V. Thus, published threshold values in ASTM C 876 should only be used as guidelines since a precise delineation of steel from a passive to an active state cannot be made to encompass all types of bridges. Engineers and technical specialists familiar with concrete materials and corrosion testing should interpret potential measurements using supplementary data and other factors necessary to accurately formulate conclusions about corrosion of reinforcing steel in concrete (Finch et al. 2003). An understanding of how various factors influence potential measurements is key to a meaningful data interpretation.

2.3 Deterioration Threshold

Healthy and deteriorated areas of a bridge deck identified with NDE are typically demarcated with a deterioration threshold, defined as the probable transition within the range of NDE data (e.g., 2.41 kohm-cm to 98.91 kohm-cm for resistivity or -36.32 dB to -8.92 dB for GPR) from unaffected to affected areas in a bridge deck (Gucunski et al. 2005). Historically, this deterioration threshold has been defined subjectively by the operator conducting the NDE measurements considering the age of bridge deck, visual deck condition, and the intensity of

NDE signal change (Gucunski et al. 2005), or by varying data from one NDE technique to obtain best graphical correlation with the other NDE mapping (Rhazi et al. 2007).

Some researchers proposed a GPR normalized reflection amplitude threshold of -10 dB, relative to the top 10% maximum reflection amplitudes, which may provide an accurate damage prediction on a selected asphalt-covered deck (Romero et al. 2000). A comparative study was also conducted between a traditional approach defining thresholds and a method removing the depth-related amplitude loss, and resulted in a better correlation between GPR prediction and the other NDE data (Barnes et al. 2008). Threshold values for NDEs measuring corrosion activity were proposed in earlier DOT researches. The threshold values of resistivity are based on the assumption that decreased electrical resistance stems from the presence of sufficient chloride concentrations to induce corrosion of the reinforcing steel. Some test results indicate the corrosion is probable to occur when resistivity measurements are between 5.08 kohm-cm and 11.94 kohm-cm, while other tests indicate that resistivity values between 5.08 kohm-cm and 9.91 kohm-cm are necessary to induce corrosion (Manning, 1985). However, a recent study concluded that these threshold values are not appropriate for general application through comparing DOT recommended criteria with data collected from twelve bridges (Guthrie and Tuttle 2006). According to ASTM Standard (ASTM Standard (C876-09 2009), potential measurements more negative than -350 mV indicate a probability greater than 90 percent that corrosion is occurring, and potential measurements more positive than -200 mV indicate a probability greater than 90 percent that corrosion is not occurring. Some researchers suggested established values did not consider concrete moisture content, chloride content, temperature and other factors, therefore these threshold values should only be used as a guideline since a precise

delineation of steel from a passive to an active state cannot be made to encompass all conditions (Elsener 2001).

2.4 Finite Element Modeling of Composite Bridges

Researchers have discussed the accuracy and application of finite element models in analyzing behavior of composite bridge structures. Discussion was mainly focused on appropriate material models, e.g., linear elastic and concrete smeared cracking, boundary conditions as well as element types.

Barth and Wu (2006) developed a series of FE models to study the ultimate load behavior of composite bridge decks using ABAQUS. Two simple-span bridge models and one continuous bridge model were included in the study. All models were three dimensional and included nonlinear material properties. Shell elements were used to model the steel girders and the concrete slab. The concrete material of the model was simulated by two alternative representations available in ABAQUS; one was the smeared crack concrete model, and one involved a concrete formulation incorporating damaged plasticity characteristics. The load and deflection curves resulting from the models were compared with experimental data. The comparison showed that the results from the smeared crack concrete deck model agreed better with the experimental data, but the authors encountered numerical convergence difficulties with this type of model when simulating the continuous, multi-span bridge.

A three-dimensional FE model was proposed by Thevendran et al. (1999) to study curved steel concrete composite beams using ABAQUS software. In his model, nine concrete slabs were modeled by four-node, thick-shell elements, and the steel flange and web were modeled using four-node, thin-shell elements. A typical element grid is shown in Figure 2-4. Rigid beam

elements were used to simulate the full composite behavior between the girders and deck. Nonlinear material properties were included in the model. This model was used to study the load-deflection relationship of the curved beam, and the results were compared with laboratory data. However, there was a large deviation between the numerical and experimental results in the nonlinear stage. The authors reasoned that the large discrepancy was due to the inadequacy in concrete modeling.

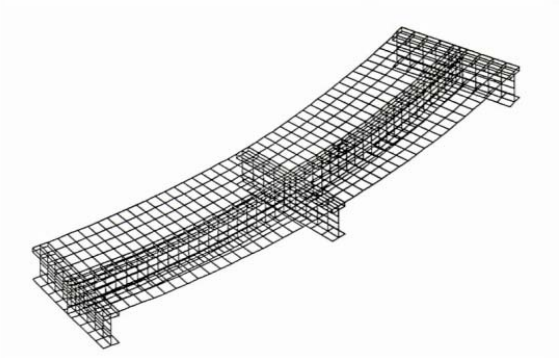

Figure 2-5 Finite Element Model with Curved Beams (Thevendran et al. 1999)

Biggs et al. (2000) developed a three-dimensional composite bridge model, shown in Figure 2-5, to predict the behavior of a RC deck under vehicle loading. In his model, the RC deck was modeled with shell elements and the steel girders were simulated using beam elements. Multiple point constraints (MPC), available in ABAQUS, were used to simulate the interaction between the slab and the girders so that these members were forced to undergo the same deformations for the degrees of freedom present at the interface. ABAQUS's smeared concrete model with tension stiffening was used to simulate the pre- and post-cracking behavior of the reinforced concrete. To verify the model, the authors tested a simply supported beam model, a RC slab model, and a single composite beam model with these model characteristics before running the final composite bridge model. The results of these four models all fundamentally agreed with

theoretical values, proving the validity of this bridge modeling technique. The limitation of this study, though, was the lack of cracking information in the results, since the post-cracking behavior had been defined in the model.

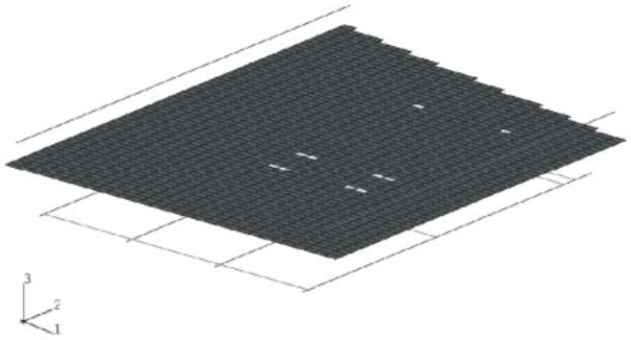

Figure 2-6 Finite Element Model with Applied Loads (Biggs et al. 2000)

2.5 Finite Element Modeling of Bridge Deck Deterioration

Lee (2011) proposed a comprehensive predictive model for the deterioration process, to predict the times associated with diffusion of chlorides, initiation of steel corrosion, and damage in the form of delamination up to the end of bridge deck service life. The essential components of this study were enhanced corrosion-induced deterioration theories, non-linear finite element analysis and Monte Carlo simulation. Parametric studies were performed in this research to quantify growth of cracking and delamination, and the Monte Carlo simulation tool was used to develop reliability data for the deterioration process. The parameters studied including clear cover depth to bridge deck, comprehensive strength of concrete, diameter of reinforcing bar and the bar spacing. The author concluded that delamination for a given bar expansion increases as bar diameter increases, and the percent delamination decreases as cover depth decreases. Good agreement was also discovered between bridge deck reliability using simulation results and the corresponding reliabilities based on NBI recorded decks from Wisconsin bridges. However, this research did not include all possible parameters that may influence reliability and service life of

bridge deck, such as average daily truck traffic (ADTT) and bridge superstructure types, and the finite element analysis was focused on component level, which is not capable to indicate system influence on deterioration process and delamination locations on bridge decks.

2.6 Finite Element Modeling of Bridge Deck Cracks

Research has been done on a three-span, continuous, skewed bridge on US 331 in Montgomery County, Alabama, to study the mechanisms that contributed to the early horizontal cracks on its bridge deck (Schindler et al. 2010). Finite element model was built to rule out excessive skew and differential support settlements, and it was concluded that horizontal early cracking was most likely caused by excessive early-age temperature gradients combined with drying shrinkage gradients which produced large shear and normal stresses at the top reinforcement mat location in concrete with high coefficient of thermal expansion and high modulus of elasticity. The majority of surface cracking discovered in this study is perpendicular to the orientation of steel girders, which indicates this cracking might be caused by the girders restraint of concrete volume changes. This research also discovered that skew angle has influence on the surface cracking. The increasing of skew of deck would increase the tensile stresses in the deck, therefore more cracking is present on deck surface, and the cracking will be parallel to the bridge skew.

Ala Saadeghvaziri and Hadidi (2005) investigated the early transverse cracking of an RC deck by developing 3D finite element models of a subassembly of the composite structure (a single girder along with its tributary deck width) using the ANSYS software package. In this model, the concrete deck was modeled using solid elements, while the girders were modeled using shell elements. The ANSYS rebar element was used to simulate the reinforcement, and the bond between concrete and rebar was also considered through a series of spring connections; a linear

elastic concrete material model was employed. Shear studs were modeled with nonlinear spring elements which connected the deck with the steel girders.

Deflection and stress at midspan were studied as they varied with varying temperature-induced shrinkage loads. A sudden jump in the deflection or stress curves was considered as an indication of transverse cracking. The boundary conditions of this 3D model were changed to study their effect on stresses and cracking of the RC deck. Other design factors such as span length, girder spacing and deck thickness were also analyzed in this study using a simplified 2D finite element model. Based on the results of the parametric study, recommendations were made regarding the composite bridge deck design. The primary recommendations were 1) construction practice should not introduce inconsistent boundary conditions on the girders, 2) the ratio of the girder and deck stiffness should be minimized to provide for the preference that the moment of inertia have a greater contribution from the deck, and 3) flexible superstructures should be employed because they have a lower tendency for deck cracking (Ala Saadeghvaziri and Hadidi 2005).

Shapiro (2006) created an ABAQUS model to study the post-cracking behavior of a damaged concrete bridge. The profile of the bridge was carefully modeled, including diaphragms, barriers rails and bearing pads. The whole bridge was modeled using 3D solid elements. Elastic material properties were selected for the bridge, with the inclusion of an equivalent modulus of elasticity applied to the concrete of the deck to approximately reflect the rebar's effect on the cracking behavior. The seam function of ABAQUS was used in the model to simulate cracks that were known to have formed in the concrete girders of the particular bridge under investigation. Several seams were assigned at the location of cracks, and during the computer analysis these seams separated and behaved like opening cracks (Shapiro 2006). The seam function is very

powerful for simulating crack propagation, but the limitation is also obvious - a predefinition of the cracked areas and crack properties is required prior to beginning the analysis.

2.7 Summary of Literature Review

Through the literature review, two questions need to be addressed according to objectives of the LTBP Program. A general and convenient procedure is required to interpret vast amount of data generated by non-destructive evaluation, as well as application of this procedure to assess bridge deck deteriorations. Besides, a reliable model should be built to study causes and process of bridge deck deteriorations, as well as to predict future deteriorations on bridge decks.

Interpretation of NDE data requires transformation of different data types and determination of deterioration thresholds in order to compare NDE results and categorize bridge deck condition. Furthermore, based on identified deterioration thresholds, data from different NDE measurements could be normalized and compared to evaluate bridge deck deteriorations.

Reinforcing steel corrosion induced deterioration is the main damage type that shortens the service life of bridge decks. The major cause of accelerated corrosion in reinforced concrete is the diffusion of chloride ions into concrete and contact with reinforcing steel. Bridge deck cracking is a serious issue because cracks allow harmful and corrosive chemicals to penetrate the concrete and deteriorate the reinforcing steel embedded in it, regardless of the bridge design type, length of spans, deck thickness and concrete mixture designs. Therefore, it is reasonable to investigate the relation between crack distribution and corrosion induced deteriorations on bridge decks. Since concrete shrinkage might be the primary causes of concrete bridge deck cracking, this research will study the correlation between shrinkage induced cracking and bridge deck deteriorations.

Chapter 3 : "A Probability-Based Threshold Definition for Non-Destructive Bridge Deck Deterioration Evaluation"

Tao Zou and Cristopher D. Moen

[To be submitted to Journal of Structural Engineering]

Abstract: This paper presents a quantitative method for defining a deterioration threshold for bridge deck non-destructive evaluation (NDE) measurements, and then demonstrates how this threshold can be used to assess bridge deck condition. The deterioration threshold is single measurement magnitude, e.g., decibels for ground penetrating radar (GPR) and volts for half-cell potential, that defines the probable transition between healthy and deteriorated areas of a bridge deck. This binary characterization (0 for healthy, 1 for deteriorated) can be used to quantify correlation between different types of NDE results, providing a richer understanding of bridge deck deterioration than traditional qualitative techniques. In the method, a probability based definition is introduced to determine the deterioration threshold for a general set of NDE measurement data with a specified level of confidence, then spatially distributed NDE data are mapped to a binary system by identified thresholds. The calculation of a GPR deterioration threshold is demonstrated with data measured on Virginia and New York Pilot Bridges within the Federal Highway Administration's Long Term Bridge Performance Project. Potential uses for the identified thresholds are then demonstrated including overlapping binary NDE mappings to study deterioration correlation, and comparing delaminated areas identified with GPR to other NDE techniques.

Author keywords: Bridge deck, Deterioration, Nondestructive evaluation, Deterioration threshold, Assessment

3.1 Introduction

High fidelity non-destructive evaluation (NDE) methods, for example ground penetrating radar (GPR) and half-cell potential, are now widely used by transportation departments (DOTs) to locate and quantify bridge deck deterioration. These modern methods can complement or replace traditional lower fidelity NDE techniques like chain drag that rely on someone listening for 'hollow' sounds to identify areas where the bridge deck has delaminated from the reinforcing steel top layer (Maierhofer et al. 2010). High fidelity NDE produces volumes of data that can redefine the way we approach bridge deck design and rehabilitation – but only if we have the analytics to unlock important trends. Different NDE techniques with different physics, when considered together, can be used to identify direct links between bridge deck durability and initial design decisions, e.g., concrete mix design, steel girder spacing, or concrete cover depth. The research summarized herein introduces a new method for interpreting different types of NDE data together, within a common framework.

Non-destructive bridge deck evaluation techniques like GPR, which detect voids and delamination with an electromagnetic pulse (Belli et al. 2008; Roberts 1995), and half-cell potential, which identifies reinforcing steel corrosion by measuring the concrete electrical potential (Elsener 2001; Kyung et al. 2004), provide spatially vivid information. However interpretation of measured return signals is complicated for engineers and practitioners, and may require information by destructive methods (Scott et al. 2001; Yehia et al. 2007). The applicability of a certain NDE approach depends on the type of bridge deck deterioration, for example, rebar corrosion should be measured with half-cell potential and delamination with GPR (Gucunski et al. 2013). NDE techniques are typically not combined for bridge deck condition assessment because there are no established protocols for comparing data representing different

underlying durability physics, e.g., rebar corrosion, live load abrasion and impact, or concrete shrinkage. Individually these data sets can provide meaningful insight on current and future deteriorations, and it is hypothesized in this manuscript, that considering them together is even more powerful.

NDE data interpretation is challenging, especially linking deterioration to certain bridge deck and superstructure characteristics that could be modified in future designs to extend service life. The research summarized herein takes a small step towards addressing this challenge by introducing a probability-based method for interpreting NDE data. The approach defines an NDE threshold magnitude that establishes deteriorated locations on a bridge deck for a certain confidence level. This approach can be generally applied to any NDE technique, bringing different NDE data sets into a common representation for combination and study. This probability-based deterioration threshold approach is demonstrated with GPR measurements recorded on Virginia and New York Pilot Bridges studied in the Federal Highway Administration's (FHWA) Long Term Bridge Performance (LTBP) Program. Deterioration mappings for chain drag, GPR and half-cell potential are overlaid to explore correlation between delamination and rebar corrosion. The manuscript begins by defining the framework for calculating a probability-based deterioration threshold.

3.2 Probability-Based Deterioration Threshold Definition

On a bridge deck, healthy and deteriorated areas identified with NDE are typically demarcated with a deterioration threshold, defined as a single magnitude within the NDE data range (e.g., -17 dB for GPR or -0.35 Volts for half-cell potential). For NDE measurements beyond this threshold, there is a high probability of deterioration. This deterioration threshold is most often defined subjectively, by the NDE operator, considering bridge deck age, visual deck condition,

and the NDE signal change intensity (Gucunski et al. 2005). Another approach for defining this threshold is to vary the threshold magnitude for one NDE technique to obtain the best graphical deterioration correlation with another NDE mapping (Rhazi et al. 2007). Deterioration threshold ranges can also be assigned to a specific NDE method, for example, between 5.1 kohm-cm and 9.9 kohm-cm for resistivity (Manning 1985). Unfortunately, these thresholds are typically established from project-specific data and are not appropriate for general application (Guthrie and Tuttle 2006).

Suppose instead that a general set of NDE measurements on a bridge deck $\{X_{DECK}\}$ is collected, with the distribution (histogram) shown in Figure 3-1(a). The end user (DOT, engineer) would like to know, with a certain confidence level which locations on the deck are deteriorated (D), i.e., $\{ D \subset X_{DECK} \}$. In this case, the deteriorated NDE measurement group $\{D\}$ is defined by the threshold T_D, where $\{D\} = \{X_{DECK} < T_D\}$.

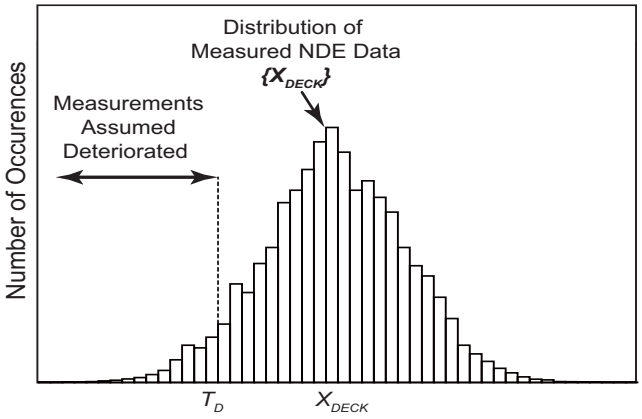
Distribution of
Measured NDE Data
{X_DECK}
Measurements
Assumed
Deteriorated
Number of Occurences
T_D
X_DECK

(a)

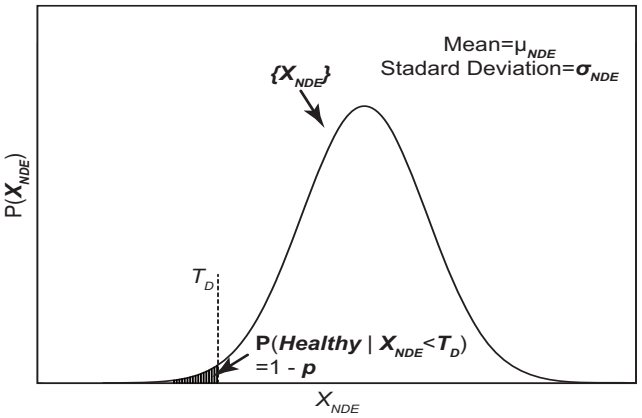
Mean=μ_NDE
Stadard Deviation=σ_NDE
{X_NDE}
P(X_NDE)
T_D
P(Healthy | X_NDE<T_D)
=1 - p
X_NDE

(b)

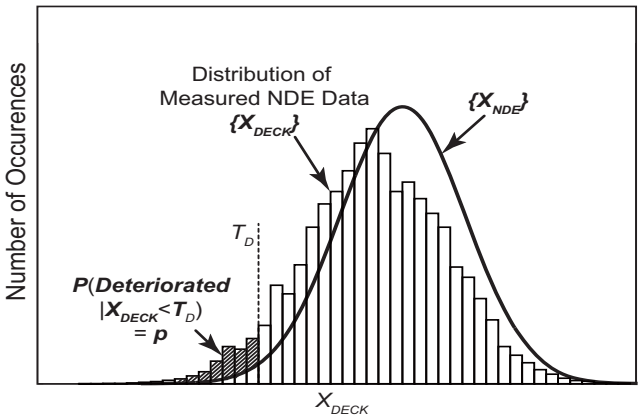
Distribution of
Measured NDE Data
{X_DECK}
{X_NDE}
Number of Occurences
T_D
P(Deteriorated
|X_DECK<T_D)
= p
X_DECK

(c)

Figure 3-1 NDE measurement histogram for a typical bridge deck (a), NDE data distribution for a bridge without deteriorations (b) and (c) the deterioration threshold, T_D, with a confidence level p

The threshold T_D is calculated for Gaussian-distributed NDE data as

$$T_D = \mu_{NDE} + z(1-p)\sigma_{NDE} \tag{3-1}$$

where p is the threshold confidence level, i.e., the probability that a location on the bridge deck identified as deteriorated is actually deteriorated, μ_{NDE} and σ_{NDE} are the measurement bias and variability for a specific NDE technique as shown in Figure 3-1(b), and $z(1 - p)$ is obtained from a standard normal distribution table (Weiss 2005). The threshold definition in Eq. (3-1) can be most easily explained by studying Figure 3-1(c), which overlays NDE measurements including deterioration to NDE measurement distribution that would be collected on a perfectly 'healthy' bridge. The hypothesis is that the percentage of deterioration false positives less than T_D, i.e., bridge locations that were predicted as deteriorated but that are actually not deteriorated, is defined by the $\{X_{NDE}\}$ distribution tail.

For example, an engineer looking to study areas of possible bridge deck deterioration with a certain NDE method might select p=0.90, meaning there is a 90% chance that an NDE measurement within $\{D\} = \{X_{DECK}<T_D\}$ is actually deteriorated. In other words, the conditional probability $P(Deteriorated \mid X_{DECK}<T_D)=p$. If the conditional probability is rewritten as $P(Deteriorated \mid X_{DECK}<T_D)=1- P(Healthy \mid X_{DECK}<T_D)$, then $P(Healthy \mid X_{DECK}<T_D)=1-p$. The threshold is calculated with Eq. (3-1) assuming that $P(Healthy \mid X_{DECK}<T_D)= P(Healthy \mid X_{NDE}<T_D)$, which is represented as the (white) area under the $\{ X_{NDE}\}$ distribution in Figure 3-1(c).

The NDE statistics μ_{NDE} and σ_{NDE} should ideally be calculated for each NDE method and each bridge based on bridge deck condition field measurements and measurement equipment parameters. For example, theoretical GPR readings are a function of concrete relative permittivity, magnetic permeability and electrical conductivity, as well as pore water temperature and GPR antenna frequency (Halabe et al. 1989). The next section shows how Eq. (3-1) can be applied to GPR data collected on bridges in the eastern U.S.

3.3 Pilot Bridge Study Employing GPR Deterioration Thresholds

The deterioration threshold methodology presented previously is applied to two sets of GPR bridge deck data measured on pilot bridges in Virginia and New York for the Federal Highway Administration's (FHWA) Long Term Bridge Performance Study (Ghasemi et al. 2009). These bridges were selected because concrete porosity, pore water saturation and chloride concentration were directly measured which are all parameters needed to approximate the GPR $\{X_{NDE}\}$ statistics μ_{NDE} and σ_{NDE}.

The Virginia pilot bridge, located in Haymarket, VA on U.S. Route 15 over Interstate 66, is a two-span continuous bridge with six variable depth built-up steel girders (Figure 3-2(a)) spaced at 2.3m (7ft-6in.) center-to-center (Collins 2010). The New York pilot bridge, located in Almond, NY on NY Route 21 over the Karr Valley Creek, is an adjacent concrete box girder bridge with varying girder width as shown in Figure 3-2(c). It has two simple spans made continuous with a cast-in-place concrete diaphragm over the center pier. Pilot bridge ages, annual average daily traffic (AADT), and deck conditions are summarized in Table 3-1.

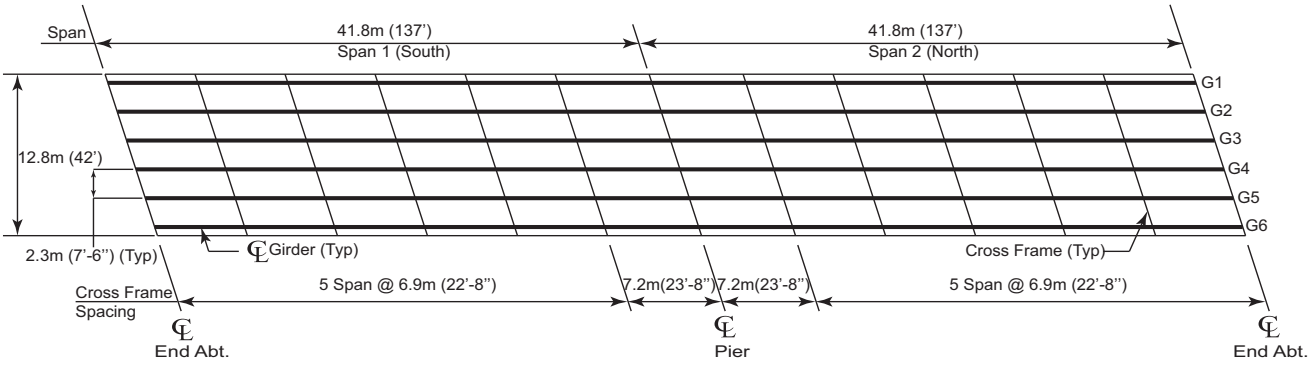

(a)

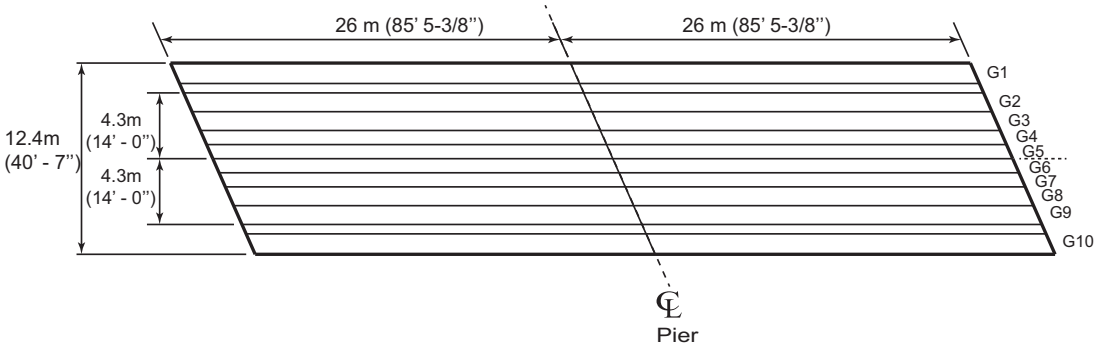

(b)

Figure 3-2 Pilot bridge plan views for (a) Virginia and (b) New York

Table 3-1 Pilot bridge age, condition, and geometry

Pilot Bridge	Year Built	Span (m)	NBI Deck Rating	AADT	Skew (degree)
Virginia	1979	83.5	6(Satisfactory)	16,500	17
New York	1990	52	7(Good)	8,700	24

3.4 GPR Attenuation Calculations

The goal in this section is to define equations for calculating the theoretical GPR attenuation so that GPR measurement bias and variability for a 'healthy' bridge, i.e., μ_{NDE} and σ_{NDE}, can be determined. Ground penetrating radar identifies bridge deck deterioration with a short pulse of electromagnetic energy transmitted into the reinforced concrete slab, which is then reflected back

at different amplitudes depending upon the slab density and uniformity. The density varies because of top and bottom rebar grids, variations in concrete properties, and concrete delamination from rebar (Breysse 2012). A reflected signal, measured with a receiving antenna, loses energy as it passes through the bridge deck. The theoretical GPR signal attenuation, $A=-\alpha d$, is the loss in electromagnetic energy in decibels (dB), where α is the attenuation coefficient in dB/m and d is the signal traveling path distance in meters. (The negative sign represents a loss in electromagnetic energy.)

3.4.1 GPR Attenuation Loss

GPR energy loss (signal attenuation) varies with concrete material properties, GPR antenna frequencies and if there is delamination and deteriorations. The material 'scattering' energy losses are typically small for healthy concrete because the aggregate particle size is much smaller than the electromagnetic wavelength (Olhoeft 1998), and therefore larger dimension inhomogeneities, e.g., delamination, can be identified when plotting signal attenuation contours over a bridge deck.

Variability in the attenuation, A, comes from the attenuation coefficient α which is a function of the concrete medium electrical and magnetic properties (Halabe et al. 1989)

$$\alpha = 8.686 \times \omega \times \left[\frac{\varepsilon' \mu_0}{2} \left[\sqrt{1 + \left(\frac{\sigma}{\omega \varepsilon_r' \varepsilon_0} \right)^2} - 1 \right] \right]^{1/2} \qquad (3\text{-}2)$$

where ω is the angular frequency ($2\pi f$) in rads/s, f is the electromagnetic frequency in Hz, and σ is the concrete conductivity in S/m. As a dielectric material, concrete electromagnetic properties can be characterized by the complex permittivity ε and the complex magnetic permeability μ. However, most common dielectric materials including concrete are nonmagnetic, making the

permeability μ very close to the permeability of free space, where $\mu_0 = 4\pi$ x 10^{-7} Henry/m (Rhim and Buyukozturk 1998). The complex permittivity can be defined as $\varepsilon = \varepsilon^{'} + i\varepsilon^{''}$ in Farad/m where $\varepsilon^{'}=\varepsilon^{'}_r\varepsilon_0$ is the real part of the complex permittivity and $\varepsilon^{''}=\varepsilon^{''}_r\varepsilon_0$ is the imaginary part of the complex permittivity, and the dielectric permittivity of free space, ε_0, is 8.854 x 10^{-12} Farad/m. $\varepsilon_r = \varepsilon^{'}_r + i\varepsilon^{''}_r$ is the relative complex permittivity, where $\varepsilon^{'}_r$ is the real part of the relative complex permittivity or dielectric constant, and $\varepsilon^{''}_r$ is the imaginary part of the complex permittivity or loss factor. The real part of the relative complex permittivity $\varepsilon^{'}_r$ represents the ability of a material to polarize, support polarization, and store energy in response to an external electrical field (Olhoeft 1998, Baker et al. 2007), and the imaginary part of the relative complex permittivity $\varepsilon^{''}_r$ is a measure of how dissipative or lossy a material is to an external electric field and is referred as the relative loss factor (Rhim and Buyukozturk 1998). . These variables that define α can be calculated as described in the following subsections.

3.4.2 Concrete Relative Permittivity

Concrete relative permittivity, $\varepsilon_r = \varepsilon^{'}_r + i\varepsilon^{''}_r$,, is a dimensionless complex quantity and a primary variability source in GPR attenuation. It varies with concrete porosity, saturation, and chloride content (Feng and Sen 1985)

$$\sqrt{\varepsilon_r} = (1-\phi)\cdot\sqrt{\varepsilon_m} + (1-S)\cdot\phi\cdot\sqrt{\varepsilon_a} + \phi\cdot S\cdot\sqrt{\varepsilon_{sw}} \qquad (3\text{-}3)$$

where ϕ is concrete porosity defined as (volume of voids)/(total volume of concrete) which varies from 0.1 for newly cast concrete (Popovics 1985) increasing to 0.2 over time because of freeze-thaw cycles. The degree of saturation, S, defined as (volume of water)/(volume of voids), varies through the bridge deck depth, however for these GPR studies, the top 25 to 50 mm is most important, where S ranges from 0.40 to 0.50 in warm summer months and to a higher number in cold winter months (Carrier et al. 1975). The relative dielectric permittivity of

concrete solids (real quantity), ε_m, is typically considered as 5.0 (Halabe et al. 1989), and ε_a=1.0 is the relative dielectric permittivity of air (real quantity). A key parameter in Eq. (3-3) is ε_{sw}, the relative complex dielectric permittivity of water, which also consists of real and imaginary components (Ulaby et al. 1986). ε_{sw} can be solved by Eqs. (3-4) to (3-17), further the complex relative permittivity $\varepsilon_r = \varepsilon'_r + i\varepsilon''_r$ is calculated by solving the complex equation (3-3).

$$\varepsilon_{sw} = \varepsilon'_{sw} + i \cdot \varepsilon''_{sw} \tag{3-4}$$

where

$$\varepsilon'_{sw} = \varepsilon_{sw\infty} + \frac{\varepsilon_{sw0} - \varepsilon_{sw\infty}}{1 + (2\pi \cdot f \cdot \tau_{sw})^2} \tag{3-5}$$

and

$$\varepsilon''_{sw} = \frac{2\pi \cdot f \cdot \tau_{sw} \cdot (\varepsilon_{sw0} - \varepsilon_{sw\infty})}{1 + (2\pi \cdot f \cdot \tau_{sw})^2} + \frac{\sigma_i}{2\pi \cdot f \cdot \varepsilon_0} \tag{3-6}$$

The relative permittivity of saline water at infinite frequency (dimensionless), $\varepsilon_{sw\infty}$, is typically assumed as 4.9 for concrete (Stogryn 1971), and the static relative permittivity of saline water (dimensionless), ε_{sw0}, is defined as

$$\varepsilon_{sw0}(T, N_{sw}) = \varepsilon_{sw0}(T,0) \cdot a_1(N_{sw}) \tag{3-7}$$

where T is the saline water temperature in degree Celsius and the normality of saline water, N_{sw} is

$$N_{sw} = S_{sw} \cdot (1.707 \times 10^{-2} + 1.205 \times 10^{-5} \cdot S_{sw} + 4.058 \times 10^{-9} \cdot S_{sw}^2) \tag{3-8}$$

with the initial condition

$$\varepsilon_{sw0}(T,0) = 88.045 - 0.415 \cdot T + 6.295 \times 10^{-4} \cdot T^2 + 1.075 \times 10^{-5} \cdot T^3 \tag{3-9}$$

and parameter

$$a_1(N_{sw}) = 1.0 - 0.255 \cdot N_{sw} + 5.15 \times 10^{-2} \cdot N_{sw}^2 - 6.89 \times 10^{-3} \cdot N_{sw}^3 \quad (3\text{-}10)$$

The salinity, S_{sw}, of a salt solution is defined as the total mass of solid salt in grams dissolved in one kilogram of the aqueous solution, and is expressed in parts per thousand (*ppt*) by weight. The salinity of pore water in concrete bridge decks is typically not directly measured, but determined indirectly by free chloride and moisture content. To convert the percentage chloride content to a NaCl (sodium chloride) equivalent, a multiplication factor of 1.65, equal to the ratio of molecular weight of NaCl (58.5) to the atomic weight of chloride (35.5), is applied (Halabe et al. 1989). The pore water salinity is then determined by dividing the NaCl equivalent of the free chloride content by the corresponding moisture content.

For example, considering the Virginia pilot bridge, the mean percent chloride content is calculated by dividing the mean chloride concentration (1.7 kg/m^3, Table 3-2) by the concrete density (2100 kg/m^3). The percent chloride content is then converted to its NaCl equivalent multiplying by 1.65, and divided by the moisture content (4%) to obtain the pore water salinity.

The relaxation time of saline water (seconds), τ_{sw}, is related to the normality of saline water (N_{sw}) and water temperature (T) as

$$\tau_{sw}(T, N_{sw}) = \tau_{sw}(T,0) \cdot b_1(T, N_{sw}) \quad (3\text{-}11)$$

$$2\pi \cdot \tau_{sw}(T,0) = 1.111 \times 10^{-10} - 3.824 \times 10^{-12} \cdot T + 6.938 \times 10^{-14} \cdot T^2 - 5.096 \times 10^{-16} \cdot T^3 \quad (3\text{-}12)$$

$$b_1(T, N_{sw}) = 1.0 + 0.146 \times 10^{-2} \cdot T \cdot N_{sw} - 4.896 \times 10^{-2} \cdot N_{sw} - 2.97 \times 10^{-2} \cdot N_{sw}^2 + 5.64 \times 10^{-3} \cdot N_{sw}^3 \quad (3\text{-}13)$$

where σ_i is the ionic conductivity of the aqueous saline solution (S/m). The ionic conductivity of the aqueous saline solution is expressed as:

$$\sigma_i(T, N_{sw}) = \sigma_i(25, N_{sw}) \cdot c_1(\Delta, N_{sw}) \tag{3-14}$$

$$\sigma_i(25, N_{sw}) = N_{sw}(10.39 - 2.378 \cdot N_{sw} + 0.683 \cdot N_{sw}^2 - 0.135 \cdot N_{sw}^3 + 1.01 \times 10^{-2} \cdot N_{sw}^4) \tag{3-15}$$

$$\begin{aligned} c_1(\Delta, N_{sw}) &= 1.0 - 1.96 \times 10^{-2} \cdot \Delta + 8.08 \times 10^{-5} \cdot \Delta^2 \\ &- N_{sw} \cdot \Delta[3.02 \times 10^{-5} + 3.92 \times 10^{-5} \cdot \Delta + N_{sw}(1.72 \times 10^{-5} - 6.58 \times 10^{-6} \cdot \Delta)] \end{aligned} \tag{3-16}$$

$$\Delta = 25 - T \tag{3-17}$$

3.4.3 Concrete Electrical Conductivity

Electrical conductivity is a measure of the ease of electron movement within a material under the influence of an external electrical field (Saarenketo 1998). Electrical current can propagate through rock and minerals through three methods, which are ohmic, electrolytic or dielectric (Ulaby 2010). Electrolytic conduction requires the presence of irons to carry the charge, such as those found dissolved in groundwater, and therefore electrolytic conduction is the dominant process in moist or wet material, such as concrete. According to Archie's law, electrolytic conduction is dependent on pore fluid porosity and conductivity (Archie 1942):

$$\sigma = a \cdot \phi^m \cdot S^n \cdot \sigma_i + \sigma_c \tag{3-18}$$

where the empirical constants a ranges from 0.4 to 2, m ranges from 1.3 to 2.5 and n=2. σ_i is defined in Eq. (3-14) and σ_c is the surface conductivity of soil matrix in S/m.

One challenge with calculating concrete electrical conductivity using Archie's Law is this formulation was initially defined for rock, and the empirical constants, a, m and n are defined subjectively and vary for different concrete types (Nokken and Hooton 2008, Wong et al. 1984). Alternatively, the concrete conductivity can be re-written as (Rhim and Buyukozturk 1998):

$$\sigma = (\varepsilon_r^{'} \varepsilon_0 \tan\delta)\omega \tag{3-19}$$

and

$$\tan\delta = \frac{\varepsilon_r''}{\varepsilon_r'} \tag{3-20}$$

is the loss tangent.

The GPR attenuation parameter calculations are quite involved, however now that they are defined in Eqs. (3-2) to (3-20), measurement variability can be approximated as described in the next section which is the key to defining T_D and probable areas of deterioration on a bridge deck.

3.5 GPR Measurement Bias and Variability

With the theoretical GPR attenuation equations defined, μ_{NDE} and σ_{NDE} for the signal attenuation A can now be calculated. The relationship between A and concrete deck parameters is nonlinear, and so Monte Carlo simulation is warranted to construct an attenuation distribution from which μ_{NDE} and σ_{NDE} can be calculated. Concrete porosity ϕ, chloride concentration, pore water salinity S_{sw}, saturation S, and concrete clear cover depth d are treated as normal random variables. Their properties were all measured on the pilot bridge decks, with mean and standard deviations summarized in Table 3-2. Randomly generated values are input into Eqs. (3-3) and (3-8), along with assuming a deterministic value for water temperature T as 20 degree Celsius which is then input into Eqs. (3-9), (3-12), (3-13) and (3-17). The antenna frequency is also assumed deterministic at 1.5 GHz, resulting in the distribution for A shown in Figure 3-3 for the pilot bridges.

Table 3-2 GPR signal attenuation statistics for the pilot bridges

Property	Virginia Bridge		New York Bridge	
	μ_{NDE}	σ_{NDE}	μ_{NDE}	σ_{NDE}
Porosity (ϕ) (%)	15.9	1.0	11.6	0.9
Chloride Concentration (kg/m^3)	1.7	1.0	2.9	1.7
Pore Water Salinity (S_{sw}) (*ppt*)	33.4	20.2	56.5	33.1
Saturation (S) (%)	80.3	9.7	76.0	3.0
Clear Concrete Cover Depth (d) (mm)	57.0	6.9	55.0	7.0

The Monte Carlo simulation results for the three pilot bridges show that the measurement distribution is close to the Gaussian distribution. This means that simulation is not needed, and that the mean and standard deviation of the concrete properties in Table 3-2 can be used directly to calculate μ_{NDE} and $\sigma_{NDE.}$.

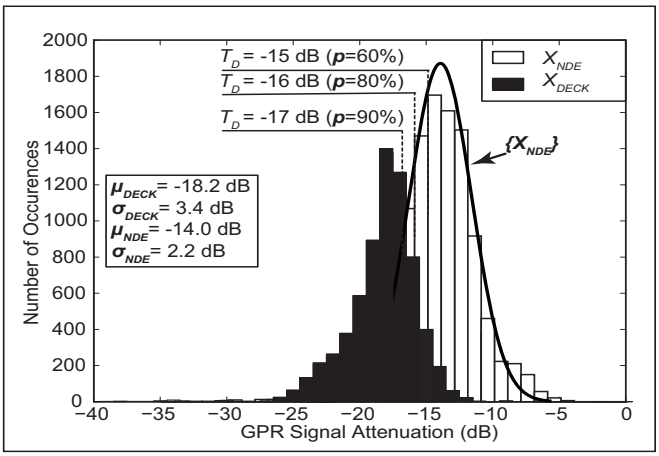

(a)

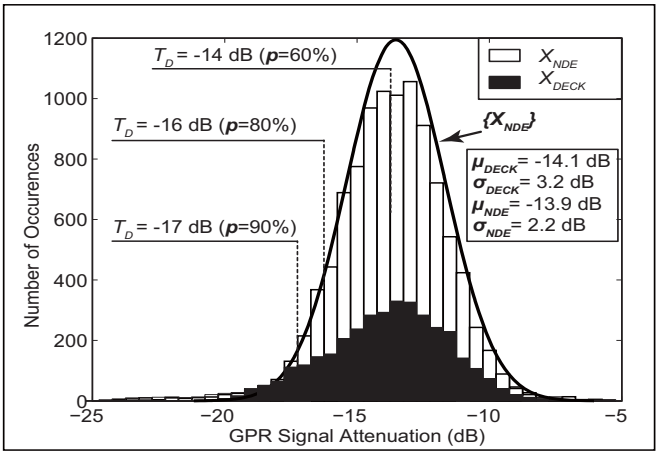

(b)

Figure 3-3 Monte Carlo simulation and deterioration thresholds of (a) Virginia and (b) New York pilot bridges

3.6 GPR Deterioration Threshold

Substituting the GPR measurement mean and standard deviation, μ_{NDE} and σ_{NDE}, and z-values into Eq. (3-1) for specified confidence levels, the deterioration threshold, T_D, is calculated and summarized in Table 3-3, together with empirical deterioration thresholds determined at the maximum GPR signal change intensity (Romero et al. 2000). Considering the Virginia pilot bridge for p=0.90, if measured GPR signal attenuation is more negative than -17 dB, there is a 90%

chance that concrete at the testing locations is truly deteriorated, and a 10% chance that concrete at testing locations is not deteriorated. Instead of a fixed threshold value, this method allows end users to specify demanding confidence levels and calculate corresponding deterioration threshold values; when combined with DOT's criteria on bridge deck replacement, this method provides more accurate estimations on deteriorated areas on bridge decks than traditional empirical way.

Table 3-3 Deterioration threshold values at specified confidence levels

Confidence Levels	$z(1\text{-}p)$	T_D (dB)	
		Virginia	New York
90%	-1.28	-17	-17
80%	-0.85	-16	-16
60%	-0.50	-15	-14
Empirical	na	-18	-14

3.7 Half-Cell Potential Deterioration Threshold

Half-cell potential measures embedded reinforcing steel potential relative to a reference half-cell placed on concrete surface. The measured potential difference can be used to determine reinforcement steel corrosion in immediate regions of test locations, with concrete as an electrolyte. Theoretical deterioration thresholds of half-cell potential data are determined according to ASTM C876, which indicates that for potential measurements more negative than -0.35 V, there is a probability greater than 90 percent that corrosion is occurring in that area; while for potential measurements more positive than -0.2 V, non-corrosion probability is greater than 90%. Although some studies showed conflicts with ASTM C876 threshold values (Stratfull 1973; Elsener and Bohni 1990), these values reported in the DOT surveys are consistent with ASTM C876 (Hema et al. 2004). In this study, threshold values reported by ASTM C876 with a 90% confidence level will be used to compare with other NDE results and the percentage of deteriorated areas with -0.35 V as threshold value are 31% and 84% for Virginia and New York pilot bridges, respectively.

3.8 Bridge Deck Condition Assessment

Due to the fact that NDE techniques are detecting various defects by measuring different underlying physics, e.g., GPR measures electromagnetic energy loss and half-cell potential measures electrical potential, NDE results are typically difficult to be combined in assessing bridge deck condition. By introducing definition of probability-based deterioration thresholds, all NDE data could be represented by a binary type, making direct comparisons possible. In this section, the deck condition of Virginia pilot bridge is assessed as a case study by combining chain drag, GPR and half-cell potential measurements.

For NDE techniques discussed in this paper, each of them shows either qualitative (chain drag) or quantitative (GPR and half-cell potential) data presented on different measuring grids. To evaluate these NDE data on an even playing field, it is necessary to transform results to the type and coordinate system that could be compared directly. Therefore, all measured data are normalized by deterioration thresholds into binary types with '1' for 'deteriorated' or '0' for 'healthy'. Meanwhile, all data are transferred onto a same planar coordinate system with 0.6-m (2-ft) grids coincident with chain drag onsite measurement, thus bridge deck condition could be represented by discrete points on this coordinate system to conduct point-to-point comparisons. Linear two-dimensional interpolation is used to transfer quantitative NDE data, i.e., GPR and half-cell potential data, from their original coordinate system to this planar coordinate system. In Figure 3-4, chain drag measurements are represented by the discrete points and GPR and half-cell potential data are converted to binary type by deterioration thresholds with the 90% confidence level. Chain drag deterioration mapping by discrete points is compared with original evaluation as in Figure 3-4(a), and it is shown that deterioration mapping by discrete points is an appropriate approximation of chain drag evaluation.

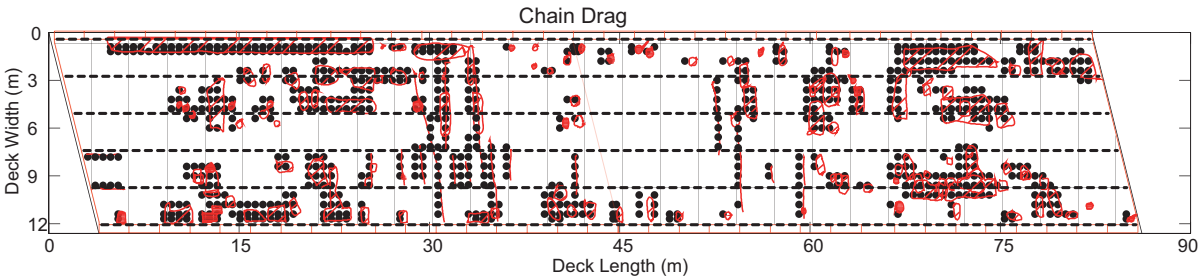

(a)

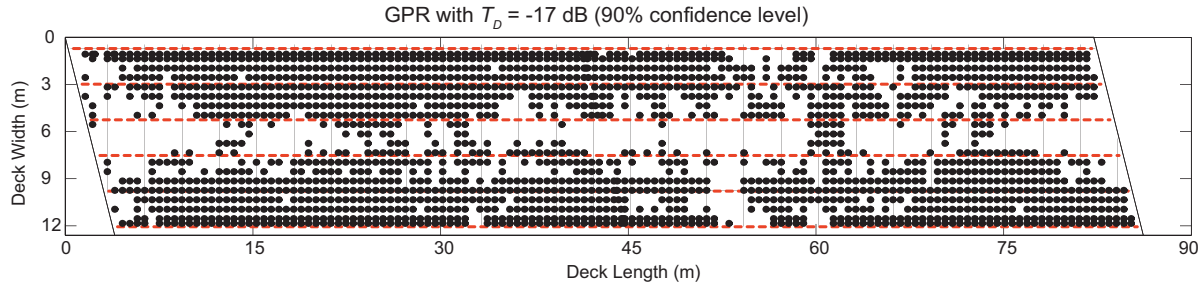

(b)

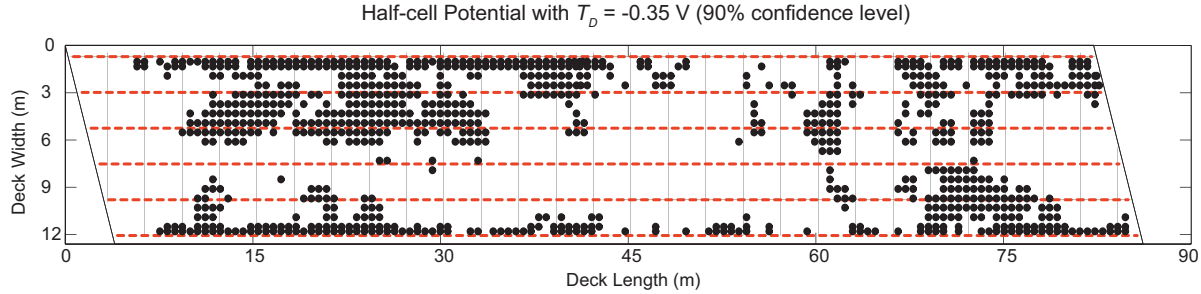

(c)

Figure 3-4 Binary mapping of bridge deck deterioration by (a) chain drag (b) GPR and (c) half-cell potential

After NDE data are normalized by deterioration thresholds with specified confidence levels and transferred onto a same coordinate system, the bridge deck condition could be assessed by overlapping deteriorated points. Overlapping of deteriorated points is able to highlight locations with more possible deteriorations, e.g., locations identified as deteriorated by both NDE evaluations, as well as locations with potential future deteriorations, e.g., locations identified as

deteriorated by individual NDE evaluation. However, instead of simply overlapping all NDE measurements, the assessments are divided into two categories based on features of NDE techniques. One category is for NDE measures similar defect types, e.g., chain drag and GPR, which both measure concrete delamination; the other category is for GPR and half-cell potential, where GPR measures existing concrete delamination, while half-cell potential measures rebar corrosion which may cause future concrete deteriorations. In Figure 3-5(a), bridge deck conditions are assessed by combining qualitative measurement, i.e., chain drag, and quantitative measurement, i.e., GPR. In this plot, the deterioration at each point is indicated by gray scale, where dark colors indicate regions identified as deteriorated by both NDE techniques, while light colors indicate regions identified as deteriorated by either NDE technique. By comparing with GPR contour mapping (Figure 3-5(b)), it is obvious that locations with most possible deteriorations, i.e., white and red areas in Figure 3-5(b), are pointed out by both NDEs, and locations identified by single NDE are marked with less possibility of deterioration.

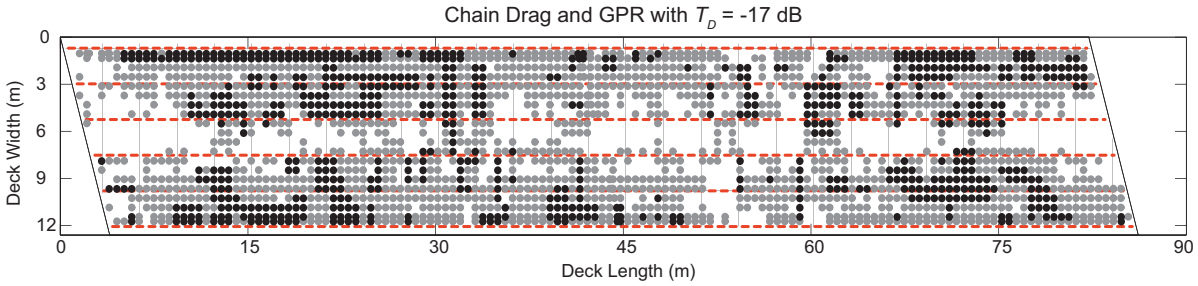

(a)

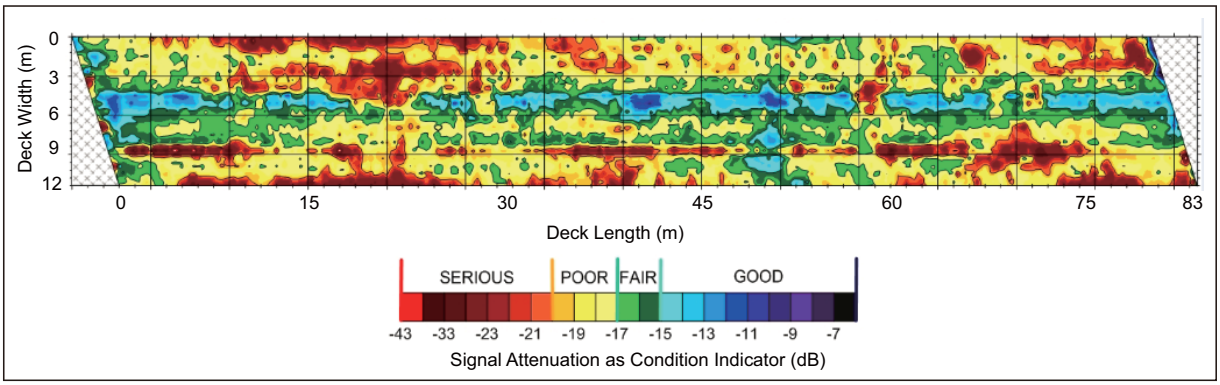

(b)

Figure 3-5 Contour mapping by (a) overlapping chain drag and GPR and (b) GPR (Rutgers University 2009)

Concrete delamination allows harmful chemicals to penetrate and corrode reinforcing steel (Breysse 2012), therefore delaminated areas on a bridge deck have high potential of future reinforcing steel corrosion. In Figure 3-6, deteriorated locations identified by GPR and half-cell potential both with a 90% confidence level are overlaid. The overlaid points indicate locations with both concrete delamination and rebar corrosion, and grey points are locations with existing concrete deterioration that may cause future corrosion of reinforcing steel.

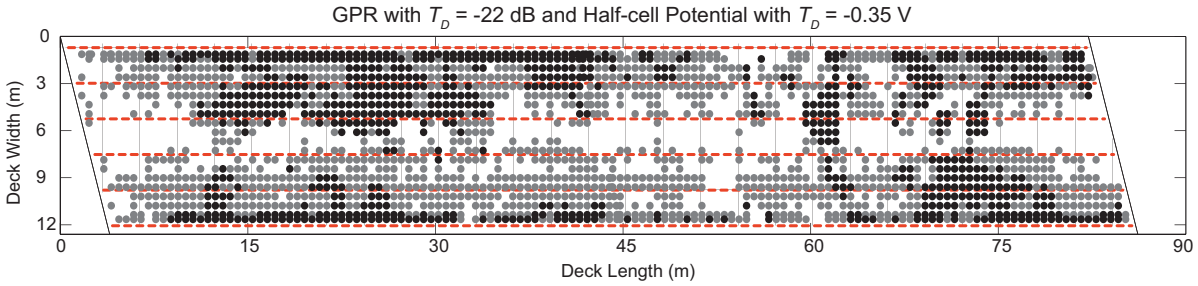

Figure 3-6 Assessment of bridge deck condition by overlapping GPR and half-cell potential

3.9 Conclusion

This paper presents a general probability-based method to identify deterioration thresholds for NDE measurements with quantitative results, and uses defined thresholds to assess bridge deck condition. This probability-based threshold definition allows end users to specify desired confidence level, and identify 'truly' deteriorations with respective probability. Concrete properties, environmental factors and NDE equipment properties are used to develop statistical distribution of measured NDE underlying physics for healthy concrete, and this features the link between fictitious bridge decks with all healthy concrete and actual bridge decks. Bridge decks are assessed by overlapping different NDE measurements at discrete points. Assessments are conducted for two groups, for NDE techniques measuring similar or different underlying physics. For both cases, overlapping NDE data is capable to identify most possible deterioration areas, as well as locations with potential future deteriorations.

In future research, in order to obtain a more accurate estimation of GPR signal attenuation distribution, the concrete porosity, saturation and chloride content should be measured on more locations to get better representation of the statistical distributions.

Acknowledgement

This publication was supported by a subcontract from Rutgers University, Center for Advanced Infrastructure & Transportation (CAIT), under DTFH61-08-C-00005 from the U.S. Department of Transportation – Federal Highway Administration (USDOT-FHWA). Researchers from the Virginia Center for Transportation Innovation and Research (VCTIR) and Virginia Department of Transportation (VDOT) also contributed to the presented research.

Notation

The following symbols are used in this paper:

A = magnitude of electromagnetic signal attenuation in dB

D = measured NDE data representing deteriorated concrete

S = degree of saturation = (volume of water)/(volume of voids)

T = saline water temperature in degree Celsius

T_D = deterioration threshold

X_{DECK} = measured NDE data on a bridge deck

X_{NDE} = theoretical measured physics of healthy concrete

a = constant (0.4-2)

d = signal traveling path distance in meter

e = base of the natural logarithm

f = electromagnetic frequency in Hz

m = constant (1.3-2.5)

n = constant (~2)

p = probability that X_{NDE} is less than T_D

α = attenuation coefficient in dB/m

ε = dielectric permittivity of concrete mixture in Farad/m (complex quantity)

ε' = real part of dielectric permittivity of concrete mixture in Farad/m

ε'' = imaginary part of dielectric permittivity of concrete mixture in Farad/m

ε_0 = dielectric permittivity of free space = 8.854 x 10^{-12} Farad/m

ε_a = relative dielectric permittivity of air = 1.0

ε_m = relative dielectric permittivity of concrete solids = 5.0

ε_r = relative dielectric permittivity of concrete mixture (complex quantity)

ε'_r = real part of relative dielectric permittivity of concrete mixture (dimensionless)

ε''_r = imaginary part of relative dielectric permittivity of concrete mixture (dimensionless)

ε_{sw} = relative complex dielectric permittivity of water (complex quantity)

ε'_{sw} = real part of relative complex dielectric permittivity of water (dimensionless)

ε''_{sw} = imaginary part of relative complex dielectric permittivity of water (dimensionless)

ε_{sw0} = static relative permittivity of saline water (dimensionless)

$\varepsilon_{sw\infty}$ = relative permittivity of saline water at infinite frequency (dimensionless)

μ_0 = magnetic permeability of free space = 4π x 10^{-7} Henry/m

σ = concrete conductivity in S/m.

σ_c = surface conductivity of concrete in S/m

σ_i = pore fluid conductivity in S/m

τ_{sw} = relaxation time of saline water in seconds

ϕ = porosity of concrete = (volume of voids)/(total volume of concrete)

ω = angular frequency ($2\pi \cdot f$) in rads/s

Chapter 4 : "Non-Destructive Bridge Deck Condition Assessment with Deterioration Thresholds"

Tao Zou, Cristopher D. Moen

[Published in the proceedings of the 93rd Transportation Research Board Annual Meeting]

Abstract

This paper presents a general procedure to evaluate different types of non-destructive evaluation (NDE) data together by using a deterioration threshold. The deterioration threshold is an NDE magnitude that demarcates healthy and deteriorated areas on a bridge deck, and it is commonly defined empirically by considering bridge deck conditions. A general probability based definition is introduced to calculate the deterioration threshold of a general set of NDE measurement data with specified level of confidence. NDE data can then be mapped to binary coordinates, i.e., '0' for healthy and '1' for deteriorated, by deterioration thresholds, which brings different NDE data sets into common representation for direct comparisons. This binary system accommodates combination of multiple NDE measurements to evaluate bridge deck condition, which can be used to identify current and potential future damage, as well as assisting in determination of deck replacement when compared with DOT criteria. Application of this procedure is demonstrated by analyzing chain drag and GPR data measured on a Virginia Pilot Bridge. The binary mapped NDE data is compared with drilled core samples to evaluate deterioration identification accuracy. Chain drag and GPR data predicted different areas of probable deterioration, and it is demonstrated that when overlay data from the two NDE techniques that a more accurate picture of current and future deterioration is achieved.

4.1 Introduction

Non-destructive evaluation (NDE) methods are being broadly applied by DOTs to quantify concrete bridge deck deterioration. These evaluation techniques produce data that can guide rehabilitation decisions; when carefully evaluated and compared, the NDE data has the potential to reveal direct links between durability and initial design criteria, e.g., concrete mix design and steel girder spacing. Challenges exist though with data interpretation, and it is often difficult to make direct comparisons between different types of NDE data with different underlying physics – e.g., ground penetrating radar (GPR), impact echo, and half-cell potential. This paper introduces a general procedure for evaluating different types of NDE data together, on a common playing field.

Historically NDE techniques have been as simple as dragging metal chains across a bridge deck's surface (i.e., chain drag), which uses changes in sound to identify areas where the bridge deck has delaminated near the top surface (Maierhofer et al. 2010). Advanced tools are becoming more accessible that can, for example, measure the reflected electromagnetic signals to identify deteriorations at the top layer of reinforcing steel within concrete across a bridge deck. Previous research studied the effectiveness of NDE techniques for detecting bridge deck deteriorations, mainly concrete delamination and reinforcing steel corrosion (Gucunski et al. 2010). These studies demonstrated that no single technology (e.g., ground penetrating radar, chain drag, impact echo, half-cell potential) is capable of detecting all deterioration.

It is hypothesized herein that the key to exploring different NDE data types together is the use of a deterioration threshold, defined as the transition within the range of quantitative NDE data from healthy to deteriorated areas on a bridge deck (Zou and Moen 2014). Deterioration thresholds have been established for many NDE techniques, including half-cell potential and

resistivity. For example, -200 mV and -350 mV potentials demarcate high probability and low probability of reinforcing steel corrosion, respectively, in the interpretation of half-cell potential data. Deterioration thresholds for GPR data are typically determined empirically because variability in concrete material properties and bridge deck conditions influences the GPR readings (Ulaby 2010).

A deterioration threshold definition is presented in this paper that accounts for the inherent variability in NDE measurement methods. With this threshold, the NDE data is mapped to a binary system (0 for healthy and 1 for deteriorated) where the level of accuracy (i.e., probability that a deteriorated location predicted by the NDE method is actually deteriorated) is defined by the end user. The binary system accommodates comparison of one NDE technique to another and the combination of multiple NDE measurements to evaluate bridge deck condition. The procedure is illustrated on a Virginia Pilot Bridge within the FHWA Long-Term Bridge Performance (LTBP) Project. The binary mapping is used to directly compare chain drag and GPR Pilot Bridge data, and to demonstrate how the "old school" and "new school" methods can be used together in a rational, scientific framework to perform bridge deck condition assessment. The probability-based deterioration threshold definition is introduced in the following section.

4.2 Probability-based NDE Deterioration Threshold Definition

Suppose a general set of NDE measurements on a bridge deck {XDECK} is collected, with the distribution (histogram) shown in Figure 4-1. The end user (DOT, engineer) would like to know, with a certain confidence level, which locations on the deck are healthy (*H*), i.e., $\{H \subset X_{DECK}\}$ and which locations on the deck are deteriorated (*D*), i.e., $\{D \subset X_{DECK}\}$. The NDE magnitudes $\{H\}$ and $\{D\}$ are defined by thresholds T_H and T_D, where $\{H\} = \{X_{DECK} > T_H\}$ and

$\{D\} = \{X_{DECK} < T_D\}$ (This formulation assumes that low NDE magnitudes reflect deterioration and high values reflect healthy areas. A 'high to low' NDE scale can be included in this approach by switching the signs if necessary). The thresholds T_H and T_D are selected to provide, at a specific probability or level of confidence, that the points identified in $\{H\}$ or $\{D\}$ are actually healthy or deteriorated, respectively.

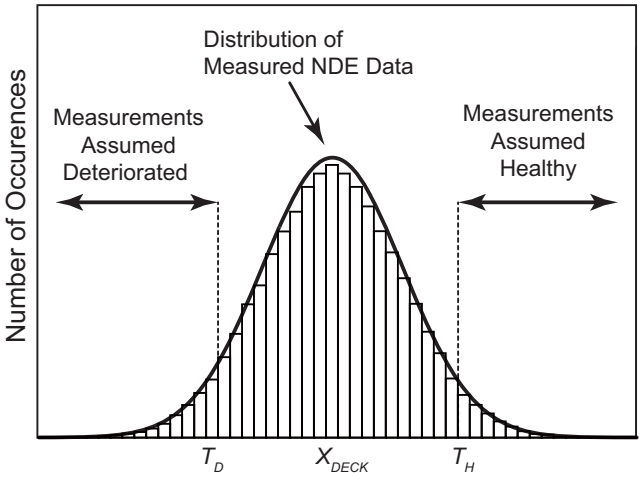

Figure 4-1 A typical distribution of measured NDE data and thresholds

The conditional probability that an NDE measurement magnitude on a specific bridge deck less than T_D is actually deteriorated is $P(Deteriorated \mid X_{DECK}<T_D) = 1- P(Healthy \mid X_{DECK}<T_D) = 1 - p$, where $p = P(Healthy \mid X_{DECK}<T_D)$. In the same sense, the probability that an NDE measurement magnitude on a bridge deck greater than T_H is actually healthy is $P(Healthy \mid X_{DECK}>T_H) = 1 - q$, where $q = P(Deteriorated \mid X_{DECK}>T_H)$. The end user selects the accuracy or confidence they want when identifying healthy and deteriorated locations with the NDE data by defining $P(Deteriorated \mid X_{DECK}<T_D)$ and $P(Healthy \mid X_{DECK}>T_H)$, for example both can be set to 0.90. This means that there is a 90% chance that any bridge deck location within the set $\{D\}$ is

actually deteriorated, and there is a 90% chance that any bridge deck location within the set $\{H\}$ is healthy.

The NDE magnitude of healthy concrete, referred to as $\{X_{NDE}\}$, varies based on the NDE types (ground penetrating radar, impact echo, half-cell potential and resistivity) and concrete properties; it can be calculated theoretically based on properties of the bridge decks being measured. For example, theoretical GPR magnitude is a function of concrete relative permittivity, magnetic permeability and electrical conductivity, as well as temperature and antenna frequency. Since theoretical NDE magnitude is derived from properties of actual bridges, it serves as a link between the actual bridge deck and a corresponding bridge deck with all healthy concrete. Therefore, the confidence levels, $P(Deteriorated \mid X_{DECK}<T_D)$ and $P(Healthy \mid X_{DECK}>T_H)$, are assumed equivalent to $P(Deteriorated \mid X_{NDE}<T_D)$ and $P(Healthy \mid X_{NDE}>T_H)$, respectively.

With $P(Deteriorated \mid X_{DECK}<T_D)$ and $P(Healthy \mid X_{DECK}>T_H)$ specified, T_D and T_H are calculated to achieve these probabilities using the NDE measurement method probability density function shown schematically in Figure 4-2, in which the pdf represents the variability of theoretical NDE magnitudes for healthy concrete. For the example that $P(Deteriorated \mid X_{DECK}<\mathrm{T_D}) = 1 - p = 0.90$ and $P(Healthy \mid X_{DECK}>\mathrm{T_H}) = 1- q = 0.90$, then $P(Healthy \mid X_{DECK}<T_D) = p = 0.10$ and $P(Healthy \mid X_{DECK}>T_H)= 1- q$ remains as 0.90. Assuming the NDE measurements for a specific NDE type vary as a Gaussian distribution with mean μ_{NDE} and standard deviation σ_{NDE} (this assumption is supported by research conducted by the authors on GPR measurement variability on healthy concrete, (Zou and Moen 2014)), T_D and T_H can be calculated directly from the standard normal distribution (Figure 4-2) for a NDE type as

$$T_D = \mu_{NDE} - z(p)\sigma_{NDE} \tag{4-1}$$

and

$$T_H = \mu_{NDE} + z(1-q)\sigma_{NDE} \tag{4-2}$$

where $z(p)$ and $z(1-q)$ can be easily obtained from a z-table in a statistics book (Weiss 2012).

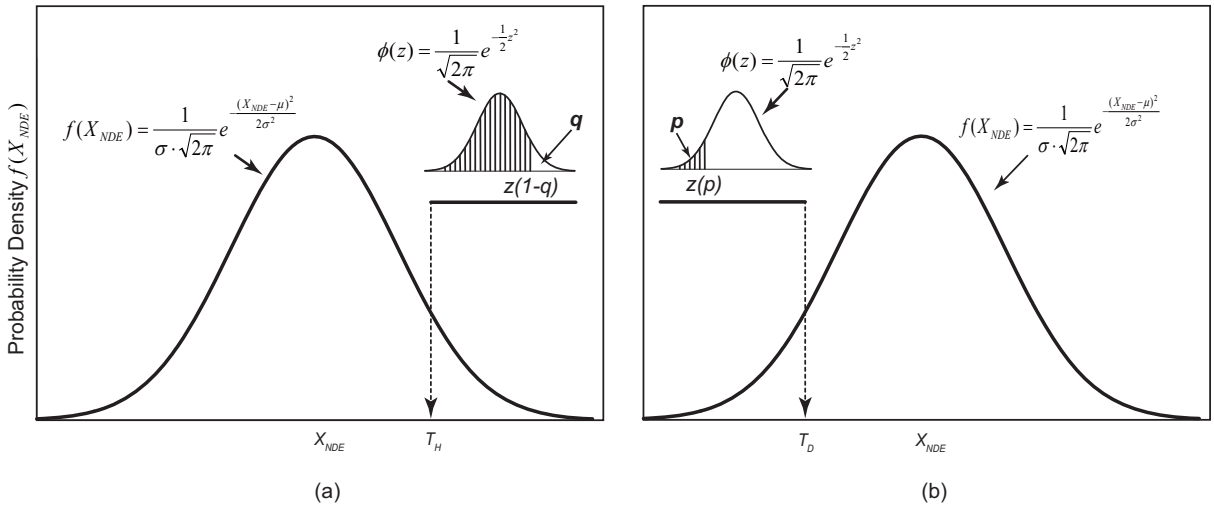

Figure 4-2 Theoretical distributions of NDE data for healthy concrete with (a) T_H and (b) T_D

4.3 GPR Deterioration Threshold Definition

The threshold definitions in the previous section are used to define T_D for GPR data measured on a Virginia bridge selected for the Federal Highway Administration's Long Term Bridge Performance Project. The GPR deterioration threshold is typically defined subjectively by the operator conducting the NDE measurements considering the age of bridge deck, visual deck condition, and the intensity of NDE signal change (Gucunski et al. 2005), or by varying a data normalization parameter from GPR technique to obtain the best graphical correlation with another NDE mapping (Rhazi et al. 2005*)*. These thresholds are typically established from project-specific data and are not appropriate for general application (Guthrie and Tuttle 2006).

Ground penetrating radar is an electromagnetic (EM) method based on the propagation and reflection of EM waves. A short pulse of electromagnetic energy is transmitted into the slab,

which is then reflected from objects or interfaces representing discontinuities in electrical properties, e.g., top and bottom rebar grids and abrupt variations in concrete properties in bridge decks (Maser 1989); the reflected signal is then picked up by a receiving antenna. The strength of reflected signal depends on the reflection, transmission and attenuation characteristics of the medium, and the signal attenuation, or loss of EM energy, is a common representation of bridge deck condition by GPR measurement, which is also used to assess the deck condition of Virginia Pilot Bridge.

The electromagnetic signal that is detected by the receiver undergoes loss in its propagation path from the transmitter to the receiver, and material loss and scattering loss are large portions of the total loss. Material loss is related to the electrical and magnetic properties of the medium, and is referred to as the standard signal attenuation for healthy concrete. In addition to the signal attenuation due to the signal conduction process, the inhomogeneities in the medium can also cause scattering loss. The scattering losses are typically small in healthy concrete, since the size of aggregate particle is much smaller than the electromagnetic wavelength (Halabe et al. 1989). However, when large dimension inhomogeneities are present in concrete, e.g., delaminations, the scattering loss cannot be neglected, resulting to higher degree of signal attenuation than healthy concrete.

To calculate the deterioration threshold, T_D, $P(Deteriorated \mid X_{DECK}<T_D) = 1- p$ is set by the operator or end users and then $P(Healthy \mid X_{DECK}<T_D) = p$ is calculated based on the GPR measurement data for a healthy bridge. $P(Healthy \mid X_{DECK}<T_D)$ is obtained from the probability density function for signal attenuation of healthy concrete. Theoretical signal attenuation of healthy concrete is related to concrete properties and environmental conditions, for details see (Zou and Moen 2014). All attenuation parameters were measured on the Virginia Pilot Bridge

deck (except for moisture content which was assumed constant at 4.8%) with statistics reported in Table 4-1.

Table 4-1 GPR signal attenuation statistics for the Virginia Pilot Bridge

Property	Mean	Std Dev
Porosity (ϕ) (%)	14.7	0.01
Chloride Concentration (lbs/yd^3)	8.6	3.1
Pore Water Salinity (S_{sw}) (ppt)	99.1	34.7
Saturation (S) (%)	69.1	0.1
Concrete Surface Conductivity (σ_c) (S/m)	$2.5\text{x}10^{-3}$	$2.5\text{x}10^{-3}$
Clear Concrete Cover Depth (d) (m)	$5.7\text{x}10^{-2}$	$6.9\text{x}10^{-3}$

Using the methods outlined in (Zou and Moen 2014) and the measured variables in Table 4-1, the GPR attenuation probability density function statistics for a healthy bridge deck are μ_A=-13.92 dB and σ_A=5.05 dB, resulting in

$$A = f(X_{GPR}) = -\frac{1}{5.05 \cdot \sqrt{2\pi}} e^{-\frac{(X_{GPR}+13.92)^2}{2\times 5.05^2}} \tag{4-3}$$

The deterioration threshold T_D is calculated by finding z(p) from the standard normal distribution of Eq. (4-3) for varying levels $P(Deteriorated \mid X_{DECK}<T_D)$, i.e, for varying confidence levels that the bridge deck locations identified as deteriorated are actually deteriorated, and then plugging in $z(p)$ into Eq. (4-1) to get T_D as shown in Table 4-2.

Table 4-2 Deterioration Thresholds for the Virginia Pilot Bridge

Confidence	*1-p*	z(p)	T_D (dB)
95%	0.95	-1.64	-22
90%	0.90	-1.28	-20
80%	0.80	-0.85	-18
70%	0.70	-0.50	-16

The theoretical GPR signal attenuation with various confidence levels is shown in Figure 4-3, together with the histogram of actual measured signal attenuation on the Virginia Pilot Bridge.

At 30% significance level (70% confidence level), the signal attenuation equals to -16 dB, which is same as the value determined empirically. In other words, when -16 dB is used as the GPR deterioration threshold, there is a 70% probability that identified areas (areas with measured signal attenuation more negative than -16 dB) are truly deteriorated. Furthermore, when -22 dB is used as the deterioration threshold, the probability that identified areas are truly deteriorated is 95%. Considering that no 'ground truth' actually exists for any NDE measurement, the determination of deteriorations on bridge decks based on this probabilistic approach gives bridge owners and inspectors a rational, scientific-based method for identifying deteriorated areas with specified confidence. Now that the deterioration thresholds are defined for the Virginia Pilot Bridge, an example of how this threshold can be used – specifically with a comparison of chain drag to GPR and then a proposed method demonstrating how GPR and chain drag could be used together to conduct a bridge deck assessment.

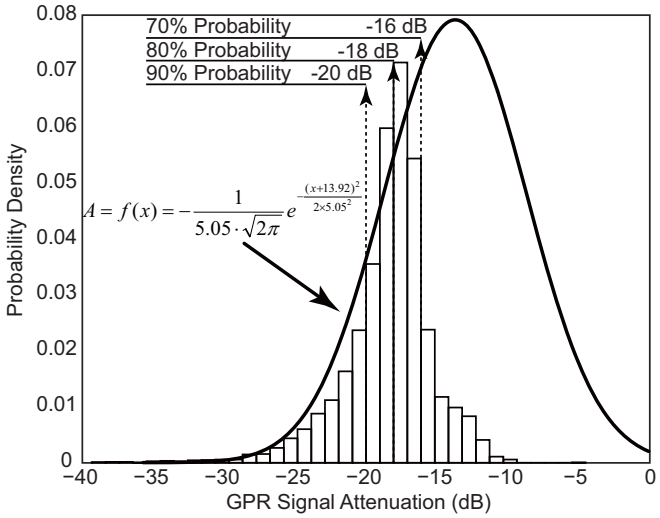

Figure 4-3 Distribution of Theoretical GPR Deterioration Threshold

4.4 Virginia Bridge Chain Drag and GPR Measurements

The southbound bridge on U.S. Route 15 over Interstate 66 in Haymarket, VA is evaluated in this comparison study of chain drag and GPR bridge deck condition measurements. It was the first pilot bridge in Long Term Bridge Performance (LTBP) Program with common steel stringer girders and a poor deck condition. This bridge was built in 1979, has a total length of 83.5m (274 ft.) and two lanes travelling southbound (Collins 2010) as shown in Figure 4-4. Two 41.8m (137 ft.) spans cross over two lanes of east and westbound Interstate. The bridge deck is supported by six continuous steel girders with varying cross section and 2.3m (7ft-6in) center to center spacing. Bridge deck thickness is 0.02m (8-1/2 in.) with an approximate skew of 17.45°. Steel girders are supported on abutments with rocker bearing and on piers with pin bearings.

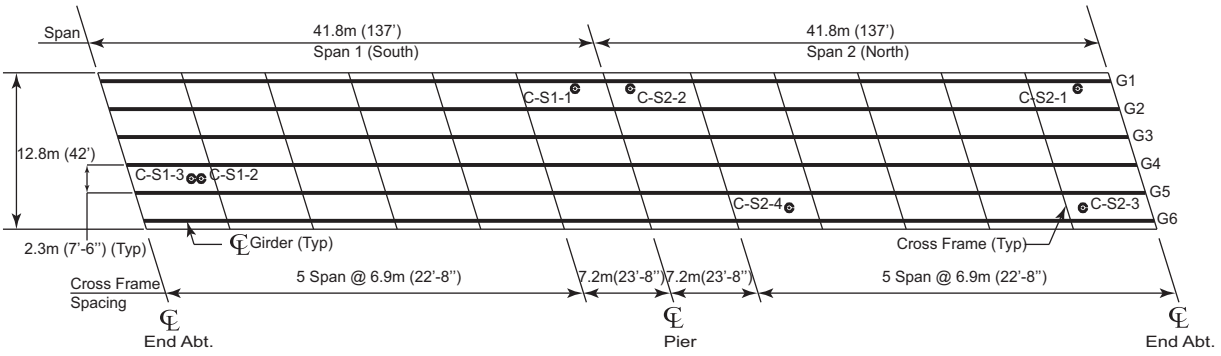

(a)

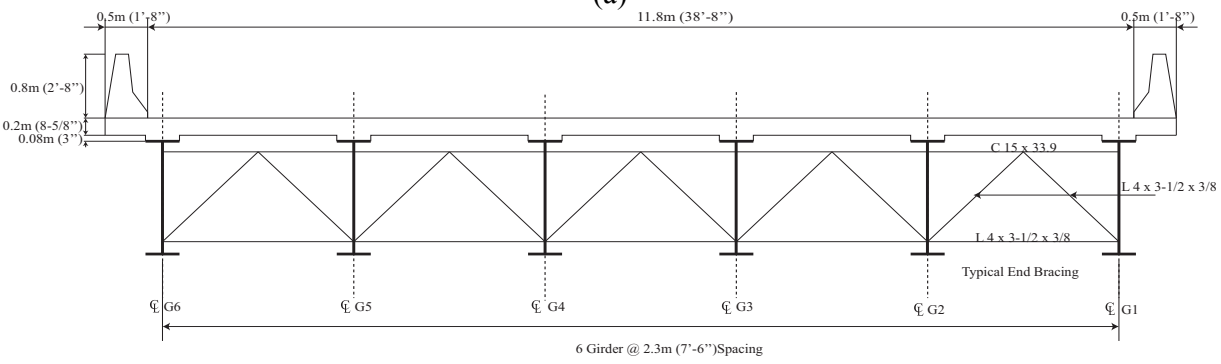

(b)

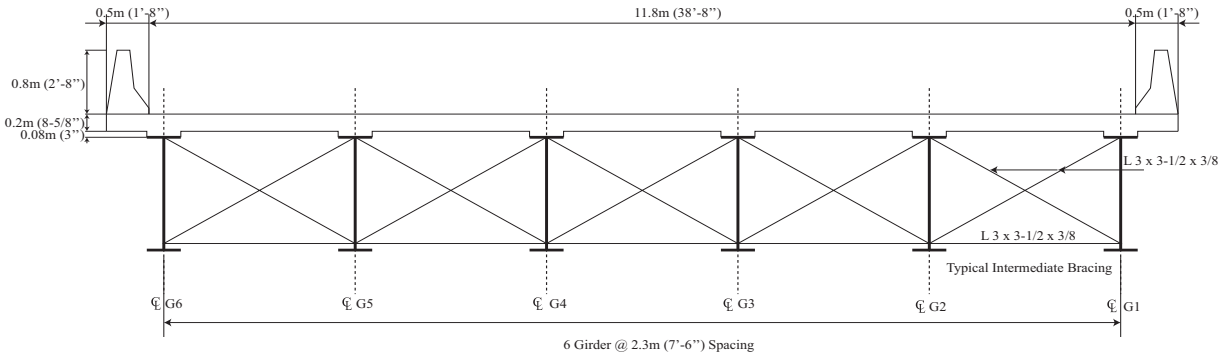

(c)

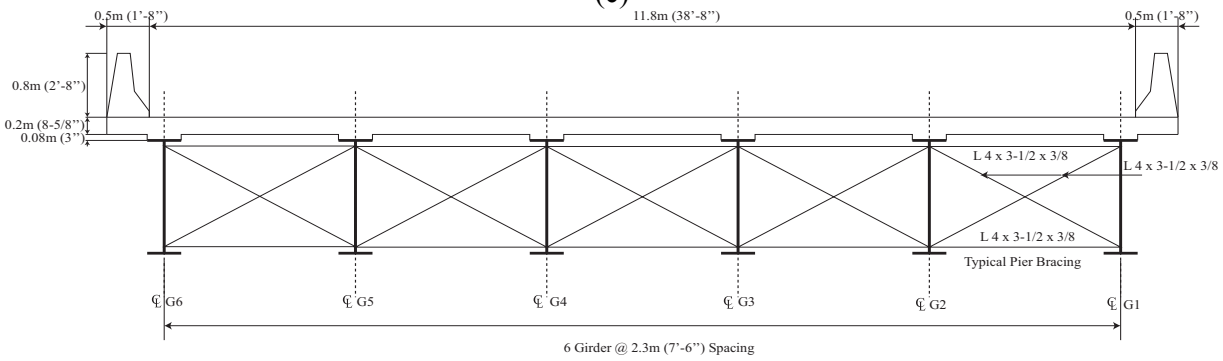

(d)

Figure 4-4 Virginia Route 15 Bridge (a) layout, (b) typical end section, (c) typical intermediate section and (d) pier section

4.4.1 Chain Drag Measurement on Virginia Pilot Bridge

To detect defects in this bridge deck, several NDE measurements were conducted, including chain drag and GPR. Chain drag is an acoustic method that is based on change of sounds while a set of chain links are dragged on bridge deck surface (ASTM D4580-03 2012). It is a rapid and inexpensive way to locate near surface delamination and severe stages of bridge deck deterioration; however, the accuracy of chain drag measurement depends on inspector technique and experience (Hernderson et al. 1999). Bridge deck condition evaluated by the chain drag method is shown in Figure 4-5, with deteriorated areas indicated. As mentioned, unlike other NDE methods representing NDE results by quantitative data, chain drag only gives binary results, indicating whether cracking or delamination is present at testing locations (1) or not (0).

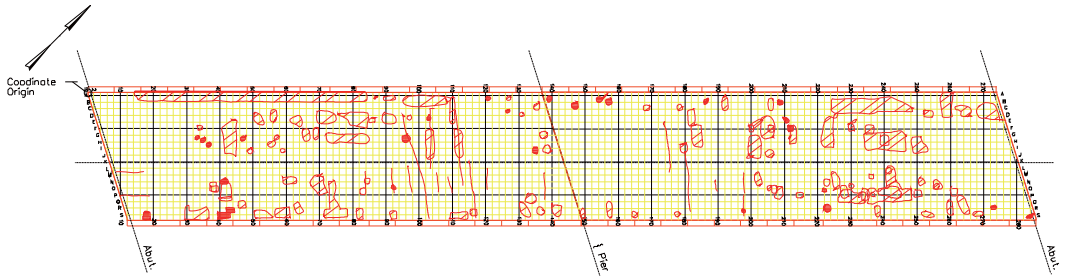

Figure 4-5 Virginia Route 15 Bridge condition evaluated by chain drag (Andrew Foden 2009)

In addition to chain drag readings, core samples were drilled at seven locations identified in Figure 4-4(a), and four out of the seven locations have delamination as shown in Figure 4-6. This core data will be used later in the paper to provide a comparison to the NDE methods.

Core	Top	Diameter	Side	Depth	Condition	Note
C-S1-1	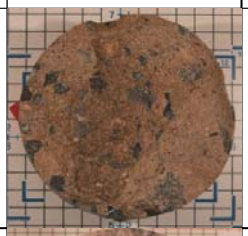	10.16 cm (4.00 in.)	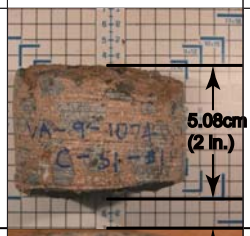	5.08 cm (2.00 in.)	Delamination	na
C-S1-2	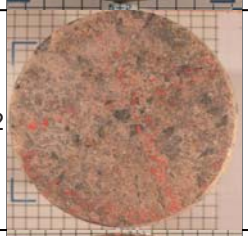	10.16 cm (4.00 in.)	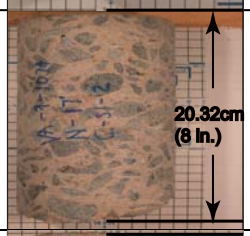	20.32 cm (8.00 in.)	No Delamination	na
C-S1-3	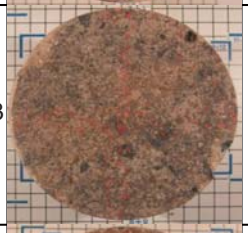	10.16 cm (4.00 in.)	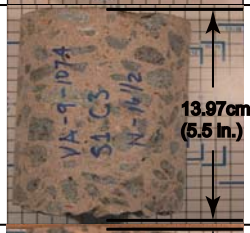	13.97 cm (5.50 in.)	Delamination	No Near Surface Delamination
C-S2-1	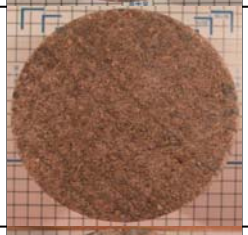	10.16 cm (4.00 in.)	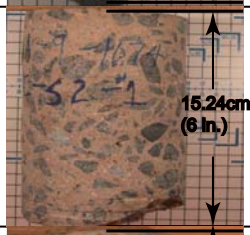	15.24 cm (6.00 in.)	Delamination	No Near Surface Delamination
C-S2-2	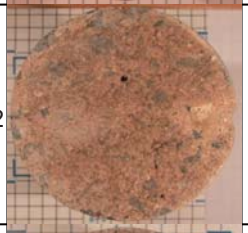	10.16 cm (4.00 in.)	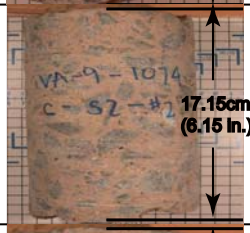	17.15 cm (6.75 in.)	No Delamination	na
C-S2-3	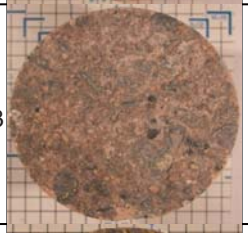	10.16 cm (4.00 in.)	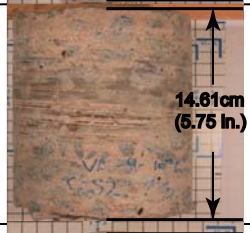	14.61 cm (5.75 in.)	No Delamination	na
C-S2-4	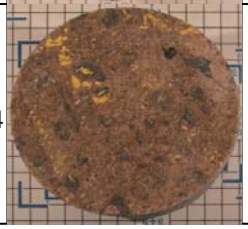	10.16 cm (4.00 in.)	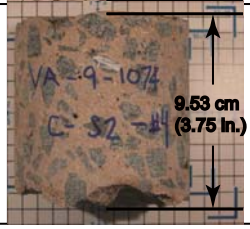	9.53 cm (3.75 in.)	Delamination	na

Figure 4-6 Depths and conditions of core samples (Rutgers University 2009)

4.4.2 Ground Penetrating Radar Measurement on Virginia Pilot Bridge

In Figure 4-7, condition mapping of the Virginia Pilot Bridge is shown as GPR measurements expressed with signal attenuation contours. Deterioration threshold in Figure 4-7 was identified as -16 dB by the researchers who performed the measurements (Romero et al. 2010*)*).This threshold value was determined empirically considering the age of bridge deck, visual deck condition, and the intensity of NDE signal change. As shown previously in Table 4-2, this empirical deterioration threshold results in a 70% probability that locations with measure signal attenuation less than -16 dB are truly deteriorated.

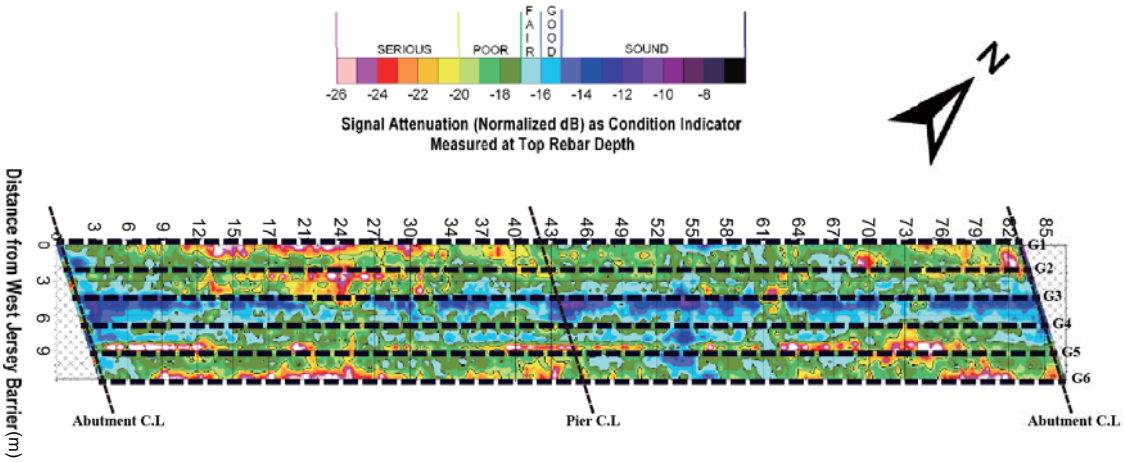

Figure 4-7 Virginia Route 15 Bridge condition evaluated by GPR (Rutgers University 2009)

4.5 Chain Drag and GPR Data Trends

A question that is often asked by bridge owners is how accurate is GPR compared to chain drag, and what differences are there in a GPR versus a chain drag mapping. These questions are evaluated in the following sections, based on a GPR deterioration threshold, T_D=-18 dB.

4.5.1 NDE Binary Mapping Methods

To evaluate chain drag and GPR data accuracy and facilitate comparisons later in the paper, it is necessary to transform all data into the same coordinate system. For the chain drag mapping, coordinates at measuring locations are defined and the existence of delaminations is identified as black dots (magnitude of '1') in Figure 4-8 with the original detected areas with delamination shown as outlines. Healthy areas are represented numerically as '0'.

The GPR data is mapped to binary types with '1' for 'deteriorated' or '0' for 'healthy' using the deterioration threshold of -18 dB (Oh et al. 2012). Locations with measured signal attenuation less than (more negative) -18 dB are identified as deteriorated, and vice versa. Furthermore, these data are linearly interpolated onto the same planar coordinate system with 0.6-m (2-ft) grids coincident with onsite measurement of chain drag, thus bridge deck condition could be represented by discrete points on this coordinate system to conduct point-to-point comparisons.

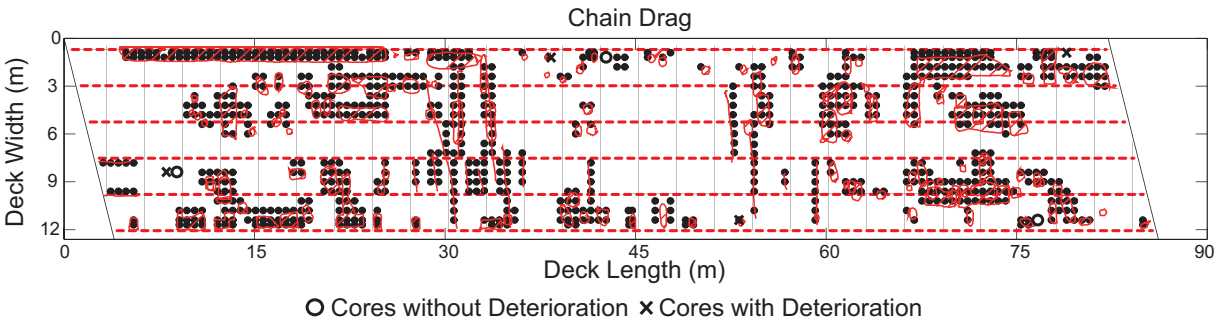

Figure 4-8 Chain drag results with discretized deterioration points overlaid – 'O' for cores without delamination and 'X' for cores with delamination

4.5.2 Chain Drag and GPR Deterioration Prediction Accuracy

Based on the delaminated areas shown in Figure 4-8, the chain drag predicts that 29 percent of the bridge deck area is deteriorated. But how accurate is this approximation? The delaminated area predictions are compared to the drilled core data in Figure 4-8; the circles (O) representing

cores without delamination and crosses (X) representing cores with delamination. All three cores without delamination are correctly identified, while two out of four cores with delaminations were incorrectly identified as in healthy condition, resulting in a prediction accuracy of 5/7 or 71%. At these two incorrectly identified locations, which are C-S1-3 and C-S2-1, there were no signs of top surface cracking or near surface delamination as shown in Figure 4-6, although delamination was present at the top layer of reinforcing steel in the bridge deck. As mentioned previously, accuracy of chain drag measurement depends on the operation and experience of operators and is able to provide accurate predictions of damage, especially for locations with surface cracking or near surface delamination. However, for delaminated locations without signs of near surface cracking or delamination, chain drag tends to be unable to identify deterioration.

GPR data is plotted in Figure 4-9 with 47 percent of the bridge area predicted as deteriorated. This is higher than the chain drag predictions (29 percent) because at least in part, the GPR has a higher fidelity data collection and can 'see' damage that may not be picked up by the chain drag technique, especially deteriorations deep in a bridge deck. On the other hand, GPR is also well known for having attenuation loss from several sources e.g., antenna loss, transmission loss and spreading loss, that is complicated to predict which may be contributing to the differences when compared to chain drag.

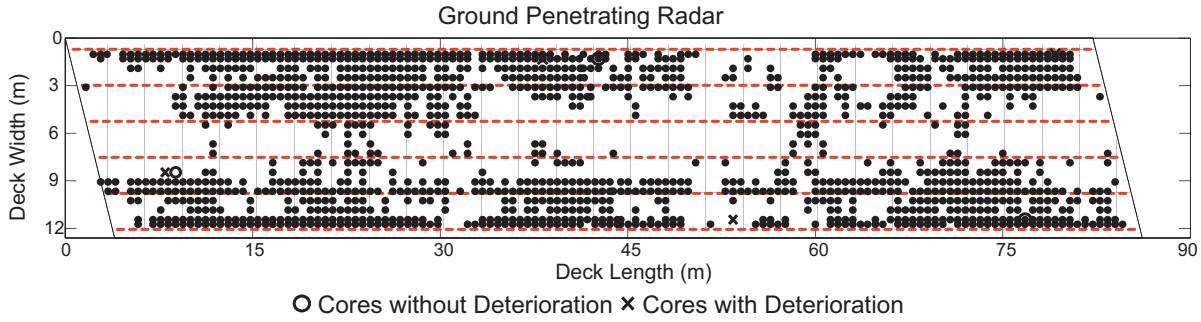

Figure 4-9 Deteriorations measured by GPR with core samples

Comparing the core results to the GPR deterioration predictions, 3/7 or 43 percent of bridge deck is identified as deteriorated which is lower than the chain drag approach. For three locations without delamination identified by cores, GPR is able to only pick up one correctly, and other two locations (C-S2-2 and C-S2-3) are incorrectly identified as having delaminations. For the four locations indicating delamination by cores, GPR incorrectly identified two as not deteriorated (C-S1-3 and C-S2-4), although these two cores were located at the boundary between healthy and deteriorated locations, which makes interpretation of results challenging. Overall it is clear that chain drag matches the core results better, which doesn't necessarily mean that GPR is less accurate at predicting bridge deck deterioration due to limited number of core data, but does suggest that GPR results could be more valuable when combined with other NDE techniques in conducting bridge deck condition assessment. A suggested combination method is proposed in the next section.

4.6 Using GPR and Chain Drag Together for Bridge Deck Assessment

Although GPR has a lower overall accuracy (43%) through comparison with core samples, it is able to identify most locations with delamination at top layer of reinforcing steel, as well as surface cracking or near surface delamination, which may result in potentially severe delamination in the future. Meanwhile, with a higher overall accuracy than GPR (71%), chain

drag identifies all locations without existing delamination. These trends demonstrate that an option for improving condition assessment is to consider chain drag and GPR measurements together, and this overlapped approach is made possible with the mapping approach introduced earlier in the paper.

Chain drag and GPR data are presented together in Figure 4-10 for the Virginia Pilot Bridge. Assessment accuracy improves over either NDE measurement by itself, with now 6/7 core conditions predicted accurately (86 percent). Through comparison with cores, three out of four deteriorated locations are identified as delaminated by either chain drag or GPR or both two NDE measurements (Table 4-3), while now the three locations without delaminations are all identified correctly.

Black dots in Figure 4-10 indicate bridge deck locations identified as deteriorated by both two measurements, while gray dots are points identified as deteriorated by either chain drag or GPR. Areas identified as deteriorated by both two measurements are 20 percent and by either measurement are 56 percent. This data representation could be viewed as showing current damage (black dots) and predicted future damage (grey dots), which could be useful for bridge owners attempting to determine when to replace a bridge deck. An extension of this approach is to compare these 'current+future' mappings on a standard inspection cycle (every 2 years for example). For many DOTs, bridge deck deterioration area exceeding 30 to 50 percent of deck area warranted consideration of deck replacement (Hema et al. 2004). By overlapping, percent of deteriorated areas identified by multiple NDE measurements could be compared with the above criteria, supporting bridge deck replacement decisions.

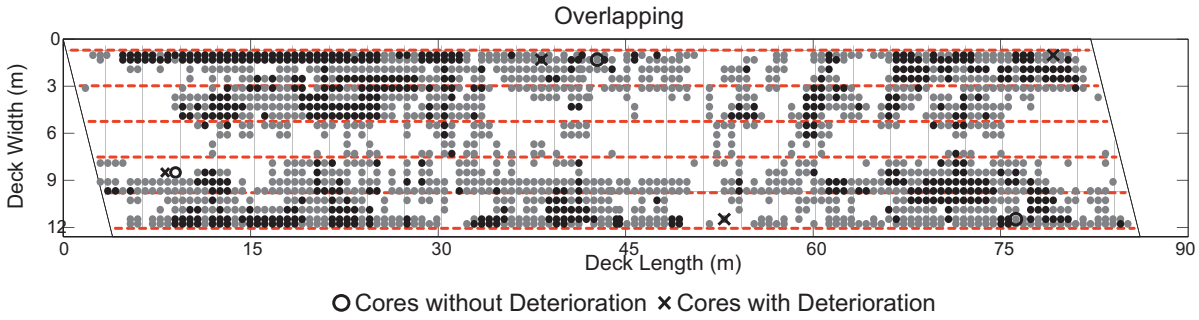

Figure 4-10 Overlapping of deteriorated points by chain drag and GPR

Table 4-3 Chain Drag and GPR Measurement Compared with Cores

Core	Core Condition	Chain Drag	GPR	Overlapping
C-S1-1	Delamination	Correct	Correct	Both Correct
C-S1-2	No Delamination	Correct	Correct	Both Correct
C-S1-3	Delamination	Incorrect	Incorrect	Neither Correct
C-S2-1	Delamination	Incorrect	Correct	Either Correct
C-S2-2	No Delamination	Correct	Incorrect	Either Correct
C-S2-3	No Delamination	Correct	Incorrect	Either Correct
C-S2-4	Delamination	Correct	Incorrect	Either Correct

4.7 Conclusion

NDE techniques commonly measure different underlying physics for certain deterioration types, making direct comparisons between NDE data and combined assessment of bridge deck condition difficult. This paper first presents a rational, scientific-based method for calculating the deterioration threshold of a general set of NDE measurement data. The threshold is used to convert NDE data into a common coordinate system with a binary representation. Accuracy of chain drag and GPR measurements is evaluated through comparison with drilled core data. Chain drag delamination predictions match cored bridge deck trends better than GPR, and it is demonstrated that bridge deck assessment accuracy can be improved by using chain drag and GPR results together. This combination provides both current and projected future deterioration which could be helpful for bridge owners making bridge deck replacement decisions. Moreover, by applying the probability-based deterioration threshold, the deterioration projects can be

conducted at varying confidence levels. The binary mapping technique is also applicable to impact echo, half-cell potential, resistivity, providing the possibility of bringing multiple NDE techniques onto the same playing field for bridge deck assessment, a research topic currently being studied by the authors.

Acknowledgement

This publication was supported by a subcontract from Rutgers University, Center for Advanced Infrastructure & Transportation (CAIT), under DTFH61-08-C-00005 from the U.S. Department of Transportation – Federal Highway Administration (USDOT-FHWA).

Chapter 5 : "Correlation between Live Load and Shrinkage Stresses and Bridge Deck Deterioration with Non-Destructive Evaluation"

Tao Zou, Cristopher D. Moen

[To be submitted to Journal of Bridge Engineering]

Abstract: This paper presents a method to study the correlation between live load and shrinkage induced stresses on the bridge deck and deteriorations measured by non-destructive evaluations (NDE), i.e., chain drag, ground penetrating radar (GPR) and half-cell potential. Stress distributions on the bridge deck surface are studied using a validated finite element model. Three live loading scenarios are studied with different combinations of truck locations, and concrete shrinkage is modeled by the uniform temperature change. Correlations are evaluated using two methodologies: (1) Pearson correlation coefficients are evaluated by interpolating stresses through finite element analysis to NDE testing locations, and (2) stresses and NDE data are normalized to a binary format (healthy or deteriorated) by threshold values, e.g., the concrete rupture strength for stresses and deterioration thresholds for quantitative NDE data. Correlations are then studied by evaluating number of points identified as deteriorated by both stresses and NDE data. The finite element analysis and correlation study are presented on a Virginia Pilot Bridge in Federal Highway Administration's Long Term Bridge Performance Project, and the correlation study is finally used to identify causes on bridge deck deteriorations.

Author keywords: Bridge deck, Finite Element, Stress, Live Load, Shrinkage, NDE, Correlation

5.1 Introduction

Concrete bridge deck deteriorations have been the main issue that reduces the service life of bridge structures. These deteriorations commonly initiate with the diffusion of chloride ions

through pores or surface cracks, which induce corrosion when in contact with rebar, further causing spalling and delamination of concrete (Breysse 2010). A study on the relation between time and corrosion induced deteriorations on bridge decks indicated that deterioration rate increases by 40% to 50% after diffusion of chloride ions and corrosion of rebar (Cady and Weyers 1984). Understanding causes of concrete deteriorations can help in modeling future degradation, when combined with measured existing deteriorations, can also lead to potential improvement on bridge decks' service life.

Non-destructive evaluation (NDE) has been applied for decades in detecting existing deteriorations on bridge decks, from judgment based on change of sound when dragging metal chains on the bridge deck surface, e.g., chain drag, to more advanced techniques measuring different underlying physics (Maierhofer et al. 2010). When carefully evaluated, NDE data provides rich and in-depth understanding on bridge deck deteriorations. Deterioration thresholds define the probable transitions between healthy and deteriorated areas, and can help in the interpretation of measured NDE data (Gucunski et al. 2013). A probability-based methodology was proposed to determine the deterioration thresholds of quantitative NDE data by the author (Zou and Moen 2014). This methodology transforms the continuous NDE data into a binary format, and allows direct comparisons among NDE techniques measuring different physics (Zou and Moen 2014). However, NDE techniques are only capable of detecting existing deteriorations. Finite element analysis is a powerful tool that simulates behaviors of bridge structures (Lee 2010). Studies of correlations between finite element results and NDE deteriorations help understand the causes of bridge deterioration. This correlation study can also be used to predict potential future concrete deteriorations.

Researchers have discussed the accuracy and application of finite element models in analyzing behavior of composite bridge structures, as well as the modeling of deterioration process. Two simple-span and one continuous span bridge models were built using the commercial finite element package ABAQUS to study the ultimate load behavior of composite bridge decks (Barth and Wu 2006), and the accuracy of modeling steel girders and concrete slabs by shell elements was validated through comparing finite element results with experimental data. Biggs et al. (2010) also studied the behavior of reinforced concrete decks by introducing nonlinear concrete material model with tension stiffening, which was capable of capturing the pre- and post-cracking behaviors of concrete decks, and simulation results fundamentally agreed with theoretical and experimental values.

In addition to finite element modeling of bridge behaviors, research was conducted on the utilization of nonlinear finite element and statistical method to predict deteriorations. Lee (2011) conducted finite element parametric studies on concrete blocks with rebar embedded, and corrosion was modeled by the expansion of reinforcing steel using fictitious temperature increases. Although a reliability-based predictive model was proposed with a reasonable consistent with National Bridge Inventory records, this research was focused on the component level, which did not include the system behavior of bridge structures. The early cracking of a three-span, continuous, skewed bridge on US 331 in Montgomery County, Alabama was also studied (Schindler et al. 2010). It was concluded that horizontal early cracking was most likely caused by excessive early-age temperature gradients combined with drying shrinkage, which produced large shear and normal stresses at the top reinforcement mat location in concrete with the high coefficient of thermal expansion and modulus of elasticity.

The objective of this paper is to study the correlations between stresses and NDE deteriorations on the concrete deck of a two-span continuous steel girder bridge. The stresses studied in this paper are induced from live loads with different combinations of truck locations, as well as concrete shrinkage. Stresses are interpolated to the NDE measuring grid, for the purpose of direct comparisons. Two methodologies are used to evaluate the correlations, which are Pearson correlation coefficients and correlations by normalizing finite element stresses and measured NDE data.

5.2 Virginia Pilot Bridge Live Load Testing

The southbound bridge on U.S. Route 15 over Interstate 66 in Virginia is evaluated in this study. It was the first pilot bridge in Long Term Bridge Performance (LTBP) Program with common steel stringer girders and a fairly poor deck condition. The bridge deck was categorized as in satisfactory condition according to National Bridge Inventory (NBI 2010). This bridge was built in 1979, with a total length of 83.5m (274 ft.) and two lanes travelling southbound (Collins 2010), crossing over two lanes of east and westbound. The bridge deck is supported by six continuous steel girders with varying cross section and 2.3 m (7ft-6in) center to center spacing. Cross frames are with varying configurations spacing 6.9 m (22ft-8in) at intermediate span and 7.2 m (23ft-8in) at piers (Figure 5-1(a - c)). The bridge deck thickness is 220 mm (8-1/2 in.) with an approximate 17.45° skew. Steel girders are supported with rocker bearings on abutments and pin bearings on piers.

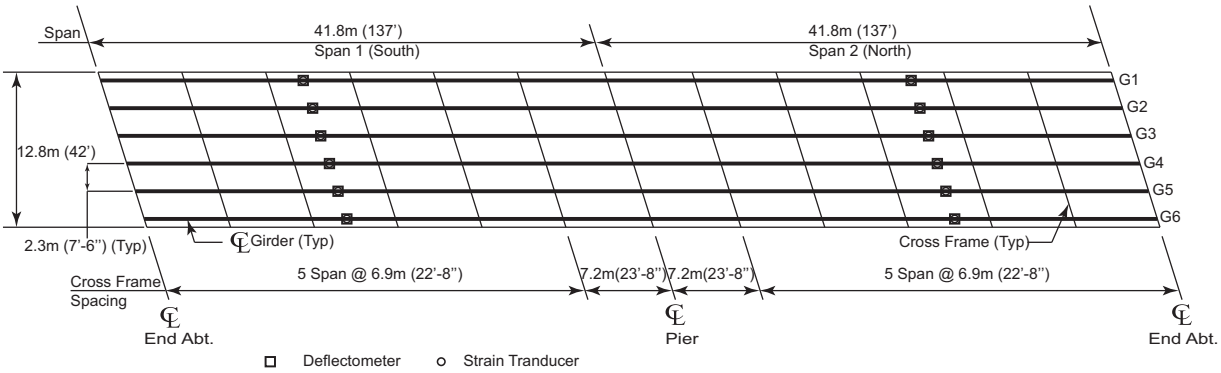
Span
41.8m (137')
Span 1 (South)
41.8m (137')
Span 2 (North)
G1
G2
G3
G4
G5
G6
12.8m (42')
2.3m (7'-6") (Typ)
℄ Girder (Typ)
Cross Frame (Typ)
Cross Frame Spacing
5 Span @ 6.9m (22'-8")
7.2m(23'-8")
7.2m(23'-8")
5 Span @ 6.9m (22'-8")
℄ End Abt.
℄ Pier
℄ End Abt.
Deflectometer
Strain Tranducer

(a)

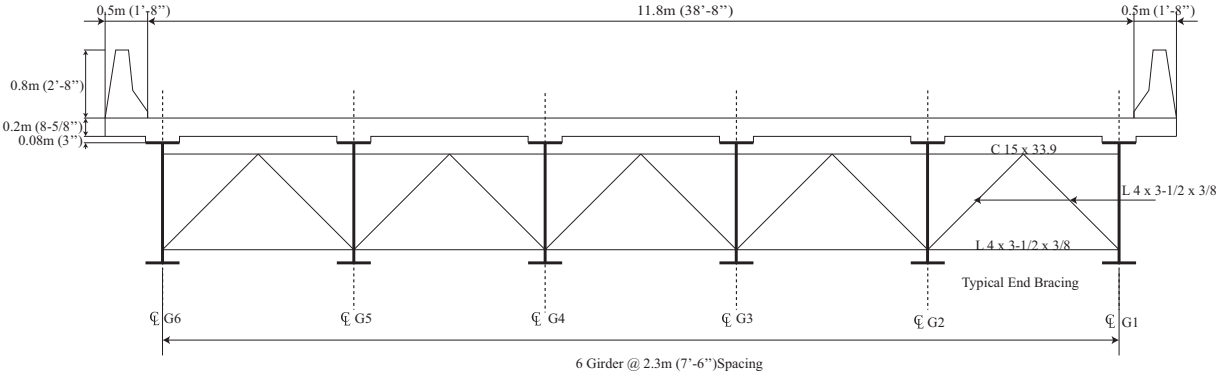
0.5m (1'-8")
11.8m (38'-8")
0.5m (1'-8")
0.8m (2'-8")
0.2m (8-5/8")
0.08m (3")
C 15 x 33.9
L 4 x 3-1/2 x 3/8
L 4 x 3-1/2 x 3/8
Typical End Bracing
℄ G6
℄ G5
℄ G4
℄ G3
℄ G2
℄ G1
6 Girder @ 2.3m (7'-6")Spacing

(b)

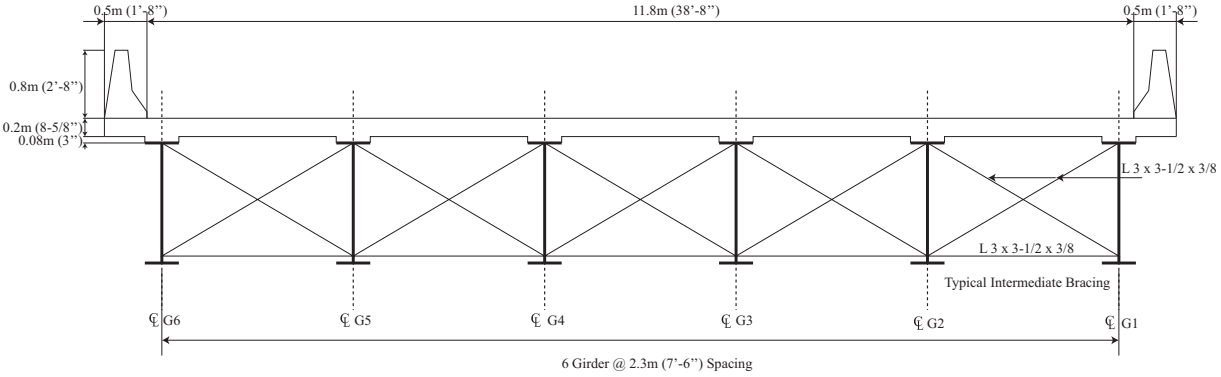
0.5m (1'-8")
11.8m (38'-8")
0.5m (1'-8")
0.8m (2'-8")
0.2m (8-5/8")
0.08m (3")
L 3 x 3-1/2 x 3/8
L 3 x 3-1/2 x 3/8
Typical Intermediate Bracing
℄ G6
℄ G5
℄ G4
℄ G3
℄ G2
℄ G1
6 Girder @ 2.3m (7'-6") Spacing

(c)

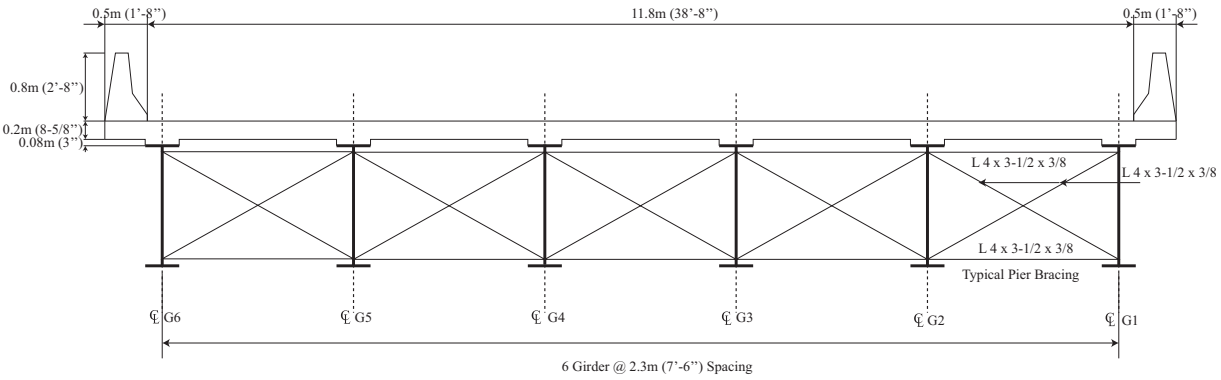

(d)

Figure 5-1 VA Pilot Bridge: (a) layout; (b) typical end section; (c) typical intermediate section and (d) pier section

Live load testing was conducted on this bridge in 2009 by Collins (2010). Strains were measured during live load testing through the use of strain transducers, installed at 0.4L on both north and south span, where L = 41.8 m (137 ft) is the span length. The instrumentation layout is illustrated in Figure 5-1(a). The strain transducers were installed on bottom flanges of six steel girders to measure the maximum strains during live load testing. Deflections were measured using deflectometers, which is composed of an aluminum plate carrying a full strain gage and the plate is sandwiched between two other aluminum plates at its base, and attached to the girder bottom flange (Collins 2010). Deflectometers were installed at 0.4L on both north and south spans as well, with the layout also shown in Figure 5-1(a).

The test vehicle was two Virginia Department of Transportation (VDOT) three-axle dump trucks, with the load of approximately 222 kN (50 kips). The axles of both trucks were weighed individually, with around 68 percent of load distributed to the rear axles, and 32 percent to the front axles. The total load is distributed to each front wheel for about 34 kN (7.7 kips) and to each rear wheel for 37 kN (8.4 kips). The dimensions of loading trucks are shown in Figure 5-2.

Three scenarios (scenarios A, B and C) were designed to maximally load selected girders, and two others (scenarios D and E) with vehicle centered in normal traffic lanes. Scenario A represents the case where girder 1 (G 1) was maximally loaded, where the exterior truck wheel was placed as close as possible to being directly above the girder. Distance from the truck to the guardrail was about 180 mm (7 in.) as demonstrated in Figure 5-2. In scenarios B and C, the bridge was loaded by two trucks simultaneously, providing maximum loading on girders 2 and 3 (G 2 and G 3), respectively.

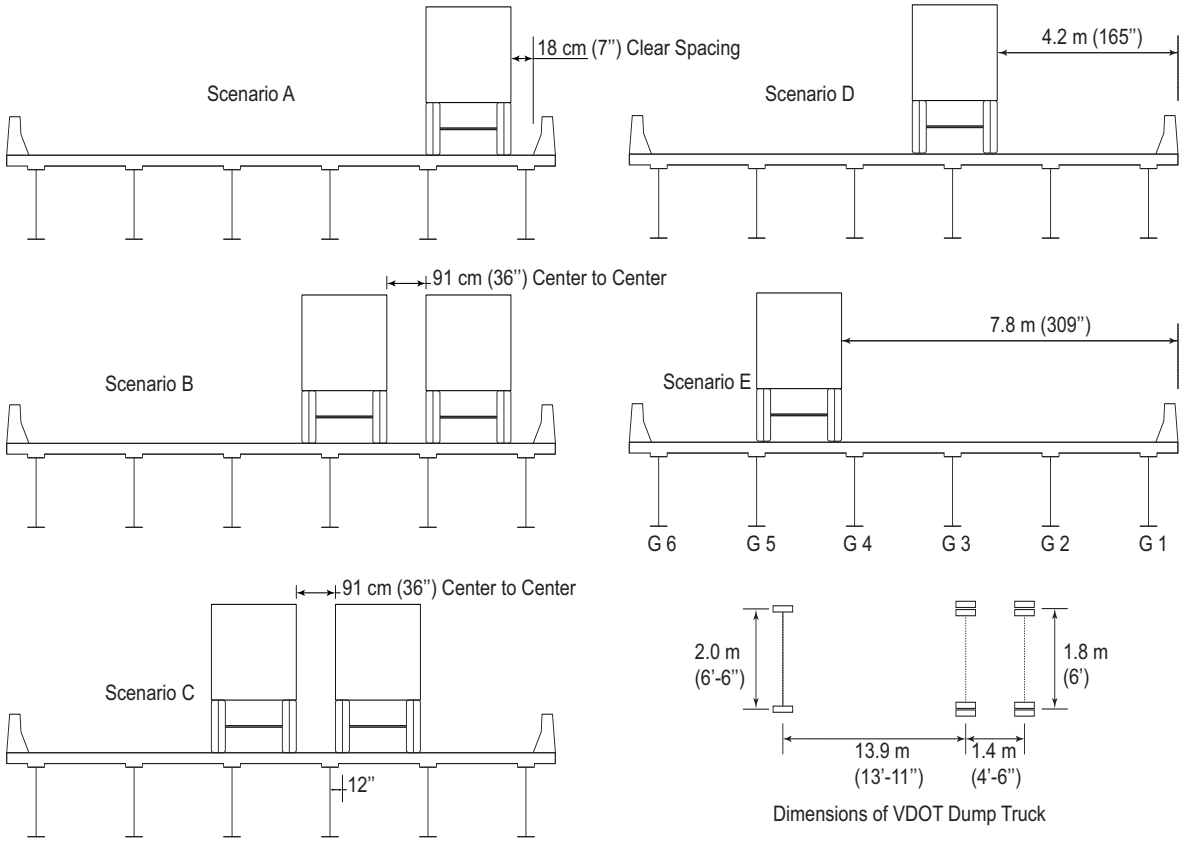

Figure 5-2 Loading scenarios and dimensions of loading trucks (Collins 2010)

In scenarios A, B and C, the testing trucks were driven at crawling speed to simulate static loads. Since these three scenarios apply static loading directly on girders, the validation and correlation studies in following sections will be based on scenarios A, B and C. The maximum longitudinal strains along the girder directions and vertical deflections on six girders under live loading are summarized in Table 5-1 for north span and Table 5-2 for south span (Collins, 2010).

Table 5-1 Strain and vertical deflection at bottom flange of girders on north span

Girder Number	Scenario A		Scenario B		Scenario C	
	Strain με ($x10^{-6}$)	Deflection (mm)	Strain με ($x10^{-6}$)	Deflection (mm)	Strain με ($x10^{-6}$)	Deflection (mm)
1	84.4	8.3	110	10.9	57.8	7.0
2	60.2	6.4	105.9	10.1	81.5	8.5
3	28.6	3.7	84.5	6.9	95.3	9.3
4	14.2	2.5	46.6	7.3	76.2	9.4
5	1.9	1.0	22.1	3.5	43.7	4.8
6	0	0.2	11.8	2.0	30	4.2

Table 5-2 Strain and vertical deflection at bottom flange of girders on south span

Girder Number	Scenario A		Scenario B		Scenario C	
	Strain με ($x10^{-6}$)	Deflection (mm)	Strain με ($x10^{-6}$)	Deflection (mm)	Strain με ($x10^{-6}$)	Deflection (mm)
1	72.7	8.4	91.4	10.8	48.4	7.1
2	61.3	6.5	105.3	9.7	75.9	8.3
3	29.9	4.6	85	9.9	90.8	10.2
4	15.2	2.7	50.1	6.7	81.6	N.A
5	3.3	1.0	24.1	3.4	46.8	5.3
6	0	0.0	8.8	1.8	28.2	4.3

5.3 NDE Measurements on Virginia Pilot Bridge

The concrete deck of Virginia Pilot Bridge is rated as in satisfactory condition (6 out of 9) by National Bridge Inventory (NBI 2009). Main deterioration types include surface cracking, concrete delamination at top reinforcing steel layer, and rebar corrosion. The Virginia Pilot Bridge was evaluated using an array of non-destructive evaluation (NDE) techniques on a 0.6 m (2 ft) grid. These techniques include chain drag, ground penetrating radar (GPR) and half-cell

potential, etc. Chain drag is an acoustic method that is based on sound changes while a set of chain links are dragged on bridge deck surface (ASTM 2012; Scheff and Chen 2000; Yehia et al. 2008). It is a rapid and inexpensive way to locate near surface delamination and severe stages of bridge deck deterioration, although results are influenced by inspectors' experience (Henderson et al. 1999). The unique feature of chain drag is that it evaluates deteriorations in a qualitative format. The deterioration mapping by chain drag indicates whether near surface delamination is present at testing locations or not. The qualitative representation of near surface concrete delamination measured on the Virginia pilot bridge by chain drag is shown in Figure 5-3, and the deteriorations are illustrated by discrete points on the testing grid.

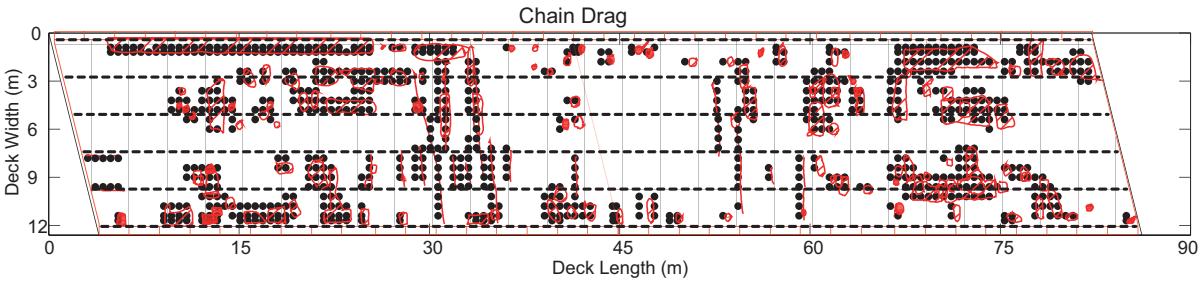

Figure 5-3 Deteriorations mapped by chain drag on Virginia Pilot Bridge

GPR is a high resolution electromagnetic technique and transmits high frequency radio waves into ground. When waves are reflected or scattered by an object with different electrical properties, e.g., voids due to concrete delamination, receiving antenna records the variations in reflected return signals (IAEA-TCS-17 2002). The signal attenuation, or loss of electromagnetic energy, is a common GPR physics indicating concrete deteriorations. Unlike chain drag, GPR measurement is expressed in a quantitative format. According to the research conducted by the author, a probability-based method is applicable to determine deterioration thresholds for selected confidence levels. This deterioration threshold is then used to differentiate quantitative

GPR data into binary representation, i.e., '1' for deteriorated and '0' for healthy (Zou and Moen 2014). In this paper, GPR data is mapped to the binary format by deterioration thresholds with 90%, 80% and 60% confidence levels, and correlations are studied with these deterioration thresholds. Figure 5-4 shows the binary representation of GPR measurements mapped by a 90% confidence level, i.e., -22 dB.

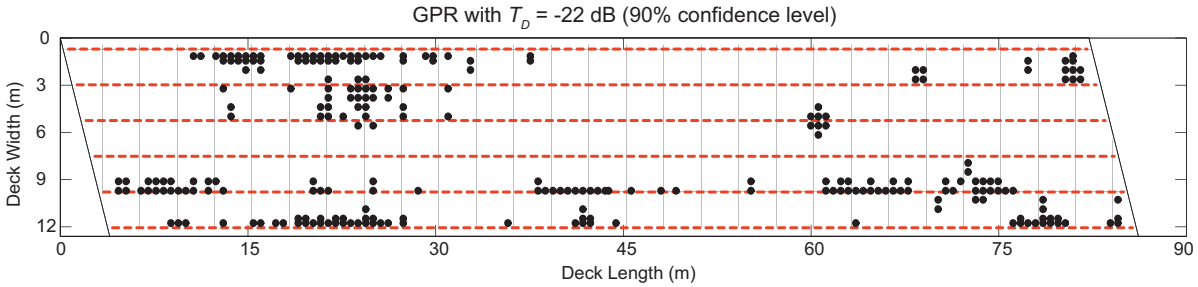

Figure 5-4 Deteriorations mapped by GPR on Virginia Pilot Bridge

Half-cell potential evaluates reinforcing steel corrosion by measuring potential of embedded reinforcing bars relative to a reference half-cell placed on the concrete surface. This potential value is the physics that half-cell potential uses to measure probability of reinforcing steel corrosion (Elsener 2001; Kyung et al. 2004). ASTM C876-09 (ASTM 2009) proposed deterioration thresholds for half-cell potential data, in which -0.35 Volts indicates a 90% probability of reinforcing steel corrosion. In Figure 5-5, half-cell potential data measured on Virginia Pilot Bridge is mapped by this deterioration threshold, i.e., -0.35 Volts, and deteriorations are shown as discrete points. The normalization of quantitative NDE data accommodates one option of correlation studies between finite element results and NDE deteriorations, and is presented in the following sections.

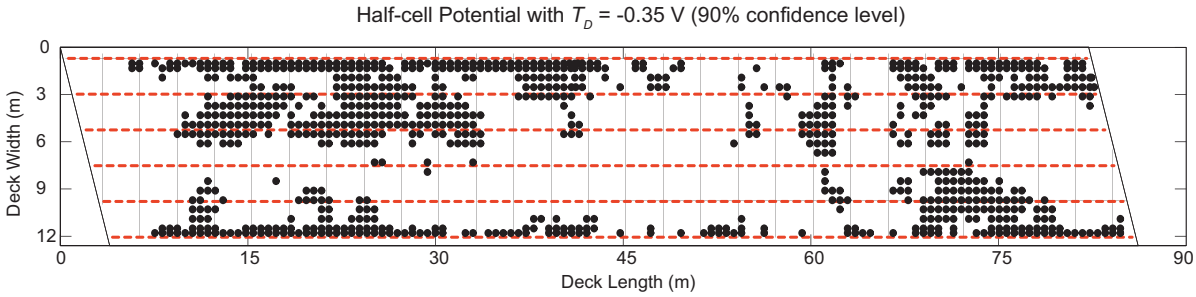

Figure 5-5 Deteriorations mapped by half-cell potential on Virginia Pilot Bridge

5.4 Finite Element Modeling of Virginia Pilot Bridge

Upon the physical testing performed on this bridge, the measured strains and deflections could be used to validate a finite element model, which makes it possible to evaluate the analytical model and study correlation between finite element results and deteriorations detected by NDE evaluations. The nonlinear commercial software ABAQUS (Hibbit et al. 2012) is used to perform analysis of the bridge. All structural components of VA Route 15 Bridge are modeled, including bridge deck, steel girders, diaphragm and guardrails (Figure 5-6(a)). Steel girders and concrete decks are modeled using the four-node shell elements with reduced integration (S4R) as illustrated in Figure 5-6(b), which are doubly curved general-purpose shell elements with hour-glass control. The linear general purpose shell in ABAQUS has the ability to switch from discrete Kirchhoff thin shell to moderately thick shell formulation (Mindlin shell) as the thickness increases. Bridge decks generally have a characteristic length to thickness ratio of greater than 15 therefore behaving as a thin shell, while the characteristic length to thickness ratios of girder flanges and webs change depending upon their thickness. Therefore, the four-node shell elements with reduced integration (S4R) could accurately model the behaviors of bridge components. The bridge deck is connected to steel girder top flanges and guardrails using ABAQUS MPC (multipoint constrain) rigid links to constrain six degrees of freedom in three

dimensional translations and rotations (Figure 5-6(b)). To accommodate those connections, nodes on the steel girders' top flange are located right below nodes on the deck, which means the coordinates of nodes in the bridge deck and steel girders connected by rigid links are same in the X and Y directions, but different in Z direction. Diaphragm and guardrails (center of gravity) are modeled using three dimensional linear beam elements (B31), which allow for transverse shear deformation. Since the diaphragms are pinned at both ends to the steel girders, the ABAQUS MPC Link elements are used to model the pin connection. Guardrails, on the other hand, are connected to the bridge deck by rigid links at nodes with same X and Y coordinates as connections between the deck and steel girders. According to a recent study (Bapat and Moen 2012), the boundary condition types, i.e., pin or roller, have little influence on this type of structural behavior; therefore, the simple pin and roller support conditions are applied to the ends of girders.

The material properties are taken from the bridge plans, with the concrete compressive strength of 28 MPa (4 ksi). By using the empirical equation, the elastic modulus is calculated as 25 MPa (3605 ksi) and rupture strength as 3.3 MPa (474 psi) for concrete bridge deck and guardrails; A linear property is applied to steel members, with a modulus of elasticity equals 200 GPa (29000 ksi), which is applied to steel girders and diaphragms. Under serviceability limit state, all structural components will behave linearly; therefore, linear elastic material properties are adequate to model the behavior of all components in the finite element model.

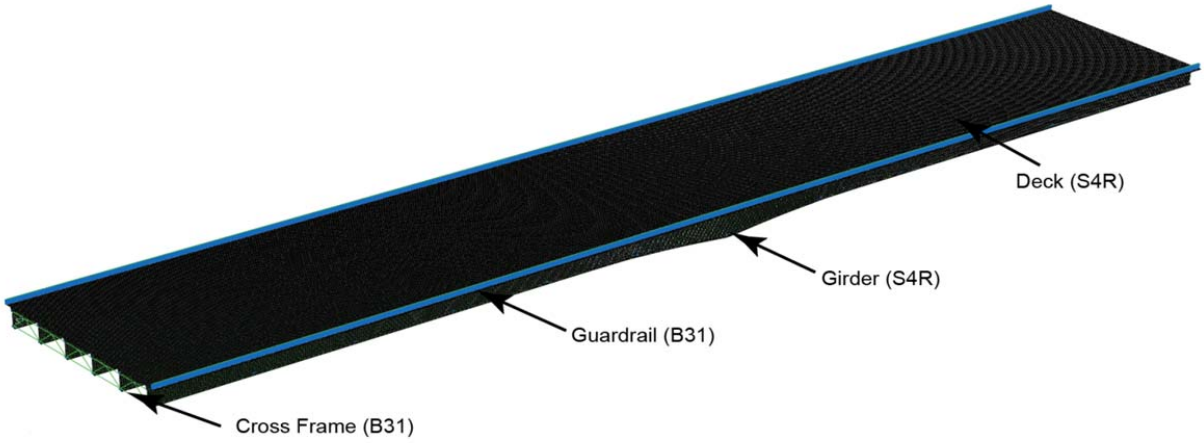

(a)

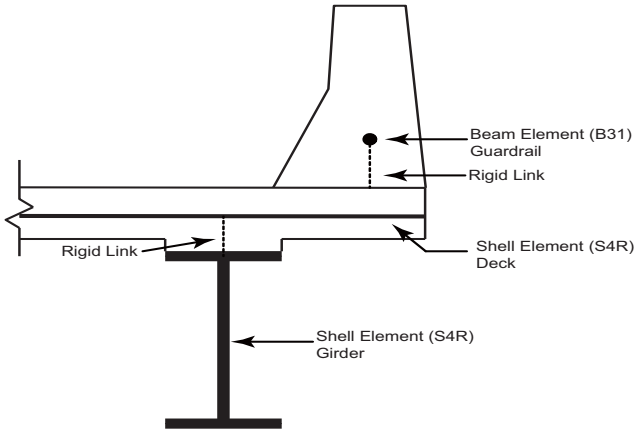

(b)

Figure 5-6 Finite element model (a) and element type (b) of Virginia Pilot Bridge

5.4.1 Live Loading

Live loads are applied according to the live load testing scenarios performed on the actual bridge (Scenarios A, B and C). Truck loads are simulated in the proposed bridge model by applying individual tire patches with a point load. Though the tire patch does not always match with a unique node in the finite element model, the point load is applied at the closest nodes to the

actual locations of truck loadings. The total length that a truck travels through the bridge deck is divided into 78 steps and static analysis is performed at each loading step. For each loading scenarios, the maximum and minimum stresses during 78 loading steps are recorded in both longitudinal and transverse directions. The maximum and minimum stresses then represent tensile and compressive stresses, respectively.

5.4.2 Concrete Shrinkage

Concrete shrinkage is a volume decrease phenomena due to physical and chemical changes in the cement paste (Nawy and Eng 1997), which is a main cause of the early age cracking of bridge decks and allows chloride irons to penetrate and further result to reinforcing steel corrosion, concrete delamination and spalling. The main types of concrete shrinkage are typically plastic, autogenous, carbonation and drying shrinkage (Kosmatka and Panarese 2005). Plastic shrinkage is caused by concrete moisture loss before the concrete sets, and autogenous shrinkage is due to the loss of water from the capillary pores (Holt and Janssen 1998). Carbonation shrinkage is associated with chemical reaction of various cement hydration products with carbon dioxide present in the air, and this type of shrinkage is usually limited to the surface of concrete (Mokaram 2002). Drying shrinkage is caused by the volumetric change due to drying of the concrete and the total shrinkage is defined as the sum of four individual types of shrinkage. For composite bridge structures, the bridge deck is restrained by the beam, reinforcing steel, shear connections and guardrails; when concrete begins to shrink, those restraints prevent the bridge deck from deforming freely, which then causes tensile stress in concrete (Akkaya et al. 2007). When the tensile stress exceeds concrete rupture strength, cracking may occur in concrete bridge deck (Shan and Weiss 2006).

Shrinkage of concrete is modelled by an application of a uniform strain profile across the depth of the slab, which is calculated based on the shrinkage strain of concrete (Levy 2010). The concrete ultimate strain is composed of shrinkage strain and creep strain. Since creep strain reduces the concrete total strain, the total strain in concrete is the shrinkage strain minus the creep strain. Altoubat and Lange (2001) managed to separate creep strains from shrinkage strains in an experiment, and it was observed that the ratio of creep strain over shrinkage strain is approximately 0.4 to 0.6. According to ACI 209.2R-08, the concrete shrinkage strain is 780 x 10-6 m/m (in./in.) (ACI 209); therefore, with ambient relative humidity h=0.6, fine aggregate percentage ϕ =50%, cement content c =409 kg/m3 (690 lb/ qd3) by using ACI 209R-92 model, the ultimate concrete shrinkage strain is 450 x 10-6 m/m (in./in.). In the finite element model, the ultimate shrinkage strain is treated as thermal strain, and the relation between ultimate shrinkage strain and the equivalent temperature variation is $\varepsilon_{sh,u} = \alpha_c \times \Delta T_{sh,u}$, where $\varepsilon_{sh,u}$ is the ultimate shrinkage strain, α_c is the thermal expansion coefficient of concrete and $\Delta T_{sh,u}$ is the equivalent temperature variation. Therefore, with the concrete thermal expansion coefficient equals to 12x10-6/°C, the ultimate equivalent temperature change in the concrete bridge deck is $\Delta T_{sh,u}$ =-37.5°C.

The modulus of elasticity of concrete is influenced by factors that affect the concrete shrinkage. Its value depends on the rate of loading, the stress level, the age of concrete at loading, the concrete mix proportions, and the relative humidity and temperature conditions. Besides, due to the effect of creep, the modulus of elasticity of concrete decreases as well when loads are sustained for longer time period (Shaker and Kennedy 1991,). In this paper, the effective concrete elastic modulus is calculated using the age-adjusted effective method (Bazant 1972), which is defined in Eq. (5-1).

$$E''(t,t_0) = \frac{E(t_0)}{1+\chi(t,t_0)\phi(t,t_0)} \quad (5\text{-}1)$$

Where E''(t,t0) is the age-adjusted effective modulus, E(t0) is the elastic modulus at time t0, χ(t,t0) is the aging coefficient and (t,t0) is the creep coefficient. The determination of aging coefficient, i.e., χ(t,t0), depends on the age at first loading, the duration of load, geometry of the loaded element, drying conditions and other factors; for practical implications, the aging coefficient can be accepted constant with an average value of 0.7 (Shaker and Kennedy 1991). The creep coefficient is determined to be 2.0 using ACI 209R-92 model, with the same parameters calculating ultimate shrinkage strain, and assuming 10 days of moist curing and loading starts at 30 days, respectively. Since the bridge deck concrete compressive strength equals to 28 MPa (4 ksi), the concrete elastic modulus is 25 GPa (3600 ksi) and the reduced concrete elastic modulus is 10 GPa (1500 ksi).

5.4.3 Finite Element Model Validation

The maximum longitudinal strains at steel girder bottom flanges and vertical diflections are recorded for live loading scenarios A, B and C. Strains and deflections by finite element analysis are then compared to field testing data summarized in Tables 5-1 and 5-2, and illustrated in Figure 5-7. It is found that the analytical results have good agreement with those from field testing. Under scenarios B live loading, vertical deflections predicted by analytical method are larger than those by field testing at exterior girders, indicating the finite element model is less stiff than the actual bridge. This is due to the less composite behavior. In this finite element model, steel girders and the concrete deck are connected at the center line of steel girder top flanges, therefore less stiff than the full connection between steel girder top flanges and the bridge deck in the actual bridge (Figure 5-6(b)). However, for strain comparisons at bottom of

steel girders, all three cases have good agreement between analytical results and field testings. Based on the validation results, the proposed finite element model is suitable for the structural analysis under live loading, and the findings are presented and discussed in the following sections.

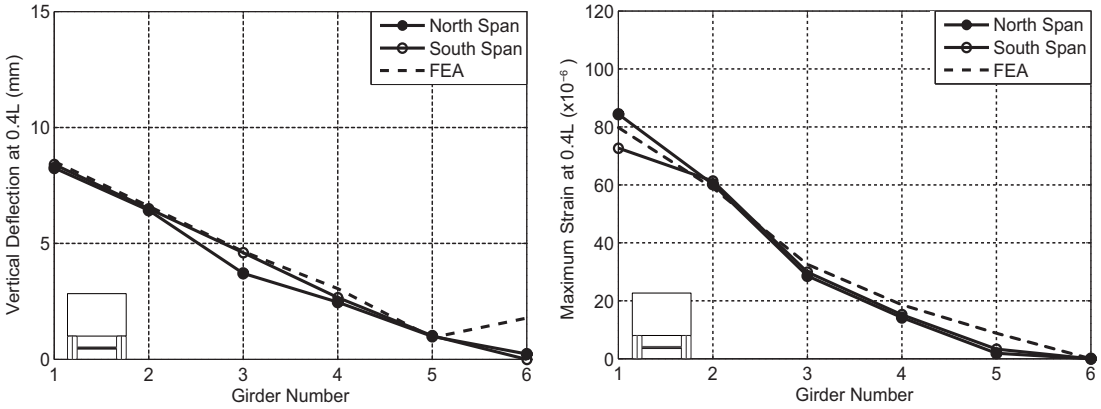

(a)

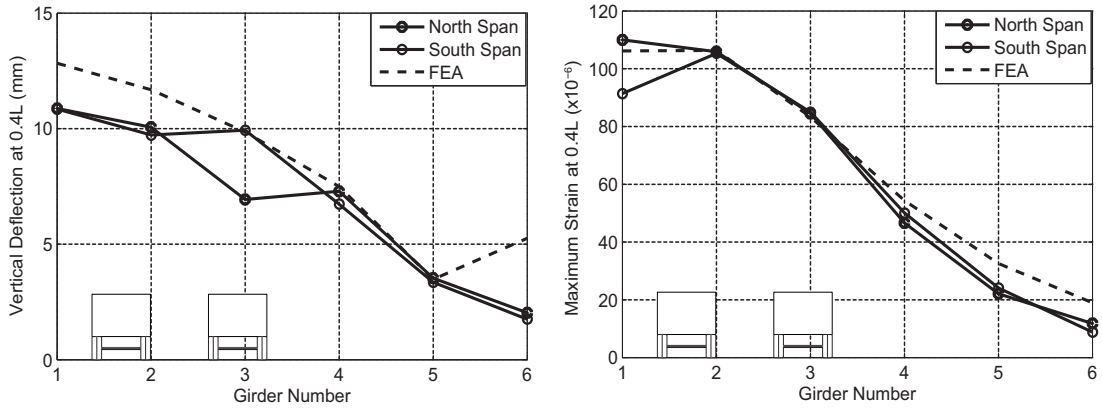

(b)

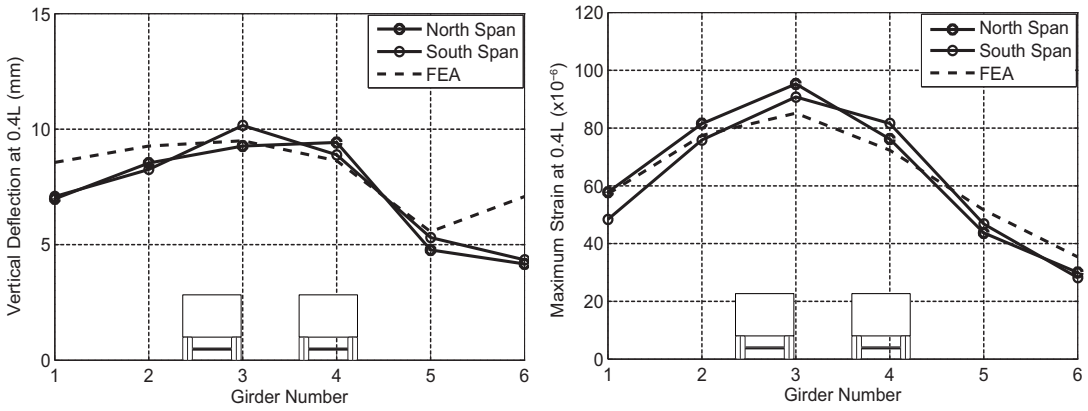

(c)

Figure 5-7 Comparison of maximum strain and vertical deflection at 0.4L for (a) scenario A, (b) scenario B and (c) scenario C

5.5 Correlation between Bridge Deck Stress and NDE Deterioration

Bridge decks experience tensile and compressive stresses under the live loading and concrete shrinkage. The study of potential correlations between these stresses and NDE deteriorations can help researchers understand causes of bridge deck deterioration. This correlation may also lead to the prediction of future deterioration.

Cracking allows harmful chemicals to penetrate into concrete bridge decks. When these chemicals make contact with reinforcing steel, corrosion may occur and accelerate the concrete deterioration process (Zhou 2005). Therefore, stresses inducing cracking are expected to be correlated with NDE measured deteriorations. Longitudinal and transverse crackings are the main cracking types present on concrete bridge decks, and these cracks are related to stresses in the transverse and longitudinal directions, respectively (Schindler et al. 2010). When stresses exceed concrete rupture strength, cracking can occur on the bridge deck surface. In the present finite element analysis, longitudinal and transverse stresses are recorded as S11 and S22, respectively (Figure 5-8). Therefore, correlations are studied between S11 and S22 stresses by

the finite element analysis and NDE measured deteriorations. Correlations are first studied by Pearson correlation coefficient which evaluates if a linear relation exists between two variables. In addition, both stresses and NDE data are normalized by deterioration thresholds (stresses by the concrete rupture strength (3.3 MPa), GPR and half-cell potential data by deterioration thresholds). The correlations are then evaluated by number of points identified as deteriorations by both stresses and NDE data. The correlation study begins with live load induced stresses in the following section.

5.5.1 Live Load Stress

In this section, stresses (S11 and S22) on the bridge deck surface due to live loadings are correlated with NDE data. With trucks travelling through, the bridge deck surface experiences both tensile and compressive stresses. When tensile stresses exceed the concrete rupture strength, i.e., 3.3 MPa (470 psi), cracking initiates and the locations are expected to be correlated with deteriorations mapped by NDE. In Figure 5-8(a-c), the maximum tensile and compressive stresses in longitudinal (S11) and transverse (S22) directions due to three scenarios' live loadings are plotted against girder numbers. As shown in Figure 5-8, live loads included tensile and compressive stresses are well below the concrete rupture strength and compressive strength, i.e., 28 MPa (4ksi). This indicates that concrete remains elastic under the live loading scenarios. Therefore live loadings are not the main causes to the initial cracking or concrete crushing on the bridge deck of Virginia pilot bridge. To study the worst case scenario, maximum tensile compressive stress from three live loading scenarios (A, B and C) are also plotted against girder numbers, shown in Figure 5-8(d), and this live loading worst case scenario will also be correlated with NDE deteriorations in the next section.

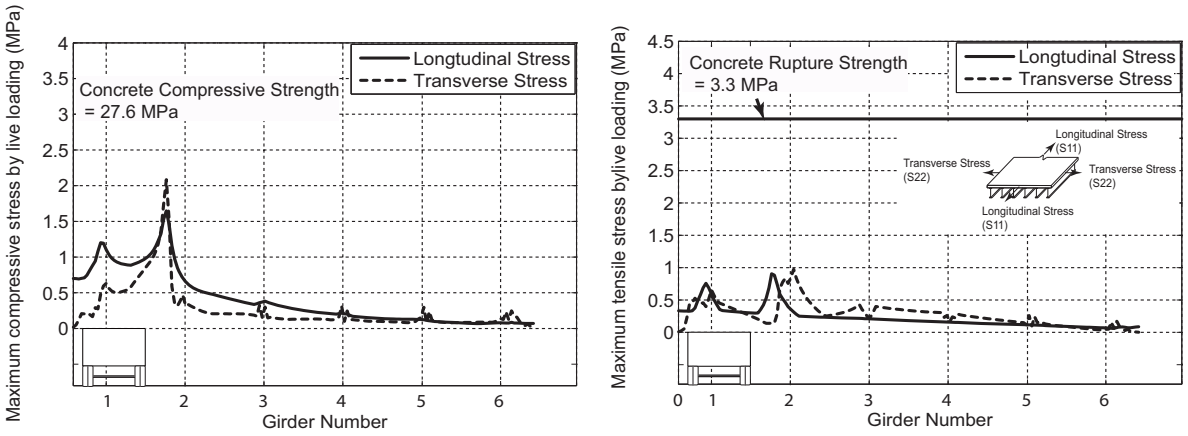
Maximum compressive stress by live loading (MPa)
Concrete Compressive Strength
= 27.6 MPa
Longtudinal Stress
Transverse Stress
Girder Number
Maximum tensile stress bylive loading (MPa)
Concrete Rupture Strength
= 3.3 MPa
Longtudinal Stress
Transverse Stress
Longitudinal Stress
(S11)
Transverse Stress
(S22)
Transverse Stress
(S22)
Longitudinal Stress
(S11)
Girder Number

(a)

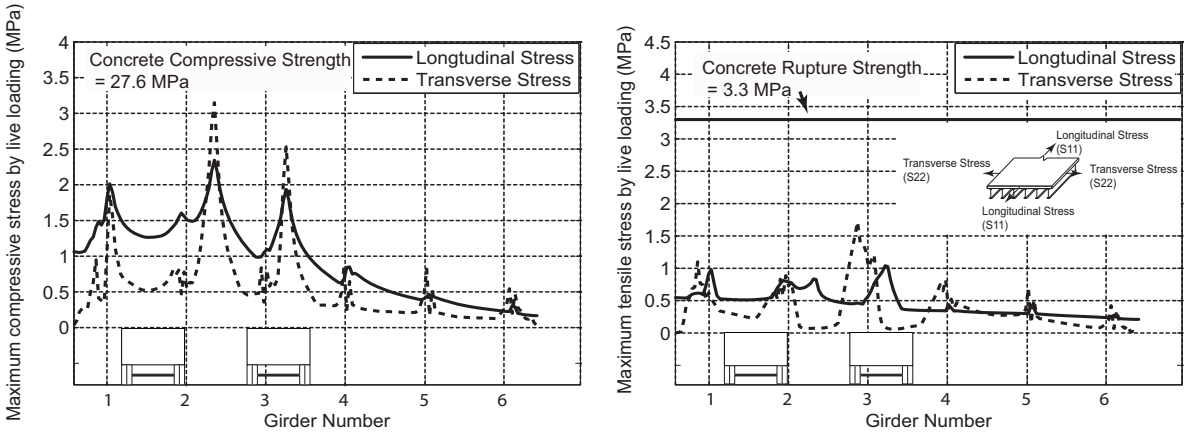
Maximum compressive stress by live loading (MPa)
Concrete Compressive Strength
= 27.6 MPa
Longtudinal Stress
Transverse Stress
Girder Number
Maximum tensile stress by live loading (MPa)
Concrete Rupture Strength
= 3.3 MPa
Longtudinal Stress
Transverse Stress
Longitudinal Stress
(S11)
Transverse Stress
(S22)
Transverse Stress
(S22)
Longitudinal Stress
(S11)
Girder Number

(b)

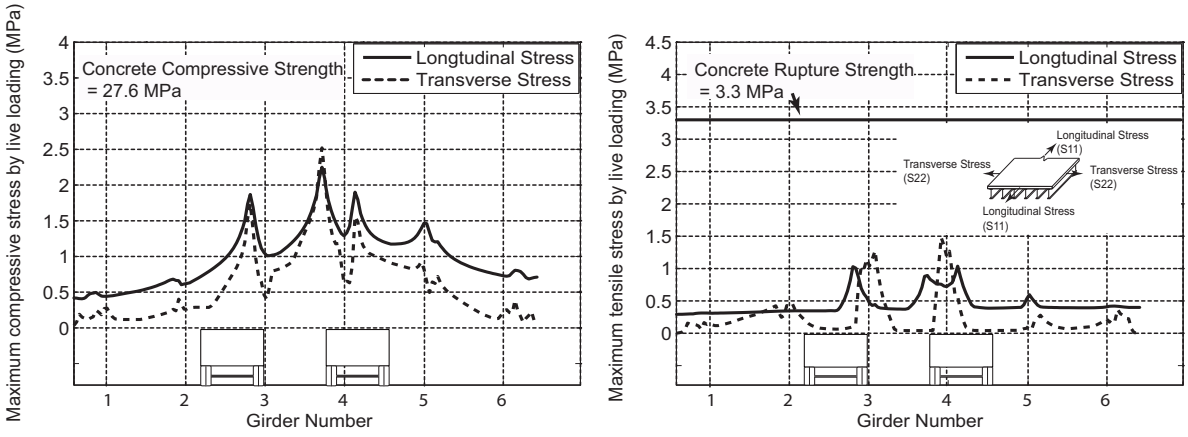
Maximum compressive stress by live loading (MPa)
Concrete Compressive Strength
= 27.6 MPa
Longtudinal Stress
Transverse Stress
Girder Number
Maximum tensile stress by live loading (MPa)
Concrete Rupture Strength
= 3.3 MPa
Longtudinal Stress
Transverse Stress
Longitudinal Stress
(S11)
Transverse Stress
(S22)
Transverse Stress
(S22)
Longitudinal Stress
(S11)
Girder Number

(c)

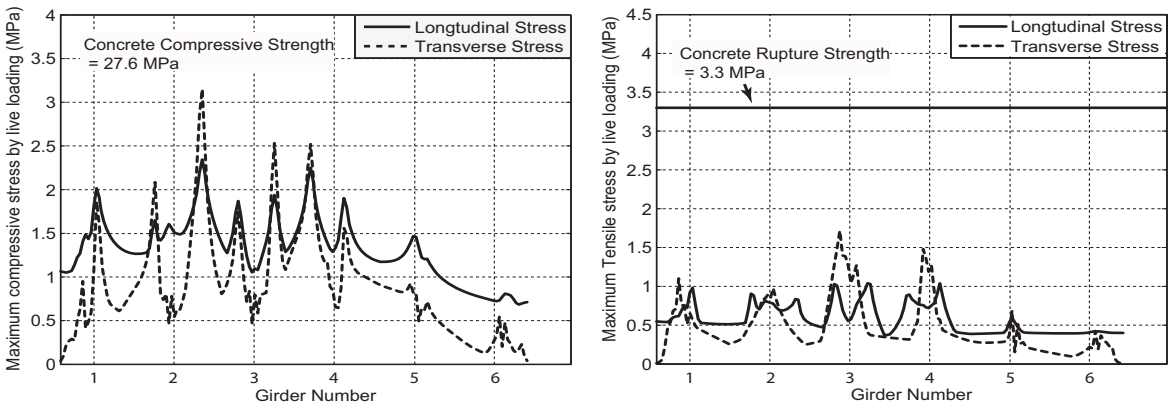

(d)

Figure 5-8 Maximum tensile and compressive stress along bridge deck width due to scenarios (a) A, (b) B, (c) C and (d) worst case live loadings

The correlations between live loading stresses and NDE data are studied by Pearson correlation coefficients. The Pearson correlation coefficient is a measure of the linear correlation between two variables, X and Y, giving a value between -1 and 1 inclusive, where 1 represents the total positive correlation, -1 the total negative correlation and 0 indicates no correlation between two variables (Figure 5-9). For the present correlation study, 1 indicates that high stresses are corresponding to high deteriorations and 0 indicates no correlation exists between stress and deteriorations. The Pearson's coefficient is calculated by Eq. (5-2) as:

$$r = \frac{\sum_{i=1}^{n}(X_i - \overline{X})(Y_i - \overline{Y})}{\sqrt{\sum_{i=1}^{n}(X_i - \overline{X})^2}\sqrt{\sum_{i=1}^{n}(Y_i - \overline{Y})^2}} \quad (5\text{-}2)$$

where $\overline{X}$ and $\overline{Y}$ are the sample means of the X (S11 and S22 stresses) and Y (NDE data) variables, respectively, and Xi and Yi are stresses and NDE data at data points, where NDE data was collected on the 0.6 m (2 ft.) grid on the bridge deck at testing. To perform direct comparisons, the longitudinal and transverse stresses extracted from finite element analysis are

interpolated to the NDE testing grid. Since the two correlated variables are representing different physics, e.g., stresses for finite element data and decibels for GPR data, the two variables are first normalized to dimensionless. In the present work, the tensile and compressive stresses are normalized by the captured maximum tensile and compressive stresses, respectively, and NDE data are normalized by the maximum measured data, e.g., -6 dB for GPR.

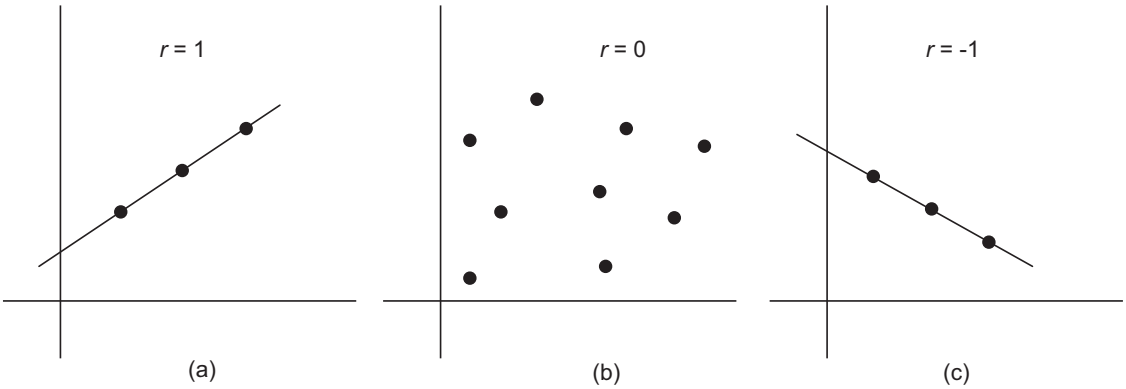

Figure 5-9 Pearson correlation between two variables with (a) positive linear correlation (b) no correlation and (c) negative linear correlation

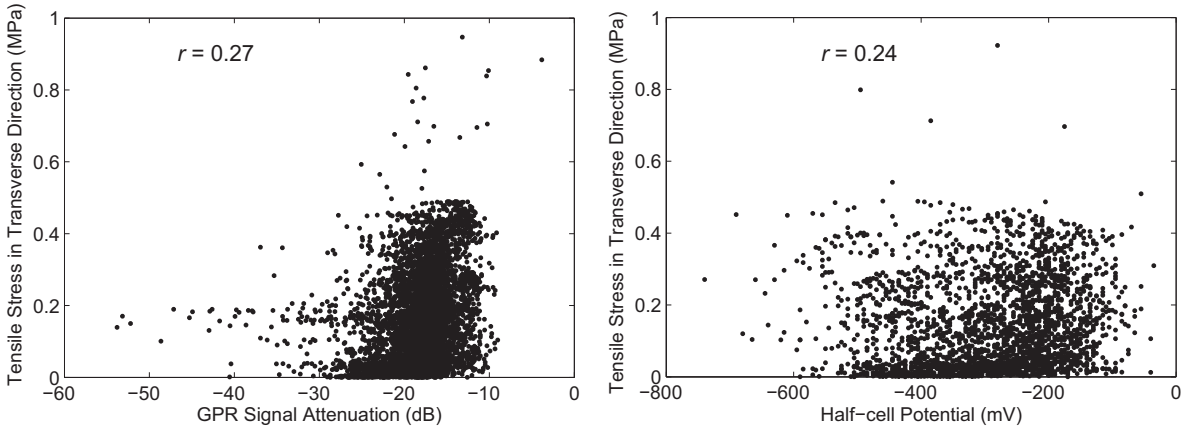

Figure 5-10 Pearson correlation coefficient between tensile stresses in transverse direction and NDE deteriorations

In Figure 5-10, the maximum correlation coefficients are shown between the transverse tensile stresses under live load scenario A and NDE data, which are 0.27 and 0.24 for GPR and half-cell potential, respectively. For all other live load cars, the Pearson correlation coefficient are all below these values. This indicates that there is no strong correlation between live load stresses and bridge deck deteriorations. Considering the maximum stresses induced by live loads are well below concrete rupture and crushing strength, live loads are not the main causes of bridge deck deteriorations on Virginia pilot bridge.

5.5.2 Shrinkage Stress

Concrete shrinkage creates tensile stresses on the bridge deck surface, especially at negative moment areas in continuous bridges. The tensile stresses in the longitudinal and transverse directions on the bridge deck surface are plotted against girder lines in Figure 5-11. The shrinkage induced longitudinal stresses can be assumed as one dimensional model and related to the concrete modulus of elasticity E and the coefficient of thermal expansion α as Eq. (5-3):

$$\sigma = CE\alpha\Delta T \tag{5-3}$$

Where C =1 for fully constrained bridge decks and C = 0 for free decks, and ΔT = 37.5 °C is the uniform temperature change simulating concrete ultimate shrinkage. According to a numerical study, the C value could be assumed as 0.34 for continuous steel girder bridges with composite behavior (William et al. 2008). Therefore, the shrinkage induced longitudinal stress is approximately 3.9 MPa by Eq. (5-3), which is close to the longitudinal tensile stress obtained through the finite element analysis shown in Figure 5-11.

Compared with live loading, shrinkage induced tensile stresses in the longitudinal direction are larger than the concrete rupture strength. This indicates that cracking is initiated under concrete ultimate shrinkage in the transverse direction. The transverse tensile stresses, on the other hand,

are well below concrete rupture strength in the interior areas between girder 1 and 6, but beyond the limit at the exterior of girder 1 and 6. These phenomena are consistent with observations that transverse cracking is more commonly present on the concrete deck surface than the longitudinal cracking. In addition, due to restraints along girder lines, e.g., shear studs, bridge deck areas near steel girder top flanges are experiencing higher longitudinal tensile stresses as well.

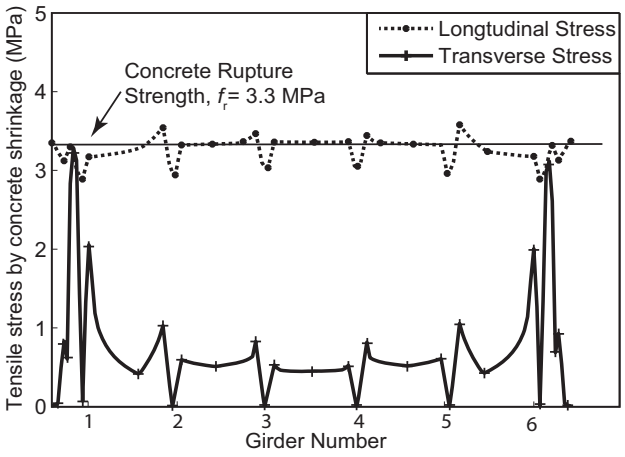

Figure 5-11 Shrinkage induced tensile stress along bridge deck width

As the live load correlation study, tensile stresses in longitudinal (S11) and transverse (S22) directions are interpolated to the NDE measurement grid. The correlation is then studied by normalizing stresses and quantitative NDE data to a binary format, where '0' is for healthy and '1' is for deteriorated locations. Stresses are normalized by the concrete rupture strength, i.e., locations with tensile stresses greater than 3.3 MPa are deteriorated, and vice versa. The NDE data is normalized by corresponding deterioration thresholds. The half-cell potential data is normalized by -0.35 Volts, which is the deterioration threshold proposed by ASTM (ASTM C876-09 2009) with 90% probability of reinforcing steel corrosion. For the GPR data, three deterioration thresholds are used, which are -22 dB, -20 dB and -19 dB representing 90%, 80%

and 60% confidence levels, respectively (Zou and Moen 2014). Concrete rupture strength, i.e., 3.3 MPa (470 psi), is used as the threshold value to normalize shrinkage stresses, where concrete cracking will initiate with stresses exceeding this limit.

The correlation results are shown in Figure 5-12, where the percent match is used to demonstrate number of points identified as deteriorated by both tensile stresses and NDE data. Through correlation study, the percent matches are 24%, 14%, and 26% between longitudinal stresses (S11) and chain drag, GPR and half-cell potential, respectively. Pearson correlation coefficients indicate there are no strong correlations between either NDE measurements with stresses in both directions. This is reasonable since deteriorations are distributed across the bridge deck, while tensile stresses beyond concrete rupture strength are accumulated at negative moment areas, as demonstrated in Figure 5-12. The correlations are greatly increased when stresses and NDE data are correlated by the binary format; this is because NDE measured deteriorations near the center pier (negative moment areas) are all captured by tensile stresses higher than the concrete rupture strength. Tensile stresses in transverse direction (S22) have almost no correlation with deteriorations by either method, since the concrete shrinkage induces transverse stresses are well below the concrete rupture strength. This also explains the presence of fewer shrinkage induced longitudinal cracking on concrete bridge decks. In addition, the GPR data with lower confidence levels has higher correlation with longitudinal stresses, since lower confidence levels result in more bridge deck areas identified as deteriorated.

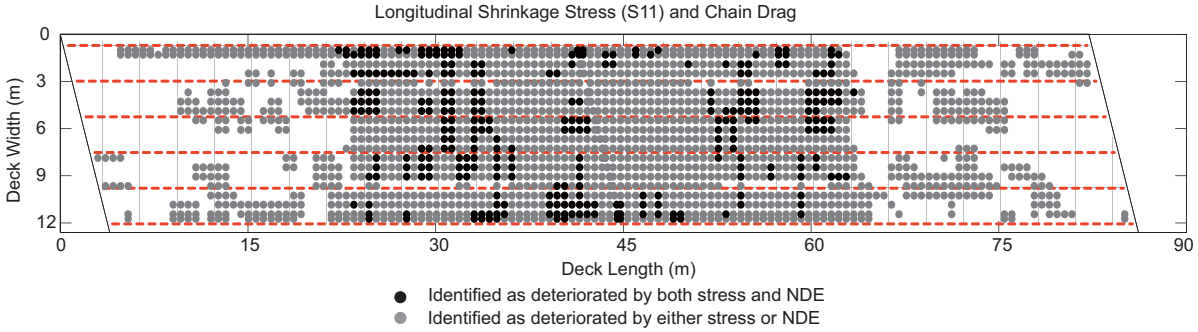

(a)

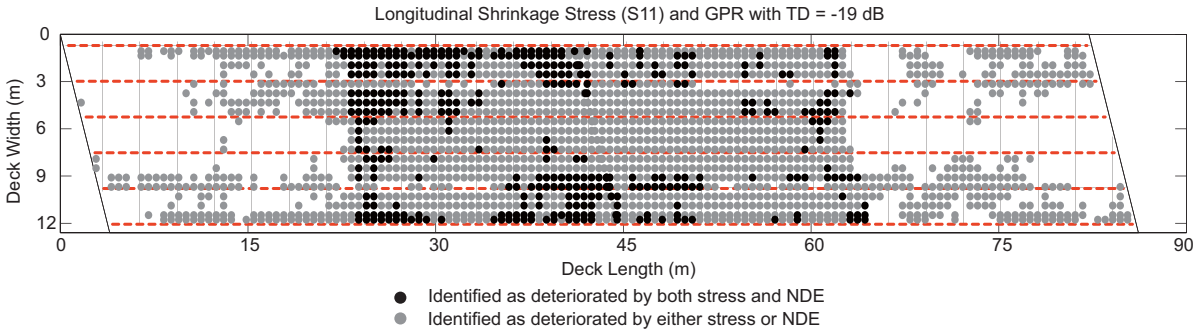

(b)

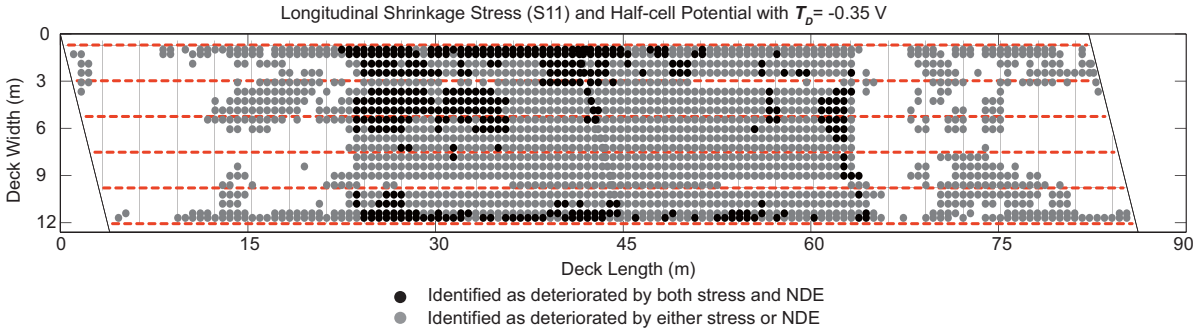

(c)

Figure 5-12 Correlations between bridge deck longitudinal stress (S11) and (a) chain drag, (b) GPR with -19 dB threshold and (c) half-cell potential with -0.35 V threshold value

5.6 Conclusion

This paper presents a correlation study between live load and concrete shrinkage induced stresses on the bridge deck surface with deteriorations measured by NDE techniques. Concrete shrinkage

results in high tensile stresses in the longitudinal direction on the bridge deck surface, which are likely to exceed the concrete rupture strength and initiating concrete cracks. The statistical study shows little correlation between either longitudinal or transverse shrinkage stresses with NDE data. However, the finite element analysis shows accumulated high longitudinal stresses at negative moment areas, which result in transverse cracking as commonly presented in continuous bridge decks. Transverse shrinkage stresses, are well below the concrete rupture strength, therefore are not a main factor that causes concrete bridge deck cracking on the Virginia pilot bridge. Further, tensile stresses due to live loading in both directions are well below concrete rupture strength, therefore live loading is considered to be the secondary effect on bridge deck cracks.

This study indicates that concrete shrinkage is the main factor resulting in bridge deck cracking and other potential deteriorations. Reducing concrete shrinkage can help decrease bridge deck deteriorations and improve bridge decks' service life. This can be achieved by applying low shrinkage concrete and/or concrete with higher rupture strength.

Chapter 6: Conclusion

6.1 Conclusion

This dissertation presents a general probability-based approach to identify deterioration thresholds for NDE measurements with quantitative results. The quantitative NDE data are then normalized by using defined thresholds to assess bridge deck condition. The correlations are also investigated between live load and shrinkage stress on the concrete surface with NDE measured deteriorations.

This probability-based threshold definition allows end users to specify desired confidence levels, and identify 'truly' deteriorations with respective probabilities. Concrete properties, environmental factors and NDE equipment properties are used to develop statistical distribution of measured NDE underlying physics for healthy concrete, and this features the link between the bridge decks with all healthy concrete and actual bridge decks. Bridge decks are assessed by overlapping deteriorations at discrete points by different NDE measurements. Assessments are conducted for two groups, for NDE techniques measuring similar or different underlying physics. For both cases, overlapping NDE data is capable to identify most possible deterioration areas, as well as locations with potential future deteriorations.

The correlation study is conducted between live load and concrete shrinkage induced stresses on bridge deck top surface with deteriorations measured by NDE techniques. The reinforced concrete bridge deck is constrained at the bottom surface by shear studs connected with steel girders, due to which concrete drying shrinkage results in high tensile stresses on the bridge deck surface, which exceed the concrete rupture strength and initiate concrete cracking. Though the statistical study shows small correlation between either longitudinal or transverse stresses with

measured deteriorations, the finite element analysis does show accumulated high longitudinal stresses at negative moment areas, which result in transverse cracking as commonly presented in continuous bridge decks. Transverse stresses, on contrary, are well below the concrete rupture stress, therefore is not a main factor that causes concrete bridge deck cracking. Further, the concrete shrinkage induced tensile stresses are relatively higher than those due to traffic loading, therefore live loading is not considered to be the secondary effect on bridge deck cracking. This study also indicates concrete shrinkage is the main factor that results in bridge deck cracking and other deterioration types, therefore reducing concrete drying shrinkage could potentially increase the service life of concrete bridge deck. This can be achieved by applying low shrinkage concrete and concrete with higher rupture strength.

Among the studied NDE techniques, chain drag is the most accessible and does not require advanced understanding of background theories. Through comparison with drilled core samples, chain drag provides reasonable accuracy even higher than other advanced NDE techniques; therefore chain drag is a preferred tool in many DOTs. However, chain drag is only capable to detect near surface delamination. When measuring degradation deep in concrete decks, or other deterioration types, e.g., reinforcing steel corrosion, advanced NDE techniques measuring particular underlying physics supplement the chain drag method.

6.2 Future Work

The future work included the following parts.

(1) When deriving mean and standard deviation of GPR signal attenuation for healthy concrete, an iterative procedure is introduced to determine electrical conductivity of concrete. A refined method will be developed to eliminate this procedure. This can be achieved by application of the concrete bulk electrical conductivity measured directly on actual bridge decks.

(2) Existing cracks on the bridge deck surface accelerate the process of reinforcing steel corrosion, which causes further bridge deck deterioration. Therefore, crack distributions are expected to be correlated with deteriorations. A refined finite element model with nonlinear concrete material properties is capable to simulate crack distributions on concrete bridge decks. The successful nonlinear finite element model requires concrete properties measured experimentally, e.g., the post-cracking stress strain relations. The testing can be conducted on core samples obtained from actual bridges to refine the finite element model.

(3) The long-term behaviors of bridge structures will be studied based on this refined finite element model. Long-term effects include accumulate live loading stresses, concrete shrinkage stresses and stresses due to temperature variations.

(4) Parametric studies can be performed to identify sensitivity of bridge deck deteriorations to numerous variables. Potential variables include the spacing of reinforcing steel, clear cover of reinforcing steel and concrete compressive strength. Design recommendations can then be proposed to reduce deteriorations on the concrete bridge deck.

Reference

AASHTO (2007). "LRFD bridge design specifications." Washington, DC: American Association of State Highway and Transportation Officials.

Akkaya, Y., Ouyang, C., and Shah, S. P. (2007). Effect of supplementary cementitious materials on shrinkage and crack development in concrete.Cement and Concrete Composites, 29(2), 117-123.

Altoubat, S. A., and Lange, D. A. (2001). Creep, shrinkage, and cracking of restrained concrete at early age. ACI Materials Journal, 98(4).

American Concrete Institute. Prediction of Creep, Shrinkage, and Temperature Effects in Concrete Structures. ACI 209R-92 (Reapproved 2008). 65, 66

Andrade, C., and D'Andrea, R. "The use of electrical resistivity as a NDT for the specification of concrete durability." Proc., 6th International Conference on Concrete under Severe Conditions-Environment and Loading, CONSEC'10, June 7, 2010 - June 9, 2010, CRC Press, 195-200.

Archie, G. E. (1942). The electrical resistivity log as an aid in determining some reservoir characteristics. Trans. AIMe, 146(1), 54-62.

ASTM Standard C876-09. (2009). "Standard Test Method for Corrosion Potentials of Uncoated Reinforcing Steel in Concrete." ASTM International, West Conshohocken, PA. DOI: 10.1520/C0876-09, www.astm.org

ASTM Standard D4580-03. (2012). "Standard Practice for Measuring Delaminations in Concrete Bridge Decks by Sounding." ASTM International, West Conshohocken, PA. DOI: 10.1520/D4580-03R12, www.astm.org

ASTM Standard D4580-03. Standard Practice for Measuring Delaminations in Concrete Bridge Decks by Sounding. ASTM International, West Conshohocken, PA. DOI: 10.1520/D4580-03R12, www.astm.org, 2012. Accessed July 19, 2013.

Bapat, A. V., and Moen, C. D. (2012). Finite Element Parameter Studies of a Skewed Composite Steel Girder Bridge. In Transportation Research Board 91st Annual Meeting (No. 12-0787).

Barnes, C.L., Trottier, J.F., and Forgeron, D. (2008). "Improved concrete bridge deck evaluation using GPR by accounting for signal depth-amplitude effects." NDT and E International, 41(6), 427-433.

Barth, K. E., and Wu, H. (2006). "Efficient nonlinear finite element modeling of slab on steel stringer bridges." Finite elements in analysis and design, 42(14), 1304-1313.

Bazant, Z. P. (1972). Prediction of concrete creep effects using age-adjusted effective modulus method. ACI Journal, 69(4), 212-217.

Belli, K. and S. Wadia-Fascetti. The Correlation of GPR Bridge Deck Assessment Data to Ground Truth. Center for Subsurface Sensing and Imaging Systems, Department of Civil and Environmental Engineering, Northwestern University, Evanston, IL, 2002. http://www1.coe.neu.edu/~kbelli/ricc/kmb_ricc2002.pdf. Accessed August 25, 2003.

Belli, K., Wadia-Fascetti, S., and Rappaport, C. (2008). "Model based evaluation of bridge decks using ground penetrating radar." Computer-Aided Civil and Infrastructure Engineering, 23(1), 3-16.

Biggs, R. M., Barton, F. W., Gomez, J. P., Massarelli, P. J., and McKeel Jr, W. T. (2000). "Finite element modeling and analysis of reinforced-concrete bridge decks."

Bouteiller, V., Toque, C., Cury, A., Cherrier, J.-F., Diday, E., and Cremona, C. (2012). "Non-destructive electrochemical characterizations of reinforced concrete corrosion: Basic and symbolic data analysis." Corrosion Reviews, 30(1-2), 47-62.

Breysse, D., and Garnier, V. (2012). "Deterioration Processes in Reinforced Concrete : An Overview." Springer Netherlands, 28-56.

Cady, P. D., and Weyers, R. E. (1984). "Deterioration rates of concrete bridge decks." Journal of Transportation Engineering, 110(1), 34-44.

Collins, W. N. (2010). "Live Load Testing and Analysis of the Southbound Span of U.S. Route 15 over Interstate-66." Master of Science Master's Thesis, Virginia Tech, Blacksburg, VA.

Conyers, L. What is G.P.R.? Anthropology Department, University of Denver, Denver, CO. http://www.du.edu/~lconyer/. Accessed August 25, 2003.

Daniels, D. J. (Ed.). (2004). Ground penetrating radar (Vol. 1). Iet.

Elsener, B. (2001). "Half-cell potential mapping to assess repair work on RC structures." Construction and Building Materials, 15(2-3), 133-139.

Finch, R., R. Fischer, M. Grimes, R. Stits, and W. A. Watkins. Acceptable Methods, Techniques, and Practices-Aircraft Inspection and Repair, Chapter 5, Section 5. Report AC 43.13-1B. Federal Aviation Administration, U.S. Department of Transportation, Washington, DC, September 1998. http://av-info.faa.gov/dst/43-13/. Accessed August 25, 2003.

Ghasemi, H., Penrod, J., and Hooks, J.M. (2009). “Developing advanced methods of assessing bridge performance.” FHWA-HRT-10-001, FHWA.

Goueygou, M., Abraham, O., and Lataste, J. F. (2008). "A comparative study of two non-destructive testing methods to assess near-surface mechanical damage in concrete structures." NDT and E International, 41(6), 448-456.

Gowers, K. R., and Millard, S. G. (1999). "Measurement of concrete resistivity for assessment of corrosion severity of steel using Wenner technique." ACI Materials Journal, 96.

Ground Penetrating Radar for Measuring Pavement Layer Thickness. Report FHWA-HIF-00-015, Federal Highway Administration, U.S. Department of Transportation, Washington, DC. http://www.fhwa.dot.gov/infrastructure/asstmgmt/gprbroc.pdf. Accessed August 25, 2003.

Ground Penetrating Radar: Basic Operating Principles. GeoModel, Inc., Leesburg, VA. http://www.geomodel.com/gprtext.htm. Accessed August 18, 2003.

Gucunski, N., Imani, A., Romero, F., Nazarian, S., Yuan, D., Wiggenhauser, H., Shokouhi, P., Taffe, A., and Kutrubes, D. (2013). "Nondestructive testing to identify concrete bridge deck deterioration." Transportation Research Board, Washington, D.C.

Gucunski, N., Romero, F. A., Shokouhi, P., and Makresias, J. (2005). "Complementary Impact Echo and Ground Penetrating Radar Evaluation of Bridge Decks on I-84 Interchange in Connecticut." Earthquake Engineering and Soil Dynamics, 1-10.

Gucunski, N., Romero, F., Kruschwitz, S., Feldmann, R., Abu-Hawash, A., and Dunn, M. (2010). "Multiple Complementary Nondestructive Evaluation Technologies for Condition Assessment of Concrete Bridge Decks." Transportation Research Record: Journal of the Transportation Research Board, 2201(-1), 34-44.

Gucunski, N., Romero, F.A., Shokouhi, P., and Makresias, J. Complementary Impact Echo and Ground Penetrating Radar Evaluation of Bridge Decks on I-84 Interchange in Connecticut. Earthquake Engineering and Soil Dynamics, 2005, pp. 1-10.

Gucunski, N., S. Antoljak, and A. Maher. Seismic Methods in Post Construction Condition Monitoring of Bridge Decks. In Use of Geophysical Methods in Construction, No. 108, 2000, pp. 35-51.

Guthrie, W. S., and Tuttle, R. S. (2006). "Condition analysis of concrete bridge decks in Utah." Utah Department of Transportation Research and Development Division, Utah.

Halabe, U.B., Maser, K.R., Kausel E., Propagation Chracteristics of Electromagnetic Waves in Concrete. U.S. Army Research Report, MIT, 1989.

Heckroodt, R. O. (2002). Guide to the deterioration and failure of building materials, Inst of Civil Engineers Pub.

Hema, J., Guthrie, W.S., and Fonseca, F.S. Concrete Bridge Deck Condition Assessment and Improvement Strategies. Report UT-04-16. Department of Civil and Environmental Engineering, Brigham Young University, Provo, Utah, November 2004.

Henderson, M. E., Dion, G. N., and Costley, R. D. Acoustic inspection of concrete bridge decks. Proceedings of SPIE - The International Society for Optical Engineering, 3587, 1999, pp. 219-227.

Hibbitt, D., Karlsson, B. and Sorensen, P. (2012). Abaqus/Standard User's Manual, Version 6.12. Hibbitt, Karlsson and Sorensen Inc., Pawtucket, Rhode Island.

Hillerborg, A., Mod??er, M., and Petersson, P. E. (1976). "Analysis of crack formation and crack growth in concrete by means of fracture mechanics and finite elements." Cement and concrete research, 6(6), 773-781.

Holt, E. E., and Janssen, D. J. (1998). Influence of early age volume changes on long-term concrete shrinkage. Transportation Research Record: Journal of the Transportation Research Board, 1610(1), 28-32.

Huston, D. R., Cui, J., Burns, D., and Hurley, D. (2010). "Concrete bridge deck condition assessment with automated multisensor techniques." Structure and Infrastructure Engineering, 1-11.

IAEA-TCS-17 (2002). "Guidebook on non-destructive testing of concrete structures." International Atomic Energy Agency, Vienna, Austria.

Kosmatka, S. H., and Panarese, W. C. (2002). Design and control of concrete mixtures (Vol. 5420). Skokie, IL: Portland Cement Association.

Kovler, K. (1997). Drying creep of concrete in terms of the age-adjusted effective modulus method. Magazine of Concrete Research, 49(181), 345-351.

Kyung, J.-W., Yokota, M., Leelalerkiet, V., and Ohtsu, M. "Practical use of half-cell potential method for NDE of corrosion of reinforced concrete structure." Proc., Proceedings of the 11th Asian Pacific Conference on Nondestructive Testing, November 3, 2003 - November 7, 2003, Trans Tech Publications Ltd, 1638-1644.

Lee, C.-W. (2011). Simulations of long-term bridge deck deterioration due to corrosion.

Levy, C. (2010). Numerical Investigation of the Effects of Shrinkage and Thermal Loading on the Behaviour of Misaligned Dowels in Jointed Concrete Pavement. Civil and Environmental Engineering, University of Waterloo. Master of Applied Science.

Maierhofer, C., Reinhardt, H.-W., and Dobmann, G. (2010). "Non-Destructive Evaluation of Reinforced Concrete Structures, Volume 1 - Deterioration Processes and Standard Test Methods." Woodhead Publishing, 28-56.

Manning, D.G. (1985). "Detecting Defects and Deterioration in Highway Structures." NCHRP Synthesis of Highway Practice 118. National Cooperative Highway Research Program, TRB, National Research Council, Washington, D.C.

Maser, K. R., K. Tabrizi, and V. Gangi. Use of Nondestructive Methods for Large Scale Bridge Deck Evaluation. Reliability Subcommittee (A2K05), TRB, National Research Council, Washington, DC, 2001.

Maser, K.R., New Technology for Bridge Deck Assessment. New England Transportation Consortium Phase I Final Report, Center for Transportation Studies, MIT, 1989.

Mokarem,D.W.(2002). Development of concrete shrinkage performance specifications (Doctoral dissertation, Virginia Polytechnic Institute and State University).

National Bridge Inventory (NBI). (2003). United States NBI Rep. 2009, <www.nationalbridgeinventory.com/nbireport200322.htm>

Nawy, E. G., and Eng, D. (1997). Long-Term Effects and Serviceability. Concrete Construction Engineering Handbook, 4-1.

Oh, T., Kee, S., Arndt, R., Popovics, J., and Zhu, J. (2012). "Comparison of NDT Methods for Assessment of a Concrete Bridge Deck." Journal of Engineering Mechanics, 139(3), 305-314.

Rhazi, J., Dous, O., and Laurens, S. A new application of the GPR technique to reinforced concrete bridge decks. Proc., 4th Middle East NDT Conference and Exhibition, Kingdom of Bahrain, 2007.

Roberts, G. E. "Ground-penetrating radar evaluation of bridge decks." Proc., Nondestructive Evaluation of Aging Bridges and Highways, June 6, 1995 - June 7, 1995, Society of Photo-Optical Instrumentation Engineers, 59-67.

Romero, F. A., Roberts, G. E., and Roberts, R. L. Evaluation of GPR bridge deck survey results used for delineation of removal/maintenance quantity boundaries on asphalt-overlaid,

reinforced concrete deck. Structural Materials Technology IV; an NDE Conference, 2010, pp. 23-30.

Saadeghvaziri, M. A., and Hadidi, R. (2005). "Transverse cracking of concrete bridge decks: Effects of design factors." Journal of Bridge Engineering, 10(5), 511-519.

Saarenketo, T. and M. K. Soderqvist. Ground Penetrating Radar Applications for Bridge Deck Evaluations in Finland. Insight, Vol. 36, No. 7, July 1994, pp. 496-501.

Scheff, J., and Chen, R. (2000). "Bridge deck inspection using chain drag and ground penetrating radar." Condition monitoring of materials and structures. American Society of Civil Engineers.

Schindler, A. K., Hughes, M. L., Barnes, R. W., and Byard, B. E. (2010). "Evaluation of Cracking of the US 331 Bridge Deck." Highway Research Center and Department of Civil Engineering at Auburn University.

Scott, M., Rezaizadeh, A., Delahaza, A., Santos, C. G., Moore, M., Graybeal, B., and Washer, G. "A comparison of nondestructive evaluation methods for bridge deck assessment." Proc., Structural Faulst and Repair, July 4, 2001 - July 6, 2001, Elsevier Ltd, 245-255.

Shah, A. A., and Ribakov, Y. (2008). "Non-destructive measurements of crack assessment and defect detection in concrete structures." Materials & Design, 29(1), 61-69.

Shah, H. R., and Weiss, J. (2006). Quantifying shrinkage cracking in fiber reinforced concrete using the ring test. Materials and structures, 39(9), 887-899.

Shaker, A. F., and Kennedy, D. L. (1991). The effective modulus of elasticity of concrete in tension. Department of Civil Engineering, University of Alberta, Canada.

Shapiro, K. (2007). "Finite-element modeling of a damaged prestressed concrete bridge."

Sharma, P. V. Environmental and Engineering Geophysics. Cambridge Printing Press, Cambridge, United Kingdom, 1997.

Shin, H. and D. A. Grivas. (2003). How Accurate is Ground Penetrating Radar (GPR) for Bridge Deck Condition Assessment? Department of Civil and Environmental Engineering, Rensselaer Polytechnic Institute, Troy, NY.

Shubinsky, G. (1994). Visual and Infrared Imaging for Bridge Inspection. Basic Industrial Research Laboratory (BIRL), Northwestern University, Evanston, IL.

Stratfull, R. F. (1973). Corrosion Autopsy of a Structurally Unsound Bridge Deck. In Highway Research Record 433, HRB, National Research Council, Washington, DC, pp. 1-11.

Stratfull, R. F. (1973). Half-Cell Potentials and the Corrosion of Steel in Concrete. In Highway Research Record 433, HRB, National Research Council, Washington, DC, pp. 12-21.

Stratfull, R. F., W. J. Jurkovich, and D. L. Spellman. (1975). Corrosion Testing of Bridge Decks. In Transportation Research Record 539, TRB, National Research Council, Washington, DC, pp. 50-59.

Thevendran, V., Chen, S., Shanmugam, N. E., and Richard Liew, J. Y. (1999). "Nonlinear analysis of steel-concrete composite beams curved in plan." Finite elements in analysis and design, 32(3), 125-139.

Tuutti, K. (1982). "Corrosion of steel in concrete."

Ulaby, F. (2010). Fundamentals of Applied Electromagnetics. Upper Saddle River, New Jersey, Prentice Hall.

Van der Wielen, A., Courard, L., and Nguyen, F. (2000). "Nondestructive detection of delaminations in concrete bridge decks." IEEE, 1-5.

Weiss, N. A. (2005). Introductory statistics, Pearson Addison Wesley, Boston.

William, G. W., Shoukry, S. N., and Riad, M. Y. (2008). Development of early age shrinkage stresses in reinforced concrete bridge decks. Mechanics of Time-Dependent Materials, 12(4), 343-356.

Yehia, S., Abudayyeh, O., Abdel-Qader, I., and Zalt, A. (2008). "Ground-penetrating radar, chain drag, and ground truth: Correlation of bridge deck assessment data." Transportation Research Record(2044), 39-50.

Yehia, S., Abudayyeh, O., Nabulsi, S., and Abdelqader, I. (2007). "Detection of common defects in concrete bridge decks using nondestructive evaluation techniques." Journal of Bridge Engineering, 12(2), 215-225.

Zhou, K., Martin-Perez, B., and Lounis, Z. (2000). "Finite element analysis of corrosion-induced cracking, spalling and delamination of RC bridge decks." 187-196.

Zou, T. (2012). "Comparison of Bridge Deck Damage Condition Evaluated by GPR and Chain Drag." VTechWorks. <http://vtechworks.lib.vt.edu/handle/10919/18741>.

Appendix A:

GPR signal attenuation is determined by the attenuation coefficient and traveled distance of EM wave, as shown in Eq. (A-1). The negative sign represents the loss of energy in signal propagation.

$$A = -\alpha \cdot d \tag{A-1}$$

where

A = magnitude of EM signal attenuation in dB

α = the attenuation coefficient in dB/m

d = signal traveling path distance in meter

The attenuation coefficient is used to determine the attenuation factor, which is further used to calculate the magnitude of signal attenuation when EM signal is transmitted into the medium and received by the antenna. Attenuation coefficient is related to electrical and magnetic properties of the medium, and is represented by Eq. (A-2).

$$\alpha = 8.686 \times \omega \times \left[\frac{\varepsilon' \mu_0}{2} \left[\sqrt{1 + \left(\frac{\sigma}{\omega \varepsilon_r \varepsilon_0} \right)^2} - 1 \right] \right]^{1/2} \tag{A-2}$$

where

ω = angular frequency ($2\pi \cdot f$) in rads/s

f = electromagnetic frequency in Hz

$\varepsilon' = \varepsilon_r \cdot \varepsilon_0$= dielectric permittivity of concrete mixture in Farad/m

μ_0 = magnetic permeability of free space = 4π x 10^{-7}Henry/m

ε_r = relative permittivity of concrete mixture (dimensionless)

ε_0 = dielectric permittivity of free space = 8.854 x 10^{-12} Farad/m

σ = concrete conductivity in S/m.

From Eq. (A-2), it is obvious that attenuation coefficient is determined by relative dielectric permittivity, magnetic permeability and electrical conductivity of concrete mixture. Since the value of magnetic permeability for most nonferromagnetic materials, e.g., concrete, is small, the magnetic permeability of free surface could be used (Ulaby et al. 2010). The determination of relative dielectric permittivity and electrical conductivity of concrete mixture is introduced in the following sections.

Relative Permittivity Determination

Permittivity describes the ability of a material to polarize, support polarization, and store energy in response to an external electrical field (Olhoeft 1998). Permittivity is represented as a complex number that has both a storage component, or real part, and a dissipation component, or imaginary part (Baker et al. 2007). The real part of permittivity is measure of a material's polarization and energy storage, and described as:

$$\varepsilon^{'} = \varepsilon_r \cdot \varepsilon_0 \tag{A-3}$$

The imaginary part is a measure of a material's dissipation or loss energy, and is related to the electrical conductivity of the material by:

$$\varepsilon^{''} = \frac{\sigma}{\omega} \tag{A-4}$$

Relative permittivity is a critical factor in GPR study that controls the signal propagation velocity and attenuation, and could be related to permittivity of the material and free space by Eq. (A-5) as:

$$\varepsilon_r = \frac{\varepsilon^{'}}{\varepsilon_0} - i \cdot \frac{\varepsilon^{''}}{\varepsilon_0} \tag{A-5}$$

Relative Permittivity of Saline Water

The relative permittivity of concrete mixture is greatly influenced by the moisture and chloride content. Application of de-icing salts on concrete bridge decks causes the salt to penetrate through surface cracking, and the salt is commonly referred to as the free chloride which goes directly into solution. The presence of free chlorides reduces the real part of complex relative permittivity of water, and increase the imaginary part, which greatly affect the attenuation of radar signals. The complex relative permittivity of saline water is determined by the well-known Debye equation (Ulaby et al. 1986):

$$\varepsilon_{sw} = \varepsilon'_{sw} + i \cdot \varepsilon''_{sw} \tag{A-6}$$

With the real and imaginary parts given by:

$$\varepsilon'_{sw} = \varepsilon_{sw\infty} + \frac{\varepsilon_{sw0} - \varepsilon_{sw\infty}}{1 + (2\pi \cdot f \cdot \tau_{sw})^2} \tag{A-7}$$

and

$$\varepsilon''_{sw} = \frac{2\pi \cdot f \cdot \tau_{sw} \cdot (\varepsilon_{sw0} - \varepsilon_{sw\infty})}{1 + (2\pi \cdot f \cdot \tau_{sw})^2} + \frac{\sigma_i}{2\pi \cdot f \cdot \varepsilon_0} \tag{A-8}$$

where

ε_{sw0} = static relative permittivity of saline water (dimensionless)

$\varepsilon_{sw\infty}$ = relative permittivity of saline water at infinite frequency (dimensionless)

τ_{sw} = relaxation time of saline water (seconds)

σ_i = ionic conductivity of the aqueous saline solution (S/m)

The relative permittivity at infinite frequency is not dependent on salinity, and the experimental study has approved that $\varepsilon_{sw\infty}$ = 4.9 is a good fit for available data (Stogryn 1971). The static relative permittivity of saline water is dependent on the salinity (S_{sw}) of a salt solution and temperature (T), which is defined by the following equations:

$$N_{sw} = S_{sw} \cdot (1.707 \times 10^{-2} + 1.205 \times 10^{-5} \cdot S_{sw} + 4.058 \times 10^{-9} \cdot S_{sw}^2) \tag{A-9}$$

$$\varepsilon_{sw0}(T,0) = 88.045 - 0.415 \cdot T + 6.295 \times 10^{-4} \cdot T^2 + 1.075 \times 10^{-5} \cdot T^3 \quad \text{(A-10)}$$

$$a_1(N_{sw}) = 1.0 - 0.255 \cdot N_{sw} + 5.15 \times 10^{-2} \cdot N_{sw}^2 - 6.89 \times 10^{-3} \cdot N_{sw}^3 \quad \text{(A-11)}$$

$$\varepsilon_{sw0}(T, N_{sw}) = \varepsilon_{sw0}(T,0) \cdot a_1(N_{sw}) \quad \text{(A-12)}$$

where the normality of saline water (N_{sw}) is related to the salinity (S_{sw}) by Eq. (A-10) by Klein (Klein and Swift 1977). The salinity (S_{sw}) of a salt solution is defined as the total mass of solid salt in grams dissolved in one kilogram of the aqueous solution, and is expressed in parts per thousand (*ppt*) by weight. The salinity of pore water in concrete bridge decks is typically not directly measured, but determined indirectly by free chloride and moisture content. To convert the percentage chloride content to NaCl (sodium chloride) equivalent, a multiplication factor, which is 1.65, equal to the ratio of molecular weight of NaCl (58.5) to the atomic weight of chloride (35.5) is applied (Halabe et al. 1989). The salinity of pore water is then determined by dividing the NaCl equivalent of the free chloride content by the corresponding moisture content.

The relaxation time of saline water is related to the normality of saline water (N_{sw}) and temperature (T) by the following equations (A-13 – A-15):

$$\tau_{sw}(T, N_{sw}) = \tau_{sw}(T,0) \cdot b_1(T, N_{sw}) \quad \text{(A-13)}$$

$$2\pi \cdot \tau_{sw}(T,0) = 1.111 \times 10^{-10} - 3.824 \times 10^{-12} \cdot T + 6.938 \times 10^{-14} \cdot T^2 - 5.096 \times 10^{-16} \cdot T^3 \quad \text{(A-14)}$$

$$b_1(T, N_{sw}) = 1.0 + 0.146 \times 10^{-2} \cdot T \cdot N_{sw} - 4.896 \times 10^{-2} \cdot N_{sw} - 2.97 \times 10^{-2} \cdot N_{sw}^2 + 5.64 \times 10^{-3} \cdot N_{sw}^3 \quad \text{(A-15)}$$

And the ionic conductivity of the aqueous saline solution is expressed as:

$$\sigma_i(T, N_{sw}) = \sigma_i(25, N_{sw}) \cdot c_1(\Delta, N_{sw}) \quad \text{(A-16)}$$

$$\sigma_i(25, N_{sw}) = N_{sw}(10.39 - 2.378 \cdot N_{sw} + 0.683 \cdot N_{sw}^2 - 0.135 \cdot N_{sw}^3 + 1.01 \times 10^{-2} \cdot N_{sw}^4) \quad \text{(A-17)}$$

$$c_1(\Delta, N_{sw}) = 1.0 - 1.96 \times 10^{-2} \cdot \Delta + 8.08 \times 10^{-5} \cdot \Delta^2 - N_{sw} \cdot \Delta[3.02 \times 10^{-5} + 3.92 \times 10^{-5} \cdot \Delta + N_{sw}(1.72 \times 10^{-5} - 6.58 \times 10^{-6} \cdot \Delta)] \quad \text{(A-18)}$$

$$\Delta = 25 - T \tag{A-19}$$

By substituting the static relative permittivity of saline water (ε_{sw0}), relaxation time of saline water (τ_{sw}) and the ionic conductivity of the aqueous saline solution (σ_i) into Eq. (A-7) and (A-8), the real and imaginary parts of relative permittivity of saline water could be determined.

Relative Permittivity of Concrete Mixture

This section discusses the model to predict the relative permittivity of concrete mixture based on the properties and volumetric proportions of the constituents. Coarse aggregate, fine aggregate, cement paste, air, water and salt are the most significant constituents of concrete mixture. The porosity (ϕ) of coarse concrete and saturation (S) of pore water are important factors in determining the relative permittivity of concrete. Porosity (ϕ) is defined as the volume of voids divided by the total volume of concrete. The normal porosity of newly cast concrete is in the order of 0.1 (Popovics 1985), but the porosity in actual bridges could be about 0.15, or even up to 0.2 due to the freeze-thaw cycles. Degree of saturation is defined as the volume of water divided by the volume of voids. The degree of saturation (S) of the top and bottom one inch layer of concrete in conventional concrete bridge decks and the top one inch of stay-in-place concrete decks vary between 40% or 50% in warm summer months to 75% in cold winter months (Carrier et al. 1975). Porosity and degree of saturation could be measured in site on bridge decks, therefore providing relatively accurate predictions on the relative permittivity of concrete.

According to the Complex Refractive Index Method (CRIM), the complex relative permittivity of concrete mixture is calculated by the following equation:

$$\sqrt{\varepsilon_r} = (1-\phi)\cdot\sqrt{\varepsilon_m} + (1-S)\cdot\phi\cdot\sqrt{\varepsilon_a} + \phi\cdot S\cdot\sqrt{\varepsilon_{sw}} \tag{A-20}$$

where,

ϕ =porosity of concrete = (volume of voids)/(total volume of concrete)

S =degree of saturation = (volume of water)/(volume of voids)

ε_m =relative dielectric permittivity of concrete solids = 5.0

ε_a =relative dielectric permittivity of air = 1.0

ε_{sw} =relative complex dielectric permittivity of water

ε_r =relative dielectric permittivity of resulting concrete mixture (a complex quantity)

The complex refractive index method asserts that the effective complex-refractive index for the mixture is given by the volume average of the complex refractive indices of the constituents (Feng and Sen 1985). This method has been widely used for soils, rocks and concrete due to its simplicity, but has no theoretical basis. However, results by this CRIM method were compared with other more sophisticated models (Halabe et al. 1989), and the difference is within acceptable range for common concrete in bridge decks. Therefore, for the consideration of simplicity and engineering applications, the CRIM model will be used in this paper to estimate relative permittivity of concrete mixture.

Electrical Conductivity Determination

Electrical conductivity is a measure of the ease of electron movement within a material that is under the influence of an external electrical field (Saarenketo 1998). Electrical current can propagate through rock and minerals through three methods, which are ohmic, electrolytic or dielectric (Ulaby 2010). Electrolytic conduction requires the presence of irons to carry the charge, such as those found dissolved in groundwater, therefore electrolytic conduction is the dominant process in moist or wet material. According to Archie's law, electrolytic conduction is dependent on porosity and conductivity of the pore fluid:

$$\sigma = a \cdot \phi^m \cdot S^n \cdot \sigma_i + \sigma_c \qquad \text{(A-21)}$$

where

a = constant (0.4-2)

m = constant (1.3-2.5)

n = constant (~2)

σ_i = pore fluid conductivity (S/m)

σ_c = surface conductivity of concrete (S/m)

The pore fluid conductivity σ_i is defined by Eqs. (A-16) through (A-19), and the surface conductivity of concrete could be measured on concrete bridge decks directly. Therefore, the concrete conductivity could be plugged into Eq. (A-2) to calculate attenuation coefficient.

Appendix B:

Table B-1Deflection comparison between FE model and field testing for Scenario A

Loading Scenario A							
Span	Girder	1	2	3	4	5	6
		Downward Deflection (in.)					
	Test	0.32	0.25	0.15	0.1	0.04	0.01
	FEA	0.34	0.27	0.19	0.12	0.04	0.07
North	Diff.	6%	6%	27%	25%	0%	N.A
		Uplift Deflection (in.)					
	Test	-0.13	-0.11	-0.17	-0.05	-0.03	-0.01
	FEA	-0.09	-0.08	-0.08	-0.07	-0.06	-0.07
	Diff.	-33%	-24%	-55%	31%	114%	N.A
		Downward Deflection (in.)					
	Test	0.33	0.26	0.18	0.11	0.04	0
	FEA	0.34	0.26	0.18	0.12	0.04	0.07
South	Diff.	2%	2%	1%	14%	-8%	N.A
		Uplift Deflection (in.)					
	Test	-0.14	-0.12	-0.09	-0.07	-0.04	0
	FEA	-0.08	-0.08	-0.08	-0.07	-0.06	-0.07
	Diff.	-40%	-30%	-20%	3%	77%	NA

Table B-2 Strain comparison between FE model and field testing for Scenario A

Loading Scenario A							
Span	Girder	1	2	3	4	5	6
		Tension Strains με ($x10^{-6}$)					
North	Test	84.4	60.2	28.6	14.2	1.9	0
	FEA	81.0	59.2	32.7	18.1	7.8	0
	Diff.	4%	2%	-14%	-28%	-308%	0
		Tension Strains με ($x10^{-6}$)					
South	Test	72.7	61.3	29.9	15.2	3.3	0
	FEA	79.8	59.0	32.6	18.6	8.8	0
	Diff.	-10%	4%	-9%	-22%	-166%	0

Table B-3 Deflection comparison between FE model and field testing for Scenario B

Loading Scenario B							
Span	Girder	1	2	3	4	5	6
		Downward Deflection (in.)					
	Test	0.43	0.40	0.27	0.29	0.14	0.08
	FEA	0.52	0.47	0.39	0.29	0.13	0.20
North	Diff.	21%	19%	43%	2%	-6%	155%
		Uplift Deflection (in.)					
	Test	-0.17	-0.18	-0.14	-0.11	-0.08	-0.06
	FEA	-0.16	-0.16	-0.15	-0.14	-0.13	-0.14
	Diff.	-6%	-15%	9%	26%	71%	134%
		Downward Deflection (in.)					
	Test	0.43	0.38	0.39	0.27	0.13	0.07
	FEA	0.51	0.46	0.39	0.30	0.14	0.21
South	Diff.	18%	20%	-1%	11%	4%	200%
		Uplift Deflection (in.)					
	Test	-0.20	-0.19	-0.17	-0.13	-0.08	-0.06
	FEA	-0.16	-0.16	-0.15	-0.14	-0.13	-0.14
	Diff.	-19%	-16%	-10%	12%	61%	130%

Table B-4 Strain comparison between FE model and field testing for Scenario B

Loading Scenario B							
Span	Girder	1	2	3	4	5	6
		Tension Strains με ($x10^{-6}$)					
North	Test	110.0	105.9	84.5	46.6	22.1	11.8
	FEA	106.2	103.2	79.5	50.0	29.2	14.7
	Diff.	3.45%	2.55%	5.91%	-7.34%	-32.17%	-24.24%
		Tension Strains με ($x10^{-6}$)					
South	Test	91.4	105.3	85.0	50.1	24.1	8.8
	FEA	106.2	106.3	83.3	54.3	32.6	19.0
	Diff.	-16%	-1%	2%	-8%	-35%	-115%

Table B-5 Deflection comparison between FE model and field testing for Scenario C

Loading Scenario C							
Span	Girder	1	2	3	4	5	6
		Downward Deflection (in.)					
North	Test	0.28	0.34	0.27	0.37	0.19	0.16
	FEA	0.35	0.37	0.37	0.33	0.21	0.27
	Diff.	26%	10%	41%	-10%	14%	66%
		Uplift Deflection (in.)					
	Test	-0.16	-0.16	-0.14	-0.14	-0.11	-0.11
	FEA	-0.14	-0.14	-0.13	-0.13	-0.13	-0.13
	Diff.	-10%	-14%	-2%	-2%	16%	24%
		Downward Deflection (in.)					
South	Test	0.28	0.33	0.40	N.A	0.21	0.17
	FEA	0.34	0.37	0.37	0.34	0.22	0.28
	Diff.	21%	12%	-7%	N.A	5%	63%
		Uplift Deflection (in.)					
	Test	-0.16	-0.16	-0.16	-0.14	-0.11	-0.11
	FEA	-0.14	-0.14	-0.14	-0.13	-0.13	-0.13
	Diff.	-12%	-14%	-14%	-4%	20%	16%

Table B-6 Strain comparison between FE model and field testing for Scenario C

Loading Scenario C							
Span	Girder	1	2	3	4	5	6
		Tension Strains με ($x10^{-6}$)					
North	Test	57.80	81.50	95.30	76.20	43.70	30.00
	FEA	61.85	79.27	83.74	71.81	49.05	31.75
	Diff.	-7%	3%	12%	6%	-12%	-6%
		Tension Strains με ($x10^{-6}$)					
South	Test	48.40	75.90	90.80	81.60	46.80	28.20
	FEA	57.19	77.47	85.17	72.33	51.63	35.39
	Diff.	-18%	-2%	6%	11%	-10%	-26%

Table B-7 Deflection comparison between FE model and field testing for Scenario D

Loading Scenario D							
Span	Girder	1	2	3	4	5	6
		Downward Deflection (in.)					
	Test	0.14	0.19	0.18	0.19	0.11	0.08
	FEA	0.18	0.19	0.19	0.17	0.10	0.13
North	Diff.	30%	4%	8%	-13%	-9%	71%
		Uplift Deflection (in.)					
	Test	-0.08	-0.08	-0.07	-0.07	-0.06	-0.05
	FEA	-0.07	-0.07	-0.07	-0.07	-0.06	-0.07
	Diff.	-12%	-17%	-4%	-3%	15%	23%
		Downward Deflection (in.)					
	Test	0.15	0.19	0.23	0.20	0.11	0.08
	FEA	0.18	0.19	0.20	0.17	0.10	0.13
South	Diff.	16%	-1%	-16%	-16%	-12%	55%
		Uplift Deflection (in.)					
	Test	-0.09	-0.09	-0.09	-0.08	-0.06	-0.06
	FEA	-0.07	-0.07	-0.07	-0.07	-0.07	-0.07
	Diff.	-22%	-22%	-22%	-13%	16%	14%

Table B-8 Strain comparison between FE model and field testing for Scenario D

Loading Scenario D							
Span	Girder	1	2	3	4	5	6
		Tension Strains με ($x10^{-6}$)					
North	Test	29.1	41.8	56.1	38.9	20.9	13.0
	FEA	30.6	40.2	46.2	31.2	20.5	13.2
	Diff.	-5%	4%	18%	20%	2%	-2%
		Tension Strains με ($x10^{-6}$)					
South	Test	25.2	38.8	54.9	40.2	21.8	14.6
	FEA	29.3	41.0	47.4	34.7	22.7	15.2
	Diff.	-16%	-6%	14%	14%	-4%	-4%

Table B-9 Deflection comparison between FE model and field testing for Scenario E

Loading Scenario E							
Span	Girder	1	2	3	4	5	6
		Downward Deflection (in.)					
	Test	0.05	0.09	0.13	0.23	0.18	0.22
	FEA	0.07	0.11	0.15	0.19	0.22	0.22
North	Diff.	61%	17%	13%	-18%	23%	0%
		Uplift Deflection (in.)					
	Test	-0.07	-0.06	-0.07	-0.09	-0.09	-0.11
	FEA	-0.06	-0.06	-0.07	-0.07	-0.07	-0.07
	Diff.	-6%	12%	0%	-21%	-20%	-35%
		Downward Deflection (in.)					
	Test	0.05	0.09	0.16	0.23	0.21	0.24
	FEA	0.07	0.11	0.15	0.20	0.22	0.22
South	Diff.	50%	16%	-4%	-14%	7%	-8%
		Uplift Deflection (in.)					
	Test	-0.06	-0.07	-0.08	-0.09	-0.09	-0.12
	FEA	-0.06	-0.06	-0.07	-0.07	-0.07	-0.07
	Diff.	5%	-3%	-14%	-24%	-19%	-40%

Table B-10 Strain comparison between FE model and field testing for Scenario E

Loading Scenario E							
Span	Girder	1	2	3	4	5	6
		Tension Strains με ($x10^{-6}$)					
North	Test	9.4	16.5	28.0	50.2	55.3	42.3
	FEA	10.8	17.6	28.5	44.3	50.7	40.2
	Diff.	-14%	-7%	-2%	12%	8%	5%
		Tension Strains με ($x10^{-6}$)					
South	Test	8.0	14.2	26.3	50.7	56.0	42.8
	FEA	8.5	16.7	28.0	43.9	51.0	42.0
	Diff.	-7%	-18%	-6%	13%	9%	2%